A Linear Scaling DFT-Method and High-Throughput Calculations for p-Type Transparent Semiconductors

Von der Fakultät für Naturwissenschaften
der Universität Paderborn
genehmigte

Dissertation

zur Erlangung des akademischen Grades
Doktor der Naturwissenschaften

— Dr. rer. nat. —

von
Hendrik Wiebeler
aus Delbrück

Paderborn, im Januar 2020

Eingereicht am: 15.01.2020
Mündliche Prüfung am: 09.04.2020

Promotionskommission

Vorsitzende: Prof. Dr. Claudia Schmidt
Erstgutachter: Prof. Dr. Thomas D. Kühne
Zweitgutachter: Prof. Dr. Matthias Bauer
Drittgutachter: Dr. Hossein Mirhosseini
Beisitzer: PD Dr. Hans Egold

Archiv
Elektronische Dissertationen und Habilitationen der Universität Paderborn:
`https://www.ub.uni-paderborn.de/`

Contents

1 Abstract/ Zusammenfassung

1.1 Abstract

This dissertation consists of two parts. The first part deals with the linear-scaling code developed in our group. Scaling with system size is still a bottleneck in electronic structure calculations, especially when they are combined with molecular dynamics, for which typically thousands of force evaluations have to be performed. As discussed in this thesis, the inaccurate calculation of forces in a linear-scaling density functional theory (DFT) code can be compensated by employing Langevin dynamics. To achieve this, the forces need to exhibit a white noised error. Based on previous work, we investigate the nature of this error in our linear-scaling code by employing autocorrelation functions and discuss a possible implementation into an *ab initio* molecular dynamics (AIMD) scheme.

In the second part of this thesis, the results of our computational screening for transparent p-type semiconductors are presented. Transparent conducting materials (TCMs) have received attention owing to their wide range of applications like solar cells and transparent electronics. However, transparent conducting oxides (TCOs) have been predominantly commercialized as n-type TCMs. In contrast to this, the performance of p-type TCOs is not satisfactory. Hence, the computational screening of pnictide- and halide-based binary and ternary compounds is discussed in this thesis to identify promising p-type TCMs. Our investigations start from *ab initio* results that can be retrieved from free-access databases for such materials. We employ criteria for the band gap, stability, and hole effective mass in our material screening procedure. Furthermore, we describe the realized implementation of the methods required for our *in silico* screening. We also assess the validity of the employed methods and our criteria. In the end, we propose 4 binary pnictides, 7 ternary pnictides and 1 binary halide that turn out to be the most promising materials for application as p-type TCMs.

The investigations in the second part deal with static properties of inorganic compounds. To go one step further, also molecular dynamics might be employed to investigate processes like sputtering and charge transport. Such simulations would profit from the flexibility and accuracy of AIMD, but require an efficient implementation of this method. This might be achieved with electronic structure calculations that are discussed in the first part of this thesis and scale linearly with system size. Furthermore, such methods might also be the method of choice for the simulation of supercells consisting of hundreds of atoms. Overall, the combination of electronic structure methods that scale linearly with system size and of material screening holds the promise of pushing the boundaries of the current knowledge by going beyond the static picture and by more efficient simulations of materials of increasing complexity.

1.2 Zusammenfassung

Diese Dissertation besteht aus zwei Teilen. Der erste Teil ist dem in unserer Gruppe entwickeltem linear skalierendem Code gewidmet. Die Skalierung der Rechenzeit mit Systemgröße ist immer noch ein Problem bei elektronischen Strukturberechnungen, insbesondere wenn diese Rechnungen in Molekulardynamik-Simulationen mit tausenden von Kraftberechnungen benutzt werden. In der Dissertation wird diskutiert, dass eine ungenaue Berechnung der Kräfte in einem Dichtfunktionaltheorie-Code durch Lösen einer Langevin-Gleichung für die Molekulardynamik kompensiert werden kann. Um dies zu ermöglichen, müssen die Kräfte weißes Rauschen im Fehler aufweisen. Basierend auf vorangegangene Arbeiten untersuchen wir in dieser Dissertation mittels Autokorrelationsfunktionen diesen Fehler, der sich bei Verwendung unseres linear skalierenden Codes bei der Kraftberechnung ergibt. Zusätzlich wird eine mögliche Implementierung in ein *ab initio* Molekulardynamik (AIMD)-Verfahren erläutert.

Im zweiten Teil dieser Dissertation werden die Resultate einer rechnergestützten Suche nach einem transparenten lochleitenden Halbleiter präsentiert. Wegen ihrer weitreichenden Anwendbarkeit, z.B. in Solarzellen und transparenter Elektronik, haben transparente elektrisch leitende Materialien (TCMs) viel Aufmerksamkeit erhalten. Momentan wird die kommerzielle Anwendung von transparenten elektrisch leitfähigen Oxiden (TCOs) dominiert. Im Gegensatz zur Elektronenleitfähigkeit ist die Lochleitfähigkeit bei diesen Oxiden jedoch unbefriedigend. Wir stellen daher in dieser Dissertation die rechnergestützte Suche nach vielversprechenden lochleitenden TCMs vor und untersuchen stickstoff-, phosphor- sowie halogenhaltige binäre und ternäre Verbindungen. Unsere Suche startet dabei von *ab initio* Daten, die in frei zugänglichen Datenbanken verfügbar sind. Wir benutzen Kriterien für Stabilität, Bandlücke und effektive Masse der Löcher, um die Kandidaten zu reduzieren. Die Implementierung der für die Suche benötigten Methoden wird in dieser Dissertation beschrieben. Zusätzlich wird die Validität der benutzten Methoden und Kriterien diskutiert. Letztendlich schlagen wir 4 binäre stickstoff- und phosphorhaltige Verbindungen, 7 ternäre stickstoff- und phosphorhaltige Verbindungen sowie eine binäre halogenhaltige Verbindung vor, die sich als vielversprechende Materialien für lochleitende TCM-Anwendungen erwiesen haben.

Die Suche im zweiten Teil basiert auf Berechnungen von statischen Eigenschaften anorganischer Materialien. Um einen Schritt weiterzugehen, könnte Molekulardynamik für die Simulation von Prozessen wie Sputtern und Ladungstransport eingesetzt werden. Diese Berechnungen könnten von der Flexibilität und Genauigkeit von AIMD-Simulationen profitieren, allerdings bräuchten sie eine effiziente Implementierung. Dies könnte mit der im ersten Teil dieser Dissertation diskutierten linear skalierenden Methode erreicht werden. Des Weiteren könnte dies auch die Methode der Wahl sein, um Superzellen zu simulieren, die aus hunderten von Atomen bestehen. Letztendlich verspricht die Kombination einer linear skalierenden Methodik zur elektronischen Strukturberechnung mit der rechnergestützten Suche die bisherigen Grenzen des aktuellen Wissensstandes zu erweitern, indem dynamischen Eigenschaften direkt simuliert und die Berechnungen von immer komplexeren Materialien möglich werden.

2 Linear scaling

The work on linear scaling was a continuation of my master's thesis. The text is based on a draft for an upcoming article. It starts with the introduction to motivate the development of methods that scale linearly with respect to system size. This is followed by a benchmark of our linear scaling method and we will discuss the noisiness of the forces. Finally, we propose an approach to perform molecular dynamics based on these forces. The results related with the autocorrelation function have been obtained during the beginning of my PhD studies, whereas the benchmark is based on results, which were already obtained during my master's thesis. However, they provide useful background information and owing to this, I have decided to also leave this part in the text.

2.1 Introduction

Quantum chemical *ab initio* methods based on Hartree-Fock (HF) and/or Density Functional Theory (DFT) are widely used tools for the determination of chemical and physical properties based on static calculations.[1,2] However, they can not describe the full picture, as these techniques have to be combined with further methods, in order to simulate time-dependent phenomena like chemical reactions and diffusion processes. For example the real-time dynamics of the nuclei can be simulated classically by solving Newton's equations of motion, whereas the forces acting on the nuclei are still calculated "on the fly" via an *ab initio* method that treats the electrons quantum mechanically. Therefore, this combination is called *ab initio* molecular dynamics (AIMD).[3–6] In principle, this method is a powerful tool, because *ab initio* calculations are employed in every time step allowing to model systems without explicitly knowing the interactions as opposed to classical MD where interactions are based on empirical knowledge. Due to the high predictive power, this approach is used in many disciplines, *e.g.* solid state physics, physical chemistry, materials science, and biophysics.[7]

However, there is a price that has to be paid for these advantages of AIMD: a compromise between, on the one hand, computational cost and on the other hand, system size and sampling has to be found. Therefore, the simulations are often based on efficient and not highly accurate quantum chemical methods using effective single-particle theories. So semi-empirical tight-binding, HF and DFT are the most commonly employed models within AIMD.[3,5] All these methods have the same computational bottleneck: the diagonalization of a very large Hamiltonian matrix. This is needed to approximately solve the Schrödinger equation and therefore to compute the total energy and especially the nuclear forces. It scales as $\mathcal{O}(N^3)$, where N denotes the number of atoms. So it is desirable to develop methods that avoid this step and scale linearly as $\mathcal{O}(N)$ in the best case.[8] Such schemes would enable simulations of systems with sizes that were previously

thought out of reach. Several linear-scaling techniques have been proposed already.[9–16] However, the problem with these schemes is that they are often only faster than conventional approaches after a system size of several hundreds of atoms is passed and they are especially problematic for metallic systems and/or if high accuracy is needed.[17] In addition, combining linear scaling approaches and AIMD leads to a unique opportunity, since errors in the forces due to linear scaling DFT approaches can be corrected by using an appropriate molecular dynamics technique. But even despite recent efforts,[18–24] neither a final answer nor method is in sight.

2.2 Grand canonical decomposition method

Starting with an effective single-particle theory, the total energy is given as :[25]

$$E = 2 \sum_{i=1}^{N_e/2} \epsilon_i + V_{dc}, \tag{2.1}$$

with N_e denoting the number of electrons. The first term is the sum of the lowest $N_e/2$ eigenvalues ϵ_i of the Hamiltonian $\mathbf{H}$, whose orbitals are doubly occupied. The second term V_{dc} is then needed to correct for the double counting and to account for the nuclear Coulomb repulsion. The computational effort of this part already scales linearly with system size, so the critical term is the first one, for which all occupied orbitals have to be determined. Typically, this requires the diagonalization of $\mathbf{H}$, which scales as $O(N_e^3)$ with system size. To avoid this, the first term in Eq. 2.1 can be rewritten employing the trace of a matrix product:

$$E = Tr[\boldsymbol{P}\mathbf{H}] + V_{dc}, \tag{2.2}$$

and $\boldsymbol{P}$ is the one-particle density matrix, which can be directly calculated instead of all the ϵ_i's. An approach to achieve this was shown by Alavi *et. al.*[26,27] and starts with the (Helmholtz) free energy functional:

$$\mathcal{F} = \Omega + \mu N_e + V_{dc}, \tag{2.3}$$

where μ denotes the chemical potential and Ω is the Grand Canonical Potential (GCP) for non-interacting fermions:

$$\begin{aligned} \Omega &= -\frac{2}{\beta} \ln \det \left(\mathbf{1} + e^{\beta(\mu\mathbf{S}-\mathbf{H})} \right) \\ &= -\frac{2}{\beta} \mathrm{Tr} \ln \left(\mathbf{1} + e^{\beta(\mu\mathbf{S}-\mathbf{H})} \right). \end{aligned} \tag{2.4}$$

The finite electronic temperature is given by $\beta^{-1} = k_B T_e$. $\mathbf{S}$ is the overlap matrix and reduces to the identity matrix $\mathbf{I}$, if an orthonormal basis set is used for the expansion of the orbitals. In the low temperature limit, *i.e.* $lim_{\beta\to\infty}$, this expression simplifies to:

$$\lim_{\beta\to\infty}\Omega = 2\sum_{i=1}^{N_e/2}\epsilon_i - \mu N_e. \tag{2.5}$$

So in this limit $\mathcal{F} = E$ holds and the first term of Eq. 2.1 is recovered. The operator of Eq. 2.4 can be factorized into P terms, as shown by Krajewski and Parrinello.[28] Without loss of generality P can be assumed to be even and consequently

$$\begin{aligned}\mathbf{I} + e^{\beta(\mu\mathbf{S}-\mathbf{H})} &= \prod_{l=1}^{P}\left(\mathbf{1} - e^{\frac{i\pi}{2P}(2l-1)}e^{\frac{\beta}{2P}(\mu\mathbf{S}-\mathbf{H})}\right)\\ &= \prod_{l=1}^{P}\mathbf{M}_l = \prod_{l=1}^{P/2}\mathbf{M}_l^*\mathbf{M}_l,\end{aligned} \tag{2.6}$$

is valid with the matrices $\mathbf{M}_l$ for $l = 1, ..., P$ being defined as:

$$\mathbf{M}_l := \mathbf{I} - e^{\frac{i\pi}{P}(2l-1)}e^{\frac{\beta}{P}(\mu\mathbf{S}-\mathbf{H})}, \tag{2.7}$$

where $*$ denotes complex conjugation. With these definitions, the GCP can be rewritten in the following way:[25]

$$\begin{aligned}\Omega = -\frac{2}{\beta}\ln\det\prod_{l=1}^{P}\mathbf{M}_l &= -\frac{2}{\beta}\ln\prod_{l=1}^{P/2}\det(\mathbf{M}_l^*\mathbf{M}_l)\\ &= \frac{4}{\beta}\sum_{l=1}^{P/2}\ln\big(\det(\mathbf{M}_l^*\mathbf{M}_l)\big)^{-\frac{1}{2}}.\end{aligned} \tag{2.8}$$

Following the train of thoughts in our previous publication[29] and inspired by lattice gauge field theory,[30] where a minus sign problem is avoided by sampling a positive definite distribution, the inverse square root of the determinant can be expressed as an integral over a complex field $\boldsymbol{\phi}_l$ having the same dimension M as the full Hilbert space, *i.e.*

$$\det(\mathbf{M}_l^*\mathbf{M}_l)^{-\frac{1}{2}} = \frac{1}{(2\pi)^{\frac{M}{2}}}\int d\boldsymbol{\phi}_l e^{-\frac{1}{2}\boldsymbol{\phi}_l^*\mathbf{M}_l^*\mathbf{M}_l\boldsymbol{\phi}_l}, \tag{2.9}$$

with $\boldsymbol{\phi}_l$ being appropriate vectors.
Employing this equation in Eq. 2.8, the GCP can be determined via the following expression:

$$\begin{aligned}\Omega &= \frac{4}{\beta}\sum_{l=1}^{P/2}\ln\left[\frac{1}{(2\pi)^{\frac{M}{2}}}\int d\boldsymbol{\phi}_l e^{-\frac{1}{2}\boldsymbol{\phi}_l^*\mathbf{M}_l^*\mathbf{M}_l\boldsymbol{\phi}_l}\right].\\ &= \frac{4}{\beta}\sum_{l=1}^{P/2}\ln\int d\boldsymbol{\phi}_l e^{-\frac{1}{2}\boldsymbol{\phi}_l^*\mathbf{M}_l^*\mathbf{M}_l\boldsymbol{\phi}_l} + const.,\end{aligned} \tag{2.10}$$

where M is the dimension of $\mathbf{M}_l^*\mathbf{M}_l$ as already mentioned.

This equation allows to obtain all physical relevant observables by functional derivatives of the GCP with respect to a suitable external parameter.[25]

$$E = \lim_{\beta\to\infty} \mathcal{F} = 2\sum_{i=1}^{N_e/2} \epsilon_i + V_{dc} = \frac{\partial(\beta\Omega)}{\partial\beta} - \mu\frac{\partial\Omega}{\partial\mu} + V_{dc}, \tag{2.11}$$

with $-\partial\Omega/\partial\mu = N_e$. In the low temperature limit, $\boldsymbol{P}$ is identical to the Fermi matrix $\boldsymbol{\rho}$, which can be written as:

$$\boldsymbol{\rho} = \frac{\partial(\beta\Omega)}{\partial\mathbf{H}} = \frac{4}{P}\sum_{l=1}^{P/2}(\mathbf{I} - (\mathbf{M}_l^*\mathbf{M}_l)^{-1}) = \frac{2}{P}\sum_{l=1}^{P/2}\left(\mathbf{I} - \mathrm{Re}\mathbf{M}_l^{-1}\right), \tag{2.12}$$

with $\mathbf{S} = -\partial\mathbf{H}/\partial\mu$. This yields:

$$\Omega = Tr[\boldsymbol{\rho}(\mathbf{H} - \mu\mathbf{S})]. \tag{2.13}$$

Analogously, we can express all physical observables as the trace of a matrix product with ρ.

The crucial aspect of the presented idea is the decomposition of $\boldsymbol{\rho}$. At low temperature, $\boldsymbol{\rho}$ corresponds to the square of the wave function and can be decomposed into a sum of $\mathbf{M}_l^{-1}$ matrices. It should be noted, that each of the matrices has a higher effective temperature β/P resulting in much sparser matrices compared to $\boldsymbol{\rho}$. Another consequence is that the Maxwell-Boltzmann distribution becomes eventually valid for the $\mathbf{M}_l^{-1}$ matrices. These $P/2$ matrices are in general very sparse with a few exceptions. So instead of diagonalizing a single and relatively dense matrix $\mathbf{H}$, it is therefore more efficient to invert $P/2$ matrices. For this approach, only the inversion of the very few ill-conditioned matrices, for which l is close to $P/2$, is significant. The other matrices are well-conditioned and therefore can be efficiently inverted by using a Chebyshev expansion,[31,32] which has *de facto* no essential computational cost. A hybrid approach can be suggested, in which these differences in the conditions are exploited. To realize this, we have to draw a line between the ill- and well-conditioned matrices by choosing an optimal $\bar{l}$. The well-conditioned ones with $l < \bar{l}$ are inverted by a Chebyshev polynomial expansion, whereas the ill-conditioned ones with $l \geq \bar{l}$ are treated via an iterative Newton-Schultz matrix inversion. A good value for $\bar{l}$ can be estimated by minimizing an *a priori* estimate of the total number of matrix multiplications.[31,32] The number of $P/2 - \bar{l}$ matrices that have to be inverted via Newton-Schultz is in general relatively small and normally it only weakly depends on the inverse electronic temperature β. Finally, the computational cost of the Chebyshev polynomial expansion is negligible and essentially independent of P.

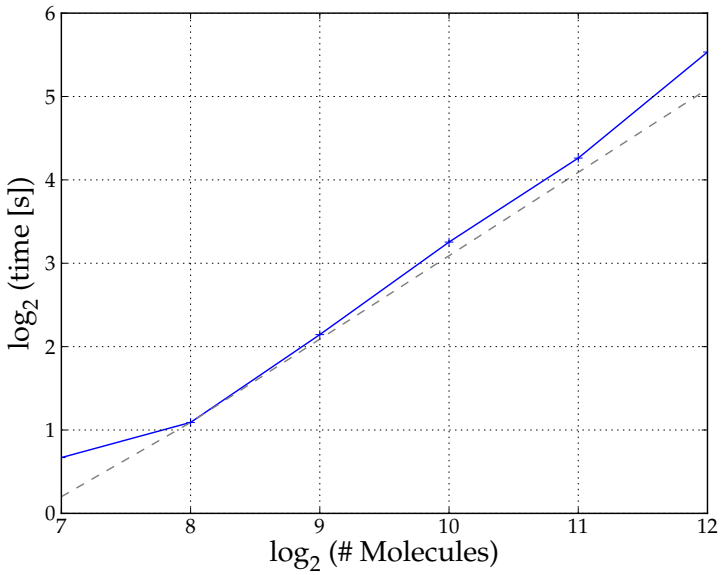

Figure 2.1: Binary logarithmic plot of the computation time for recomputing the final SCF cycle versus the number of water molecules for our linear scaling method. The dashed black line indicates ideal linear scaling.

2.3 Results and discussion

2.3.1 System-size scaling and inverse temperature

The water configurations from the CP2K[33] linear scaling benchmark set were used. Therefore, the calculations were realized with Hamiltonian matrices for systems with 128, 256, 512, 1024, 2048 and 4096 H_2O molecules. The orthogonal Hamiltonian matrices were computed by employing the BigDFT[21,24,34] code. To assess the scaling with system size for our linear scaling method, the threshold and accuracy parameters were set to 10^{-5} and μ was chosen in such a way that it yields the correct number of electrons. For the number of matrices $P/2$, which have to be inverted, a value of 350,000 was chosen. Estimates for the spectrum of the Hamiltonian and of the number of matrices $\overline{q} = P/2 - \bar{l}$ that have to be calculated via Newton-Schulz inversion were used along the lines of our previous study.[31] First we evaluated the computation time in dependence of the system size. Therefore, we set the value of β to $100\,\mathrm{Ha}^{-1}$ and the results are shown in a double binary logarithmic plot in Fig. 2.1. With the exception of the first two entries, a nearly linear scaling between the values is visible.

In addition to the size of the system, the influence of the inverse temperature β was also assessed. In this case, the Hamiltonian of the 4096 water molecule system was used and the results for different values of β are shown in Fig. 2.2. As can be estimated from the curvature of the graph, the scaling behavior is roughly quadratic. Furthermore, decreasing the inverse electronic temperature leads to less stable computations. Owing

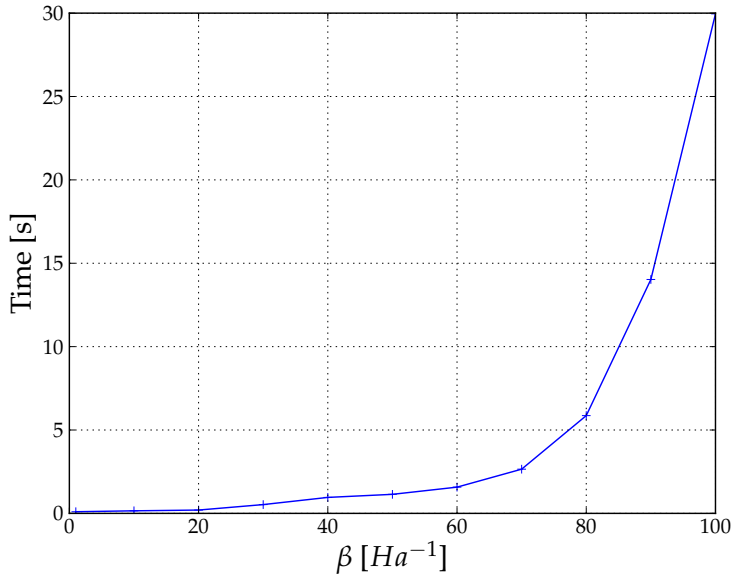

Figure 2.2: Computation time for recomputing the final SCF cycle in dependence of the inverse electronic temperature β for our linear scaling method.

to this, a value of 40 Ha^{-1} for β seems to be fine, as not much computation time can be saved anymore and the calculations are still rather stable.

2.3.2 Autocorrelation of the calculated forces

In order to estimate the quality of the resulting density matrices, the forces obtained from BigDFT and our linear scaling method were compared. For this purpose, 2000 configurations were used. They were generated using molecular dynamics and employing the four site q-TIP4P/F model[35] along with the explicit 3 body (E3B) correction.[36,37] Periodic boundary conditions were applied via the minimum image convention. Therefore, Ewald summation was employed for the long range electrostatic interactions[38] with a 9 Å cutoff to switch between long and short range electrostatics. The simulation was carried out in a cubic cell having a length of 15.536 Å and containing 125 water molecules in the NVT-ensemble with an Andersen thermostat[39] at a temperature of 300 K. In order to take nuclear quantum effects into account, ring polymer molecular dynamics with 32 beads was realized.[40] To lower the computational costs, a contraction scheme for Coulombic interactions[41,42] was applied and its cutoff was set to 5 Å. The multiple time step scheme was used to further reduce the computational costs.[43] Therefore, a total time step of 1 fs with four smaller mts-steps could be chosen. The total simulation time consisted of 50 ps of equilibration and of 2 ps of sampling. The configurations were written to disk for each step in the sampling phase, so a molecular dynamics trajectory with 2000 configurations was obtained. These configurations were used in BigDFT and after

a full SCF-cycle, the matrix of the Hamiltonian was extracted and provided as input for our linear scaling method. For the calculations with this program, μ was chosen to yield the right number of electrons. The resulting density was then transferred back to BigDFT to determine the forces.

To investigate the error introduced by our linear scaling method, we have labeled the forces calculated from BigDFT as $BOMD$ and the approximated forces from our method as App. We can therefore write:

$$\mathbf{F}_I^{\mathrm{App}} = \mathbf{F}_I^{\mathrm{BOMD}} + \boldsymbol{\Xi_I} \tag{2.14}$$

The autocorrelation function of the error in the forces for all nuclei is then given by:

$$\mathrm{ACF} = \langle \boldsymbol{\Xi_I}(0)\boldsymbol{\Xi_I}(t) \rangle \tag{2.15}$$

This quantity is a measure for the noisiness of our forces. The best result would be a δ-peak and the broader the peak the more systematic the error. For Fig. 2.3, β was kept constant and different values for accuracy and threshold were tested. As can be seen there, a huge systematic error is introduced by using thresholds higher than 10^{-5}. In contrast to this, the error caused by using a high value for accuracy is negligible. As can be seen it is sufficient to set it to 10^{-3}. This suggests setting the accuracy to a high value and the threshold to a low one.

In Fig. 2.4 we assessed the error regarding electronic temperature β and different sets of parameters. For this purpose, we used the same values for accuracy and threshold. Again it can be seen that a large systematic error is introduced as soon as a threshold greater than 10^{-5} is used. For the parameters set to 10^{-5}, we find that $\beta = 40\,\mathrm{Ha}^{-1}$ exhibits a larger systematic error. But this is already more than compensated by employing values of 10^{-6} for the parameters in combination with $\beta = 40\,\mathrm{Ha}^{-1}$. Doing the same for $\beta = 100\,\mathrm{Ha}^{-1}$ the result stays roughly the same as for 10^{-5} and $\beta = 100\,\mathrm{Ha}^{-1}$. In the limit of accurate parameters $\beta = 40\,\mathrm{Ha}^{-1}$ is giving a better result than $\beta = 100\,\mathrm{Ha}^{-1}$, therefore, lowering the value of β seems to be good for speeding up the calculation. Nevertheless, we still have to assess the error and possible further complications when our linear scaling method is used for the complete SCF-cycle. We expect still to end up with noisy forces and to deal with this issue we plan to use Langevin Dynamics, which is capable of dealing with noisy forces as outlined in the following section.

2.4 Molecular dynamics simulations with noisy forces

By approximating the BOMD forces we introduce an additional source of error. Owing to this, the net work defined as a line integral is always positive leading to a heating of the system while performing an MD simulation in the NVE ensemble. As this drift in energy is accumulating over time, even a small value can have a drastic effect on a simulation. As shown in the previous section our error exhibits a sharply peaked autocorrelation function for appropriate settings of the parameters, so it is fairly unbiased, even though it is not negligible. Since a small error is also included in BOMD forces we will look at the exact forces and therefore write:

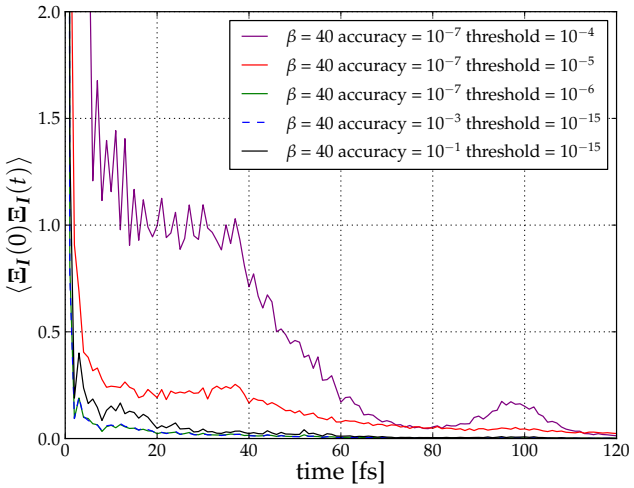

Figure 2.3: Autocorrelation functions of the error in the forces for $\beta = 40$, various threshold and accuracy parameters. Starting with values for an accurate but highly truncated calculation (magenta), we lower the threshold to 10^{-5} (red) and 10^{-6} (green). Virtually no truncation is used by employing a value of 10^{-15} (blue and black) and for these latter two graphs, the accuracy was set to 10^{-3} (blue) and 10^{-1} (black).

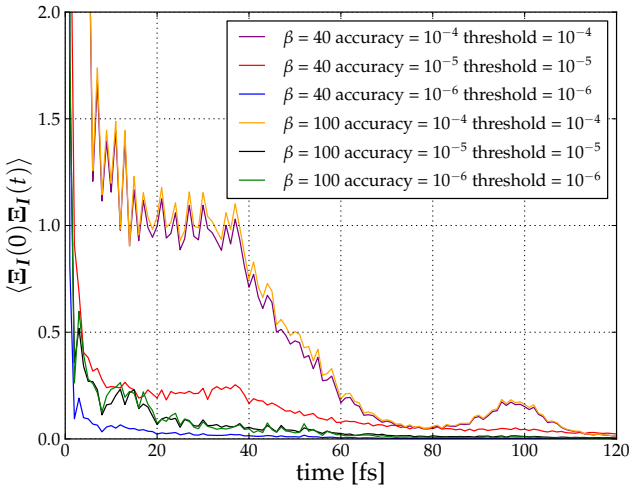

Figure 2.4: Autocorrelation functions of the error in the forces for various threshold and accuracy parameters as well as for two values of and β . We start with $\beta = 40\,\mathrm{Ha}^{-1}$ and accuracy and threshold set to 10^{-4} (magenta), 10^{-5} (red), and 10^{-6} (blue). Changing β to $100\,\mathrm{Ha}^{-1}$, we repeat the calculation with values of 10^{-4} (yellow), 10^{-5} (black), and 10^{-6} (green) for accuracy and threshold.

$$\mathbf{F}_I^{\text{exact}} = \mathbf{F}_I^{\text{App}} - \boldsymbol{\Xi_I} \tag{2.16}$$

We therefore assume that the BOMD error is negligible or simply adds to the error introduced by approximating the forces. It should be noted that the noise term is quite large compared to normal noise. This will prevent us from obtaining the correct Boltzmann averages by simply solving Newton's equations of motion, but it can be rigorously corrected by employing a modified Langevin equation based on the fact that $\boldsymbol{\Xi}_I$ is unbiased. As proposed by Krajewski and Parrinello,[28,44] we can sample the canonical distribution by solving the following equation:

$$\boldsymbol{M_I}\ddot{\boldsymbol{R}}_I = \mathbf{F}_I^{\text{App}} - \boldsymbol{\Xi}_I - \gamma_L \boldsymbol{M_I}\dot{\boldsymbol{R}}_I \tag{2.17}$$

with $\mathbf{R}_I$ being the position of nuclei I and M_I its mass. The second term contains an appropriately chosen friction coefficient γ_L for compensating the noise $\boldsymbol{\Xi}_I^L$. For this purpose, the following equation has to hold

$$\langle \mathbf{F}_I(0)\, \boldsymbol{\Xi}_I(t) \rangle \cong 0, \tag{2.18}$$

as well as the fluctuation-dissipation theorem

$$\langle \boldsymbol{\Xi}_I(0)\, \boldsymbol{\Xi}_I(t) \rangle = 2\gamma_L k_B T \boldsymbol{M_I} \delta(t). \tag{2.19}$$

If γ_L satisfies Eq. 2.19, we obtain a genuine Langevin equation, which in turn assures accurate sampling of the Boltzmann distribution. However, employing Eq. 2.19 to deduce γ_L would require the knowledge of $\boldsymbol{\Xi}_I$. In contrast to this, if the latter is approximately unbiased, it is possible to determine γ_L by empirical variation, so that the equipartition theorem $\langle \frac{1}{2}\boldsymbol{M_I}\dot{\boldsymbol{R}}_I^2 \rangle = \frac{3}{2}k_B T$ is fulfilled. Once this is accomplished, γ_L is a constant during the simulation. This allows the efficient determination of observables without knowing $\mathbf{F}_I^{\text{exact}}$, but just $\mathbf{F}_I^{App}$.

2.5 Conclusions

In this work the next steps towards AIMD with linear scaling in system size were undertaken. For this purpose, the orthogonal Hamiltonian matrix from BigDFT was extracted and processed in our linear scaling method. We presented promising benchmark results demonstrating efficient handling of the orthogonal Hamiltonian matrices by our method, which becomes evident by the assessment of the computation time. Based on these results, a potential speedup of the BigDFT program seems to be possible. In addition, we assessed various parameters for optimal performance and investigated the nature of the error in the forces on the nuclei as the difference of the forces from exact BOMD and from our scheme. We find that further noise is introduced in our simulations by truncating the intermediate matrices of the Chebyshev expansion, limited numerical precision and a finite integration time step. Since the additional noise is uncorrelated it should be possible to correct the unbiased noisy forces by employing Langevin dynamics.[5,25,28,45–47]

3 High-throughput methodology

3.1 Solar cells and the SpeedCIGS-project

3.1.1 Solar cells

Three billion years ago our planet was changed because of the emergence of cyanobacteria, which were able to do photosynthesis. This enabled life as we know it. We are in the process of reversing photosynthesis by burning the products of this process, which are coal, petrol and petroleum gas. This will lead to two problems: The first one is the limited availability of the above mentioned fuels; the other is the question of the climate change, *i.e.*, will we change our planet back to the conditions before the emergence of photosynthesis? In light of these challenges, work on renewable energies, *e.g.* solar cells, is of utmost importance.

In 2002, Germany had an energy consumption of $494 \cdot 10^6$ t coal equiv./a,[48] where one coal equivalent corresponds to $29 \cdot 10^9$ J. In cmparison to this, all plants in Germany are producing around $400 \cdot 10^6$ t coal equiv./a.[48] In order to avoid plastering every square meter with solar cells, we should be interested in developing more efficient solar cells. The average efficiency of the photosynthesis process in plants is about 1 %, so there is quite some room for improvements. To illustrate this, we can assume the process of energy conversion in solar cells to be based on a black body absorber and by employing an ideal Carnot process. We can then estimate the efficiency by multiplying the absorber efficiency with the efficiency of the Carnot process:[48]

$$\eta_{bC} = \eta_{abs}\eta_C = \left(-\frac{\Omega_{emit}}{\Omega_{abs}}\frac{T_A^4}{T_S^4}\right)\left(-\frac{T_0}{T_A}\right). \tag{3.1}$$

We have to consider three different temperatures: the temperature of the sun (T_S), the absorber temperature (T_A), as well as the temperature of the environment(T_0). Ω is the solid angle during emission and absorption. For a black body absorber, we can set the quotient to 1 leaving only a temperature-dependent expression. Furthermore, we assume the temperature of the sun to be 5800 K and 300 K for the environment temperature. Then, the efficiency as function of the absorber temperature can be plotted as shown in Ref. 48. The plot will reach a maximum efficiency of 85 % at 2478 K absorber temperature.[48] This high absorber temperature would probably melt most of the materials, which are used in solar cell. Nevertheless, compared to a silicon solar cell with 20 μm thickness[48] and an efficiency of 28 %, there should be room for improvements.

We should look more into the details and try to understand why the silicon solar cell is performing poorly when compared to an idealized Carnot process. We can calculate the overall efficiency of a solar cell by splitting the efficiency into four factors:[48]

$$\eta = \eta_{abs} \cdot \eta_{thermalization} \cdot \eta_{thermodynamic} \cdot FF. \tag{3.2}$$

η_{abs} is the efficiency of the absorption process, where we have to account for photons with energy smaller than the band gap, which can not be absorbed. The thermalization efficiency $\eta_{thermalization}$ is accounting for energy losses during separation of hole and electron. The thermodynamic efficiency $\eta_{thermodynamic}$ is accounting for the loss of energy that comes along with the conversion of free energy into usable energy. The fill factor FF is taking into account missing device specific loss mechanisms like device resistance and opposing currents. It can be determined by measuring the I-V characteristics of the solar cell. For the above mentioned silicon solar cell, this translates into:

$$\eta = 0.74 \cdot 0.67 \cdot 0.64 \cdot 0.89 = 0.28. \tag{3.3}$$

Therefore, the previously mentioned 28 % efficiency are obtained. The lowest efficiencies entering the product are $\eta_{thermalization}$ and $\eta_{thermodynamic}$. In addition, a tandem solar cell offers the potential to improve the thermalization and absorption efficiencies. The National Renewable Energy Laboratory (NREL) efficiency tables are good for illustrating the importance of such multi-junction solar cells, as the most efficient solar cells are several percent more efficient than solar cells with one absorber only.[49] The best concentrator multi-junction solar cells reach up to 46 % efficiency, which is several percent above the Shockley-Queisser limit of 33.7 %. The latter was derived for a single p-n junction.[50] The record efficiency for nonconcentrator tandem solar cells is 32.8 %, still smaller than the Shockley-Queisser limit, but already better than the 29.1 % for single junction GaAs thin film crystal solar cells.[49]

3.1.2 p-n junction

Commonly used solar cells are based on p-n junctions, which are, simply speaking, the contact region between a hole-doped semiconductor and an electron-doped semiconductor. For simplicity, we will first look at a junction consisting of electron- (n-) and hole- (p-)doped semiconductors of the same material and follow the discussion in "Festkörperphysik".[51] Doping of the material changes the chemical potential of the electrons. It shifts more towards the valence band by doping the material with holes, whereas it moves more towards the conduction band when electrons are employed for doping. When the two differently doped materials are in contact and reach the equilibrium, the difference of the chemical potential is zero everywhere. This results in smaller energies for the valence and conduction bands of the n-doped semiconductor relative to the p-doped one and the bands are curved in the region in-between, see Fig. 3.1.

If an electron and a hole are generated in this region, they would be separated since the electron travels to the side, where the conduction band is lower in energy and the hole moves to the side, where the valence band has the higher energy. This charge separation leads to a voltage, which can be used to generate electricity. This consideration also applies for charges, which are already present at the interface. Owing to this, even in equilibrium charges are separated and a space-charge region exists at the interface

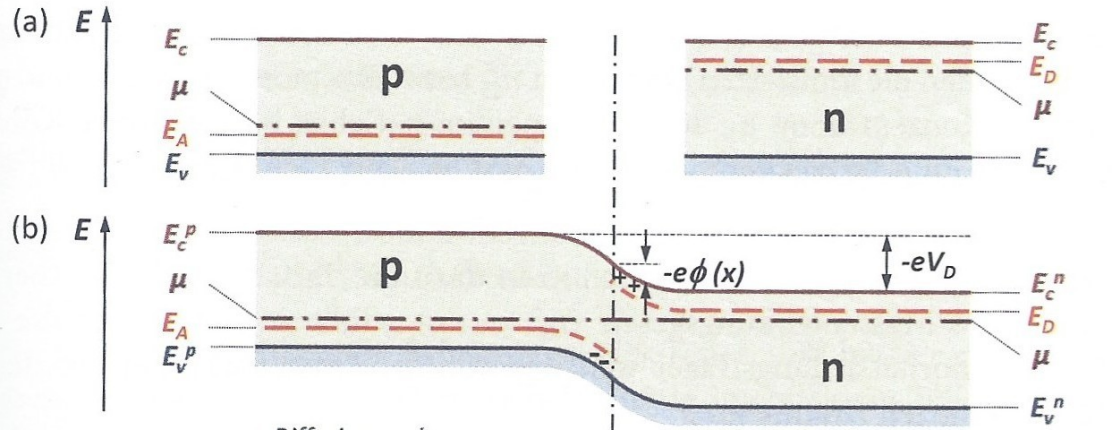

Figure 3.1: (a) For the isolated cases in the upper part, the Fermi level μ is shifted in comparison to an undoped semiconductor: downwards for p-type doping because of acceptor defects with an activation energy E_A and upwards for n-type doping because of donor defects with an activation energy E_D. (b) Combining these two semiconductors results in the alignment of the Fermi energies and a macro potential $\Phi(x)$, which will separate electrons and holes creating a space-charge region at the interface. This charge separation results also in a built-in voltage V_D compensating the macro potential. Adopted from Ref. 51.

due to negatively-charged acceptor defects in p-doped materials and positively-charged donor defects in n-doped materials. Knowledge of the band alignment can help to ensure that we facilitate such a situation and it can also be employed to find the right doping level, because if a material is doped too much, we will have a higher loss due to Auger recombination. In particular, the knowledge of the band alignment is important for heterogeneous p-n junctions that are composed of two different semiconductors. In our high-throughput screening, we predicted the natural band alignment, which refers to the alignment without doping and interface effects.

3.1.3 The SpeedCIGS-project

The search for a transparent p-type semiconductor was realized within the SpeedCIGS-project. CIGS is a synonym for the four elements copper, indium, gallium, and selenium. It is used as absorber material in thin film solar cells. As the name of the project suggests, one of the main goals is to speed up the CIGS solar cell production process. Another goal is the development of a perovskite-CIGS tandem solar cell. As described before, a tandem solar cell is an important step to overcome the inherent efficiency limit of a single-junction solar cells. In order to achieve this goal, a suitable p-type semiconductor needs to be found. The use of perovskite imposed one problematic constraint for the p-type semiconductor: In order to avoid damaging the perovskite, the substrate temperature should not rise above 250 °C. This already excludes a lot of the commonly employed p-type semiconductors in solar cells. Nowadays, spiro-OMeTAD is used as hole transport layer in perovskite solar cells. However, its high synthetic cost of $600\,\$/g$ renders it uninteresting.[52] Another issue with such perovskite solar cells, is the requirement of dopants, which are detrimental to the long-term stability, but have to be used to ensure good performance.[52] This motivated the search for a new material as hole transport layer.

3.1.4 Overview of the methodology

The work on binary chalcogenides was finished early on in the project.[53] In this article, mainly the original approach was described and used. Therefore, it can be used as a reference to illustrate the state of the methodology before our new approach was established. However, some of the improvements of the latter were already described in that article. We will start with considering the necessary steps that are required for the theoretical identification of a promising transparent p-type semiconductor.

The first step is the identification of candidates. The compound space for binary and especially ternary compounds is huge. Many scientists are working on synthesizing new materials, therefore it seems appropriate to use a database based on experimental structures. In this step, the band gap and conditions on the choice of elements can be used to reduce the list of compounds. Depending on the database (theoretical or experimental) and on the provided data, also the atoms in the unit cell, the stability of the material and the hole effective mass can be employed to select promising compounds. In the older approach, a list of semiconductors compiled by Strehlow *et al.*[54] was used

to identify binary chalcogenides. In order to keep up with the steadily growing number of synthesized compounds, it was necessary to rely on a state-of-the-art database, which would ideally offer an interface to allow data mining *via* scripting.

The second step is the calculation of some missing parameters: either the effective masses and stability in case of the older approach or the band gap for the newer one. For this step, the Effective Mass Calculator (EMC) code[55] was employed in order to calculate the curvature of the valence band, which is denoted as hole effective mass in the previous approach. For the new approach, we additionally had to calculate the band gaps, owing to their underestimation with the PBE[56] functional.[57] This step left us with the task of realizing the effective mass and band gap calculations in a more automated way, which would enable us to screen more efficiently.

The third step is the computation of the defect chemistry in order to determine if the material can be doped p-type (intrinsic defect chemistry) and with which element (extrinsic defect chemistry). This last step also needs to be automated, since the manual creation of around 50 calculations per binary and some hundreds per ternary compound is cumbersome. Additionally, there are also requirements for tandem solar cell applications to consider for example band alignment, carrier concentration and lattice matching. Owing to the importance of determining the band alignment, we had to come up with a suitable method. Another parameter of interest is the calculation of the achievable carrier concentration. In experiments, the thin films are grown *via* epitaxy. Therefore, lattice matching is also of interest, which might also be used in the screening process. To summarize, we identified the following tasks:

- Identify and employ an up-to-date database
- Automate the hole effective mass calculations
- Automate the band gap calculations
- Find a way to obtain information on the band alignment
- Automate the defect calculations
- Find a way to estimate the carrier concentration
- Calculate lattice matching in order to enable epitaxy

The work on these tasks will be described in the next sections. However, automation of band gap calculations and band alignment are described in one section owing to their closeness. Furthermore, we could not finish the work on the last two points of the list. On the one hand, the prediction of carrier concentrations did turn out to be more complicated than initially thought.[58] On the other hand, lattice matching would have been possible,[59] but we did not implement it, as it was not much of a concern in the project and owing to the limited time.

3.1.5 Meaning of workflow and high-throughput in this work

In our case, a workflow is in most cases a series of calculations in order to calculate a certain property. Fig. 3.2 shows the workflow for calculating the effective mass of $CaCuO_2$. In order to determine the effective mass with Boltzmann transport theory, we need to perform the following: optimize the structure, a static calculation, another calculation on a homogeneous k-point mesh and finally a calculation with BoltzTrap.[60] Additionally, a band structure calculation along a path through the Brillouin zone can also be conducted in order to compare results.

High-throughput refers to implementing a workflow for the investigation of several compounds. In principle, it could of course be achieved by manually setting up the required calculations. However, this is prone to errors and cumbersome for hundreds or even thousands of compounds. Therefore, automation comes into play, so the PC is handling the described work. The example workflow of Fig. 3.2 can be initiated by typing "atwf add −s bandstructure_boltztrap.yaml −m mp−11019" We are using atomate,[61] so atwf is used as abbreviation for atomate workflow. With the add command we add a workflow for the material with the Materials Project ID mp-11019, to the database. The required instructions are specified in the boltztrap.yaml file, will then be uploaded to the database and the steps of the workflow are computed automatically, when resources are available. The results would ideally be uploaded to another database, so that we just have to look up the results. Of course the initialization of the workflow can also be achieved by scripting, so that data mining and computation can be linked. This would enable the computation of properties for thousands of compounds. In fact, a modified version of this workflow was used to create a database of 48.000 compounds.[62] We did not link data mining and computation and we also did not upload our results into a databases, since we had to investigate just some hundred compounds.

3.1.6 Screening procedure

Our screening procedure is shown in Fig. 3.3. Starting from the Materials Project Database,[63] it takes into account effective mass data from Ref. 62 and we calculate the band gap and band alignment as well as the intrinsic and extrinsic defect chemistry in a final step. In this chapter, we will elucidate the steps in chronological order starting with the choice of a database. We will then explain the effective mass calculation respectively its retrieval. After elucidating the band gap and natural band alignment calculations, we finish this chapter with a clarification on our defect chemistry screening. The mentioned methods are state-of-the-art and were recently reviewed by Brunin *et al.*[64]

3.2 Database

The best starting point for our high-throughput search of an transparent p-type semiconductor is a database, in which previous calculations are stored. This already allows us to sort out metals and semiconductors with a small band gap. Even better would be a database, which would help us in the design of our own high-throughput workflows.

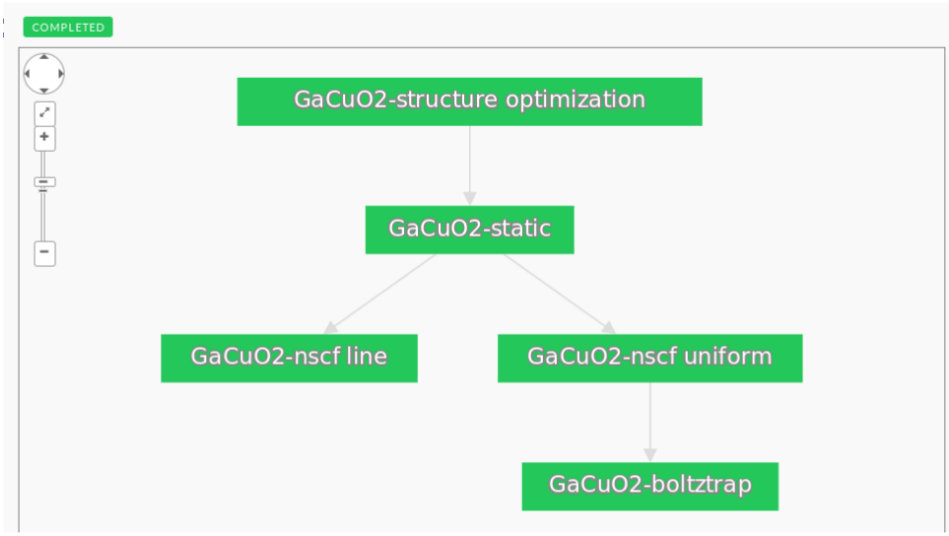

Figure 3.2: Atomate[61] effective mass workflow using BolzTrap[60] as it was employed in the study of Ricci *et al.*[62] After a structure optimization, a static calculation is used to converge the charge density. Subsequently, k-points are sampled on both a uniform mesh and a path through the Brillouin zone. The mesh data is used in boltztrap, whereas the line data is employed for validation in a later step.

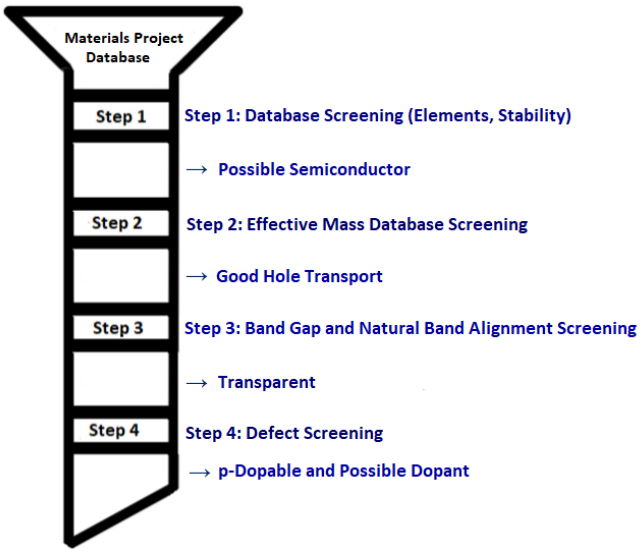

Figure 3.3: Filtering procedure of our *in silico* screening for finding a transparent p-type semiconductor. Starting from the Materials Project Database,[63] we first obtain the effective mass data from Ref. 62. Then we calculate the band gap as well as the natural band alignment. Finally, the intrinsic and extrinsic defect chemistry is determined.

For this purpose, we profited from the development of theoretical databases and decided to employ such a database, since they appeared to be more promising than experimental ones for starting our own theoretical investigations.

In January 2016, we based the selection of the database mainly on an article written by Lianshan Lin.[65] In this article, several theoretical databases were introduced. In opposition to their experimental counterparts, which were founded mainly in 20th century or even 19th century, if we also include book series like Landolt-Börnstein, theoretical databases began to emerge during the 21th century. One main reason is the computational demand of DFT calculations, which was in the nineties quite a bottleneck for high-throughput calculations. However, the increase in computational power and the development of more efficient algorithms alleviated this and played a major role in the emergence of theoretical databases.[65]

The advantages of theoretical databases are the speed, in which they can be developed, and the possibility to quickly screen existing and hypothetical compounds. It is hardly possible to synthesize and characterize all imaginable compounds, because their number increases fast with the number of different atoms in the molecular formula. In such a case, theoretical databases can speed up the process of finding suitable compounds. Traditionally, the design of a material for a specific application took between 10 - 20 years, whereas with the use of databases and high-throughput calculations it is expected to be realizable in 2 - 3 years.[63,65]

To come back to the original problem of selecting a suitable database, the second criterion of having also the possibility to create and execute our own workflows is drastically reducing the potential candidates. One of the better known databases is NoMad, a European database.[66] It specializes in the collection of data and for this purpose, it is relying on existing high-throughput schemes for generating the required data. At that time, also the handling of data stored in the NoMad repository was bothersome due to a missing Restful-Application Programming Interface (API), which was later added. Considering all these points, NoMad was not of interest for us anymore.

Based on Lin's article,[65] this leaves Aiida,[67] Materials Project,[63] Materials Simulation Toolkit (MAST)[68] and Open Quantum Materials Database(OQMD)[69] with the qmpy software for workflow managing as potential candidates. MAST as well as Aiida are suitable of workflow managing, but do not provide data on already calculated compounds, which renders both of them uninteresting for us. In case of OQMD, it is mostly made up of theoretical compounds. At that time, about 10 % of the compounds were based on data from the Inorganic Structure Database (ICSD),[70] whereas the remaining 90 % were purely theoretical data.[65] OQMD contained roughly 200.000 compounds at that time, meaning *ca.* 20.000 compounds based on ICSD data. With roughly 60.000 compounds based on ICSD data, Materials Project was the most interesting data base and software framework for our undertaking. It has to be mentioned that our interest in ICSD based data was motivated by a remark of our project partners to focus on already synthesized compounds.

3.2.1 Materials Project

The Materials Project was launched in November 2011 as core program of the Materials Genome Initiative in the USA.[63] From the beginning, it was planned and executed as a large-scale cooperation between computer science as well as experimental and theoretical materials science.[63] This led to an open mindset about sharing data and software together with an openness for further collaborations. Its sophisticated web interface and an early implementation of an RESTFUL as an application programming interface (API) is proof for this openness.[71]

On 21/06/2019, the Materials Project was hosting data sets for about 120612 inorganic compounds. Among those compounds, 52366 materials have computed values for band structure, 13621 elastic tensors and 3003 piezoelectric tensors. Compared to aflowlib, which is stating to have data for 2844669 compounds, the number of compounds in the Materials Project appears to be small. However, going into detail, we recognize that only 30031 compounds in aflowlib are ternaries compared to 56102 in the Materials Project. A major part (1963013) of the compounds in aflowlib are quaternaries, but we decided to focus on binaries and ternaries.

The choice of Materials Project was also sensible considering the properties we were interested in. The work on the effective mass database by Ricci *et al.*[62] saved as some computing time, as with that database the effective mass became a criterion, which just could be looked up. For the branch point and defect calculations, we also used software developed within the Materials Project. Atomate[72] and Fireworks[73] allowed the automation of the branch point workflow and a routine in Matminer[74] enabled parsing of the branch point results. PyCDT[75] was used for creating and parsing the defect calculations. In the future, even more concepts from the Materials Project could be employed. For example, the capability of calculating Pourbaix diagrams[76] could lead to a better understanding and improved prediction of the stability for our investigated materials.

3.3 Stability

In order to judge the stability of compounds, the formation energy of several phases has to be calculated and compared. The convex hull is then simply constructed by connecting the lowest-lying phase with the elements. However, if another phase is below these drawn lines, we also have to consider that point. In the end, no phase lies below the drawn lines, *i.e.* the convex hull, and all "stable" phases are on it. One of the challenges with this approach is the identification of all relevant phases, as in principle and without imposing criteria the number of phases can be infinite. But if we limit ourselves to the known phases, we can employ databases to identify the relevant ones. Therefore, the formation energy of phases and the convex hull can be extracted from the MPDB, see Fig. 3.4 as an example.[63]

This phase diagram also illustrate some of the shortcomings with that approach. Immediately, we can see the absence of K_3P, which lies 0.01 eV above the convex hull. Therefore, this compound should decompose into K_4P_3 and potassium. Owing to this,

the convex hull criterion is used in general in combination with a cutoff energy, for example 0.1 eV.[77] It is also interesting that K_4P_3 lies on the convex hull, as this compound explodes after some weeks, when it is stored in a Schlenk vessel.[78] The authors suspected K_4P_3 to be responsible for the reaction.[78] The crucial question is therefore, if this is caused by the decomposition of the compound or the reaction with external elements, for example oxygen or hydrogen. If it is the former, this material should not have been on the convex hull and it would have to be checked, if the PBE functional is able to describe the chemistry of binaries made of potassium and phosphorus correctly. For example, this functional is known to poorly describe transition metal oxides.[79] This shortcoming can be corrected by using PBE + U.[79,80]

The second case, *i.e.* reaction with an external element, is a blind spot of the convex hull criterion. The convex hull is judging stability with respect to the present elements, so potassium and phosphorus for our material. It will not tell us if the compounds are stable with respect to moisture or air and in particular oxygen. If we look into the literature, we notice that except for KP_{15} all of the mentioned compounds are sensitive to moisture or air.[78,81–85] Even K_3P will ignite, when it comes in contact with air.[81] In this regard, the calculation of a Pourbaix diagram might be required.[76] Such a diagram is per definition open to oxygen and hydrogen. It shows the most stable phases in dependence of pH value and voltage. However, the problem with this diagram is that it is only valid for solids in contact with water. Although for the intended application in solar cells, the contact with water should be minimal, we nonetheless need a metric to judge stability towards moisture and air. As suggested by Woods-Robinson *et al.*, a cutoff based on the Pourbaix diagram (pH = 7 and 0 voltage) might be defined.,[86] However, in the presented studies, we performed a literature survey in order to judge a compounds stability towards moisture and air. This is in addition to the stability assessment based on the convex hull criterion, which is directly integrated in our screening approach.

3.4 Effective mass

The theory in this section is mainly based on "Festkörperphysik"[51] written by Rudolf Gross and Achim Marx and on the article about BoltzTrap,[60] which was written by Georg K. H. Madsen and David J. Singh. Therefore, further details can be found in the cited publications and references therein.

3.4.1 Boltzmann transport theory

In general, transport processes can be described by employing an equation, which is composed of three terms accounting for diffusion, directed transport and loss mechanisms:[51]

$$\frac{\partial f}{\partial t} = \left(\frac{\partial f}{\partial t}\right)_{Diffusion} + \left(\frac{\partial f}{\partial t}\right)_{Directed\_Transport} + \left(\frac{\partial f}{\partial t}\right)_{Scattering}. \tag{3.4}$$

Examples for the latter are side reactions in matter transport and scattering in electron transport. In our case, we have to know the Fermi surface and assume a well defined

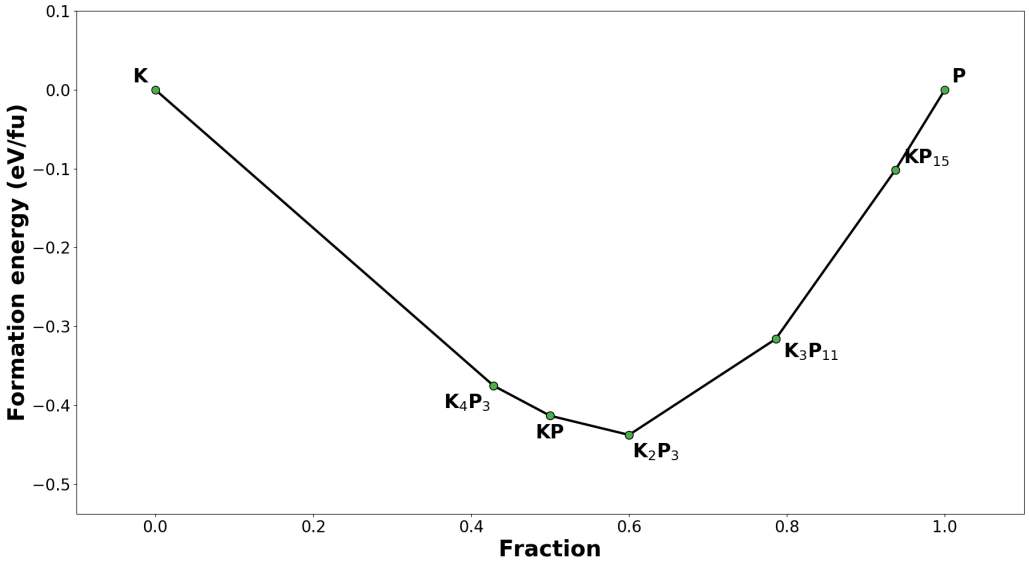

Figure 3.4: Phase diagram of binaries containing potassium and phosphorus. All shown phases with the exception of KP_{15} are unstable with respect to oxygen and hydrogen, even though they are on the convex hull. Furthermore, K_3P (not shown) is slightly above the convex hull and therefore not considered to be stable. The phase diagram was created by and with data from the MPDB.[63]

momentum $\vec{k}$ of the electrons. We require that the separation of the centers of scattering is much larger than the Fermi wavelengths ($\lambda_F << l$) with l being the averaged lengths, which a electron can travel before undergoing scattering. We also have to assume that the material exhibits a symmetric Boltzmann distribution of states in momentum space:

$$f_0(\epsilon(\vec{k})) = \frac{1}{e^{\frac{\epsilon(\vec{k})-\mu}{k_B T}} + 1}. \tag{3.5}$$

In this equation, μ is the chemical potential and ϵ is used for the energy, so that it is not mistaken to be the electric field E. The change in the distribution is approximately:

$$\frac{\partial f(\vec{r},\vec{k},t)}{\partial t} = -\vec{v}(\vec{k}) \cdot \nabla_{\vec{r}} f + \frac{1}{\hbar} \nabla_{\vec{r}} \epsilon(\vec{k}) \cdot \nabla_{\vec{k}} f + \left(\frac{\partial f(\vec{r},\vec{k},t)}{\partial t} \right)_{Scattering}. \tag{3.6}$$

The first term, $-v(\vec{k}) * \nabla_{\vec{r}} f$, describes the change of the distribution due to variation in space and is called diffusion term. The directed transport term, $\frac{1}{\hbar} \nabla_{\vec{r}} \epsilon(\vec{k}) \cdot \nabla_{\vec{k}} f$, describes the change of the distribution due to the influence of external fields. As an example, the effect of electromagnetic fields can be considered by assuming $\nabla_{\vec{r}} \epsilon(\vec{k}) = -e(\vec{E} + \vec{v} \times \vec{B})$. The last term, $\left(\frac{\partial f(\vec{r},\vec{k},t)}{\partial t} \right)_{Scattering}$, takes scattering into account. This term is quite complicated and would lead to an integro-differential equation, which cannot be solved easily.

In order to avoid this, further assumptions can be made. We can use a linearized form, which will limit us to cases close to the equilibrium and we can use an approximation based on an averaged relaxation time. Details of the linearization can be looked up in ref. 51. Assuming that both the chemical potential and the temperature are well defined for every point, a new distribution function $g(\vec{k},\vec{r},t)$ can be introduced. For small values of this function, we obtain:[51]

$$g(\vec{k},\vec{r},t) = \delta f(\vec{k},\vec{r},t) - \frac{\partial f_0}{\partial \epsilon}\left[\delta\epsilon(\vec{r},t) - \delta\mu(\vec{r},t) - \frac{\epsilon(\vec{k})-\mu}{T}\delta T(\vec{r},t)\right] \tag{3.7}$$

Assuming that the change caused by external fields is small, *i.e.* $\epsilon(\vec{k}) = \epsilon_0(\vec{k}) + \delta\epsilon(\vec{k})$ and $\nabla_{\vec{r}}\epsilon(\vec{k}) = \nabla_{\vec{r}}\delta\epsilon(\vec{k})$, we can insert this approximation into Equation 3.6 yielding:

$$\begin{aligned}\frac{\partial f(\vec{k},\vec{r},t)}{\partial t} = -\vec{v}\cdot\nabla_{\vec{r}}\left[\delta f(\vec{k},\vec{r},t) - \frac{\partial f_0^{loc}(\vec{k},\vec{r},t)}{\partial\epsilon}\nabla_{\vec{r}}\delta\epsilon\right] \\ +\frac{1}{\hbar}\nabla_{\vec{r}}\delta\epsilon\cdot\nabla_{\vec{k}}\,g(\vec{k},\vec{r},t) + \left(\frac{\partial f(\vec{k},\vec{r},t)}{\partial t}\right)_{Scattering}.\end{aligned} \tag{3.8}$$

Explicitly considering the influence of electromagnetic fields $\nabla_{\vec{r}}\delta\epsilon(k) = -e(\vec{E}+\vec{v}\times\vec{B})$, we obtain for the stationary state ($\frac{\partial f}{\partial t} = 0$):

$$\begin{aligned}-\frac{\partial f_0}{\partial\epsilon}\vec{v}\cdot\left[e\vec{E} + e(\vec{v}\times\vec{B}) - \nabla\mu - \frac{\epsilon(\vec{k})-\mu}{T}\nabla T\right] - \vec{v}\cdot\nabla_{\vec{r}}\,g \\ -\frac{1}{\hbar}\nabla_{\vec{k}}\,g\cdot\left[e\vec{E} + e(\vec{v}\times\vec{B})\right] + \left(\frac{\partial f}{\partial t}\right)_{Scattering} = 0.\end{aligned} \tag{3.9}$$

With $(\vec{v}\times\vec{B})\cdot\vec{v} = 0$ and neglecting $\nabla_{\vec{k}}\,g\cdot\vec{E}$, which is of second order in $\vec{E}$, we can simplify the equation to:

$$\frac{\partial f_0}{\partial\epsilon}\vec{v}\cdot\left[e\left(\vec{E} - \frac{\nabla\mu}{e}\right) - \frac{\epsilon(\vec{k})-\mu}{T}\nabla T\right] + \vec{v}\cdot\nabla_{\vec{r}}\,g + \frac{e}{\hbar}\nabla_{\vec{k}}\,g(\vec{v}\times\vec{B}) = \left(\frac{\partial f}{\partial t}\right)_{Scattering}. \tag{3.10}$$

We still have not dealt with $\left(\frac{\partial f}{\partial t}\right)_{Scattering}$. For this term, the relaxation time approximation can be used:

$$\left(\frac{\partial f}{\partial t}\right)_{Scattering} = -\frac{f(\vec{k}) - f^{loc}(\vec{k})}{\tau(\vec{k})} = -\frac{g(\vec{k})}{\tau(\vec{k})}. \tag{3.11}$$

Within this approximation, we are describing the scattering processes with an averaged relaxation time τ. Based on these two approximations, we can start to derive the

transport properties. For this, we will assume a given electric field $\vec{E}$, a defined temperature $T(\vec{r},t)$ and a defined chemical potential $\mu(\vec{r},t)$. In the absence of magnetic fields ($\vec{B}=0$) and charges e, we can rewrite Eq. 3.10:

$$g(\vec{k}) = -\frac{\partial f_0}{\partial \epsilon}\tau(\vec{k})\vec{v}(\vec{k}) \cdot \left[e\left(\vec{E} - \frac{\nabla \mu}{e}\right) - \frac{\epsilon(\vec{k})-\mu}{T}\nabla T \right]. \tag{3.12}$$

With $\mathcal{A} = \left[e\left(\vec{E} - \frac{\nabla \mu}{e}\right) - \frac{\epsilon(\vec{k})-\mu}{T}\nabla T \right]$, we obtain:

$$g(\vec{k}) = -\frac{\partial f_0}{\partial \epsilon}\tau(\vec{k})\vec{v}(\vec{k}) \cdot \mathcal{A}. \tag{3.13}$$

Now turning to the current density J, which can be obtained by integrating the product of carrier density, carrier velocity and probability of occupation over all states:

$$\vec{J_q} = \frac{1}{4\pi^3}\int e\vec{v}(\vec{k})f(\vec{k})d^3k. \tag{3.14}$$

Based on the definition of $g(\vec{k},\vec{r},t)$[51] and because of $\int e\vec{v}(\vec{k})f_0(\vec{k})d^3k \equiv 0$, we can write:

$$\vec{J_q} = \frac{1}{4\pi^3}\int e\vec{v}(\vec{k})g(\vec{k})d^3k. \tag{3.15}$$

Employing the relation $d^3k = dS_\epsilon dk_\perp = dS_\epsilon \frac{d\epsilon}{\nabla_{\vec{k}}\epsilon} = dS_\epsilon \frac{d\epsilon}{\hbar\nu(k)}$, we can rewrite the volume integral in k-space as an integral over shells of constant energy. Assuming a small temperature smearing ($k_BT << \epsilon_F$), we can approximate $-\frac{\partial f_0}{\partial \epsilon}$ with $\delta(\epsilon - \epsilon_F)$. After these steps, only an integral over the Fermi surface remains:

$$\vec{J_q} = \frac{1}{4\pi^3}\frac{e}{\hbar}\int_{\epsilon=\epsilon_F} dS_F \frac{\tau(\vec{k})\vec{v}(\vec{k})\vec{v}(\vec{k})}{\nu(k)} \cdot \mathcal{A}. \tag{3.16}$$

In this equation, the expression $\vec{v}(\vec{k})\vec{v}(\vec{k})$ is an outer product. Inserting the definition of $\mathcal{A}$, we obtain the desired expression for the current density:

$$\begin{aligned} \vec{J_q} = &\frac{1}{4\pi^3}\frac{e^2}{\hbar}\int_{\epsilon=\epsilon_F} dS_F \frac{\tau(\vec{k})\vec{v}(\vec{k})\vec{v}(\vec{k})}{\nu(k)} \cdot \left[\vec{E} - \frac{\nabla\mu}{e}\right] \\ &+\frac{1}{4\pi^3}\frac{e^2}{\hbar}\int_{\epsilon=\epsilon_F} dS_F \frac{\tau(\vec{k})\vec{v}(\vec{k})\vec{v}(\vec{k})\frac{\epsilon(\vec{k})-\mu}{T}}{\nu(k)} \cdot [-\nabla T]. \end{aligned} \tag{3.17}$$

If we set $\nabla T = 0$, we can use $J_q = \hat{\sigma}\vec{E}$ to identify the conductivity tensor as:

$$\hat{\sigma} = \hat{\sigma}(\epsilon_F) = \frac{1}{4\pi^3}\frac{e^2}{\hbar}\int_{\epsilon=\epsilon_F} dS_\epsilon \frac{\tau(\vec{k})\vec{v}(\vec{k})\vec{v}(\vec{k})}{\nu(k)}. \tag{3.18}$$

In the simple case of a cubic crystal system, the conductivity tensor reduces to a scalar. By further assuming that $\vec{E}$ and $\vec{J_q}$ are pointing in x-direction ($\vec{v}(\vec{k})\vec{v}(\vec{k})\vec{E} = v_x^2 E$, where v_x^2 is one third of the absolute value of the square of the total velocity v^2), we arrive at:

$$\sigma = \frac{1}{4\pi^3}\frac{e^2}{\hbar}\frac{1}{3}\int_{\epsilon=\epsilon_F} \tau(\epsilon_F) v_F dS_\epsilon. \tag{3.19}$$

Using $\nu_F = \hbar k_F/m$, $\int_{\epsilon=\epsilon_F} dS_\epsilon = 4\pi k_F^2$ and $n = \frac{k_F^3}{3\pi^2}$, we obtain the well known expression:

$$\sigma = \frac{ne^2\tau}{m}. \tag{3.20}$$

3.4.2 Boltzmann transport theory in computational materials science

The group velocity $\vec{v}(\vec{k})$ can be directly computed from the band structure:

$$\vec{v}(\vec{k}) = \frac{1}{\hbar}\frac{\partial \epsilon_{\vec{k}}}{\partial \vec{k}}. \tag{3.21}$$

Owing to this, Boltzmann transport theory can be easily applied by theorist. One problem is that the band structure is computed on a k-point mesh only, but we need the whole band structure. To obtain the latter, BoltzTrap[60] is computing a Fourier expansion of the band structure energy by using star functions. The star functions are constrained to the band energies and additional freedom is gained, since more star functions than band energies are used. This is then employed to minimize a roughness function, which will lead to a suppression of oscillations between data points. Further details can be looked up in Ref. 60. The other problem is the relaxation time, as we should be aware that the constant relaxation time is a strong approximation and often not fulfilled in experiment.

After calculating the group velocity, we still need information on the chemical potential of electrons. This tends to be cumbersome, as this chemical potential is defined by the defect chemistry of the material, which requires a lot of calculations. In the following, we estimate the chemical potential and calculate the transport properties by either setting directly this potential or the carrier concentration, which will in the end also give a chemical potential. The effective mass μ^* can then be computed by using Eq. 3.20 and by employing μ^* instead of m.

$$\sigma = \frac{ne^2\tau}{\mu^*} \iff \mu^* = \frac{ne^2\tau}{\sigma}. \tag{3.22}$$

3.4.3 Methods based on calculating the band curvature

The definition of the effective mass offers another approach for its determination. The effective mass tensor is symmetric and it can be transformed to a coordinate system which is oriented along its principal axes. In the case of three equal values, we can simply write:

$$\frac{1}{\mu^*(k)} = \frac{1}{\hbar^2}\frac{d^2\epsilon_n(k)}{dk^2}. \tag{3.23}$$

In this equation, n is the number of bands. For the hole effective mass, we have to investigate a valence band and for electrons a conduction band. Therefore, $d^2\epsilon_n(\vec{k})/dk^2$ is nothing else than the curvature of the valence or the conduction band. The hole effective mass can be computed by fitting a parabola to the valence band maximum and for electrons by fitting a parabola to the conduction band minimum.

More in general, by fitting parabolas along the directions of the principal axes, the components of the effective mass tensor can be determined:[55]

$$\epsilon_n(\vec{k}) = \alpha_1 k_x^2 + \alpha_2 k_y^2 + \alpha_3 k_z^2; \tag{3.24}$$

$$\mu^*_{xx} = \frac{\hbar}{2\alpha_1}; \quad \mu^*_{yy} = \frac{\hbar}{2\alpha_2}; \quad \mu^*_{zz} = \frac{\hbar}{2\alpha_3}. \tag{3.25}$$

Going one step further, finite differences can be employed to calculate all of the second and mixed derivatives. This is implemented in the Effective Mass Calculator (EMC) code.[55] Without simplifications, we would have to write:

$$\left(\frac{1}{\mu^*}\right)_{ij} = \frac{1}{\hbar^2}\frac{\partial^2\epsilon_n(\vec{k})}{\partial k_i \partial k_j}, \quad i,j = x,y,z; \tag{3.26}$$

$$\frac{d^2\epsilon}{dk^2} = \begin{pmatrix} \frac{d^2\epsilon}{dk_x^2} & \frac{d^2\epsilon}{dk_x dk_y} & \frac{d^2\epsilon}{dk_x dk_z} \\ \frac{d^2\epsilon}{dk_y dk_x} & \frac{d^2\epsilon}{dk_y^2} & \frac{d^2\epsilon}{dk_y dk_z} \\ \frac{d^2\epsilon}{dk_z dk_x} & \frac{d^2\epsilon}{dk_z dk_y} & \frac{d^2\epsilon}{dk_z^2} \end{pmatrix} \tag{3.27}$$

The effective mass tensor is symmetric, so there are only six independent values.

3.4.4 Finding a suitable method for high-throughput calculations

For our project, it was important to perform the effective mass calculation in an automatic fashion in order to screen some hundreds of compounds. As part of the Materials Project,[63] atomate[72] is offering a variety of workflows for computing different properties and a workflow for computing electronic transport properties by using BoltzTrap[60] can also be found. This enables the determination of both the effective mass tensor and its three principal axis components. We decided to compare the results of this workflow with the ones of EMC.[55] However, the work with the atomate workflow was discontinued due to the publication of the dryad database.[62] This database was generated by using Materials Project data and a modified atomate workflow. Owing to this, we stopped working with that workflow and employed instead the database to obtain the hole effective masses.

The original comparison can be found in Tab. 3.1, in which the effective masses are determined as harmonic averages. This benchmark was made by investigating selected binary compounds. The EMC data was provided by Dr. Ramya and Dr. Mirhosseini.

We had to leave some gaps, since only compounds with the same symmetry can be compared and the data is not directly based on the Materials Project. Overall, differences between the two methods can be expected. On the one hand, EMC requires the identification of the valence band maximum in order to estimate its curvature. It is also not able to account for transport involving multiple bands and pockets. Furthermore, band crossings are problematic. On the other hand, Boltzmann transport theory faces the problem of the constant relaxation time approximation.

In most cases, the harmonic average is equal to the three principal axis values. This can be traced back to the fact that we have a structure with a simple cubic symmetry leading to three equal values. We should also mention that the data reported in the dryad database was calculated at 300 K and for a doping level of $10^{18}\,\mathrm{cm}^{-3}$, whereas we assumed a doping level of $10^{20}\,\mathrm{cm}^{-3}$ in the workflow. This explains smaller deviations. Larger deviations might be caused by stopping to work on this workflow. Therefore, we did not validate the band structure determined with BoltzTrap with the band structure computed on high symmetry lines. In the case of the two missing values, the computation of the band structure got stuck and we stopped the workflow manually. The hole effective masses calculated with EMC are lower than the values computed with BoltzTrap. Only AgCl with a difference of 0.36 eV is worrisome. Based on these results, we decided to use the dryad database for our search. However, we considered to relax the criterion for the effective mass, the values from BoltzTrap are higher than the ones calculated with EMC.

Some time after the initial release of the dryad database, it was in incorporated into a Materials Project user database, but since then it was not updated. During this time, the Materials Project Database grew from 60.000 to more than 120.000 compounds resulting in more and more compounds without effective mass data. For future high throughput studies, the computation of effective masses will become again an issue and we need to decide which method, *i.e.* EMC or BoltzTrap, we want to employ. A more general problem is the fact that transport does not have to occur *via* the valence band in case of hole or the conduction band in case of electrons. Instead, it can also take place by the formation of small polarons.[64] This could lead to new screening strategies that are required for the identification of hole conducting materials.

3.5 Band gap and band alignment via branch point

As mentioned in the introduction, we worked on the problem of automating both band gap calculations and determination of the band alignment. It did turn out that both tasks could be tackled by adopting and automating a workflow for electronic structure calculations with a homogeneous k-point mesh employing a hybrid functional. However, one should keep in mind that the challenge of theoretically predicting band gaps is well known in literature.[57,87] The focus of this chapter lies on the description and validation of the band alignment calculations *via* the branch point concept.[88–91] For the validation, we had to ensure that the employed k-point mesh is sufficiently dense in order to obtain a reliable value for the HSE-band gap.

Table 3.1: Effective mass benchmark for selected halides and pnictides. For each compound, its Materials Project Database ID, space group, harmonic average of the hole effective mass calculated with the Effective Mass Calculator,[55] harmonic average of the hole effective mass taken from dryad database,[62] and harmonic average of the hole effective mass calculated with our modified workflow are given.

Compound	MPDB ID	Space group	$\overline{m}_h^*$ (m_e) EMC	$\overline{m}_h^*$ (m_e) MP	$\overline{m}_h^*$ (m_e) WF
AgBr	mp-866291	$F\bar{4}3m$		1.25	1.25
AgCl	mp-22922	$Fm\bar{3}m$	0.47	0.83	0.86
AgI	mp-22925	$F\bar{4}3m$	0.80	0.92	0.90
AgN_3	mp-2247	Ibam	0.80	0.80	0.83
AlP	mp-1550	$F\bar{4}3m$	0.56	0.56	
BiI_3	mp-22849	$R\bar{3}$		5.33	5.35
BP	mp-1479	$F\bar{4}3m$		0.34	0.36
CuCl	mp-22914	$F\bar{4}3m$	1.59	1.78	
CuBr	mp-22913	$F\bar{4}3m$		1.21	1.33
CuI	mp-570136	P3m1		2.74	3.01
CuI	mp-22895	$F\bar{4}3m$	0.75	0.86	0.76
GaP	mp-2490	$F\bar{4}3m$	0.41	0.45	0.44
InP	mp-20351	$F\bar{4}3m$		0.53	0.51
Mg_3N_2	mp-1559	$Ia\bar{3}$		4.78	4.66
ZnP_2	mp-11025	$P4_32_12$	0.48	0.52	0.61

3.5.1 Band alignment via branch point

Band alignment is rather important in order to create a functioning p-n-junction. For this purpose, we have at least to consider the material and the doping level. Furthermore, we also need the correct size of the band gap for the band alignment. Another requirement, which is not apparent from the example in the introduction, is the knowledge of the formed interface.

Traditionally, a theorist would either calculate the band alignment by using a model for the whole interface or by employing an approach based on the determination of ionization potential (IP) and electron affinity (EA), which are calculated by using a slab model of the material in vacuum. These latter calculations are based on the Bardeen limit, so no charge transfer between the interfaces is allowed. In screening studies, this would be done for a reduced set of candidates at the end of the screening.[92] An alternative approach would be to use the collected data of IPs and EAs data, which was for example realized by Butler *et al.*[59] However, this approach would already lead to a strongly reduced list of candidates, due to the small size of IP and EA data. Therefore, this method was not of interest for our task of establishing a general workflow. Having these two traditional approaches in mind, we searched for a methodology to obtain information on the band alignment from band structure calculations of the bulk materials.

The exponential decay of the wave function at the interface between solid and vacuum is a well known result. In the cases of semiconductor-metal or semiconductor-semiconductor interfaces, this is more complicated. First, we should note that solving Schrödinger's equation for complex wave vectors leads to virtual gap states.[88,89] These gap states are mainly donor-like near the valence band maximum and mainly acceptor-like near the conduction band minimum. The branch point energy is the energy, where the spectral weight changes its character.[89] Is the Fermi energy above the branch point, we will have negatively charged interface states, but positively charged states, when the Fermi energy is below the branch point. In the case that both energies are equal, we have no charge at all.

Therefore, the branch point can be seen as a charge neutrality level for the interface. This leads to the central assumption of the branch point concept: it is based on the Schottky limit, where charge transfer is allowed and the alignment is calculated for uncharged interfaces. This allows to employ the bulk band structure making this approach computationally very efficient. Tersoff was one of the first to apply the concept of branch point in order to calculate the band alignment of Si, Ge and some III-V and II-VI semiconductors.[93] He employed the local density approximation in combination with a rigid shift of conduction bands in order to match experimental gap values. To find the branch point, he used the energy at which the cell-averaged real-space Green's function of the band structure changes sign.

Cardona and Christensen[90] employed Baldereschi's concept[94] of mean value k-points. The mean value k-point of a semiconductor is the k-point where any periodic function of the wave vector is a good approximation to the averaged value of that function over the whole Brillouin zone. Christensen and Cardona also employed the LDA level of theory and used the average of the top two valence bands and lowest two conduction bands to

correct the size of the gap.[90] Mönch also used Baldereschi's concept in combination with a tight binding approximation for the band structure calculations.[89]

Baldereschi's concept of a mean value k-point offers also another route to calculate the branch point by using the mean value of all points in the Brillouin zone. This was realized by Schleife *et al.* in 2009.[91] They defined the branch point energy in the following way:

$$\varepsilon_{BP} = \frac{1}{2N_K}\sum_{k}^{N_K}\left[\frac{1}{N_{VB}}\sum_{i}^{N_{VB}}\varepsilon_i(k) + \frac{1}{N_{CB}}\sum_{j}^{N_{CB}}\varepsilon_j(k)\right]. \tag{3.28}$$

In this equation, the number of valence bands (N_{VB}) and the number of conduction bands (N_{CB}) are free parameters and need to be chosen accordingly. In the original article, this definition was used in combination with GW, *i.e.* an approach based on many-body perturbation theory to determine the band structure.[91] The work of Deàk *et al.*[95] inspired us to use the HSE hybrid functional[96] for high-throughput calculations of the branch point. However, we are not the first who used this concept in a high-throughput study, as it was employed by Sarmadian *et al.*[97,98] in two studies a few years before.

3.5.2 Implementation

In matminer,[74] a routine for analyzing VASP calculations using the definition of Schleife *et al.* was implemented. In addition, we worked on a workflow for band gap calculations, which had been defined in atomate.[61] We modified this workflow in order to sample a homogeneous k-point mesh and to stop after creation of the HSE-calculations. Although atomate offers adapters for common queuing systems, OpenCCS, which is employed on the Paderborn supercomputer OCuLUS, is not supported. Therefore, it was easier to split the calculations. The PBE-part was handled on a normal PC. Afterwards, the results were collected and the HSE-calculations were executed on OCuLUS. This collection of results was achieved with some bash-scripting. At the end, the calculations were evaluated by using a python script, which is calling the above mentioned routine. Overall, this workflow is not completely automated, as it would require that all steps and even the saving of the results into a database are handled by the PC without human intervention. Nevertheless, our implementation saves a lot of time compared to a traditional workflow, where each step is realized manually. With this approach, hundreds of calculations can easily be handled by it.

As can be seen in Eq. 3.28, there is a freedom regarding the number of valence and conduction bands, which are used in the calculation of the branch point energy. For diamond and zinc-blende phases, it was recommended by Hinuma *et al.* to use $N_{VB} = 2$ and $N_{CB} = 1$.[99] We decided to use these values as a default. As a small test, we compared our results with Deàk *et al.*[95] They calculated the band alignment for TiO_2 in two structures: rutile and anatase. As can be seen in Tab. 3.2, we achieved reasonable agreement, especially when we consider the fact that our implementation of the branch point calculation is designed for screening applications.

Table 3.2: Comparsion of band alignment results for two structures of TiO_2: anatase and rutile. The table lists our results for the band gap, the shift of the valence band maximum and the shift of the conduction band minimum. Next to them, the results from the study of Deàk *et al.*[95] are shown.

Modification	Band gap	Deàk[95]	Shift VBM	Deàk[95]	shift CBM	Deàk[95]
Anatase	3.57 eV	3.58 eV	-2.04 eV	-2.00 eV	1.53 eV	1,58 eV
Rutile	3.24 eV	3.37 eV	-1.35 eV	-1.38 eV	1.89 eV	1.99 eV

3.5.3 Band gap validation

For the calculation of the band gap, we are using a homogeneous k-point mesh, which is Γ-centered. This allows us to combine band gap and band alignment screening. However, if we are investigating a material, where the VBM and CBM are not found at the Γ-point, there is no guarantee that we will obtain the correct values for both properties. This will result in an overestimation of the gap. To obtain reliable results also in such cases, the density of the employed mesh can be increased in the atomate workflow by changing the reciprocal density parameter. The default is 50 k-points per atom and we set this value to 100 and 200 to check the convergence. The smallest value appears most reliable, as we are expecting an overestimation if the VBM and CBM are not located directly at a k-point.

In order to obtain a more interesting comparison, I decided to compare our results with the ones from a publication, which appeared after our calculations were done.[100] Interestingly, this comparison indicates that the the loose k-point mesh is performing well. Therefore, I also included some further results for binary thallium halides in order to show the overestimation problem encountered for loose k-point meshes. However, these compounds are not evaluated and are not taken into account for the calculation of the mean average error.

The cited study used structural data from experiment,[100] whereas we employed PBE-optimised structures. This could explain the deviation in HSE-gaps for TiI, $Rb_3Sb_2Br_9$, and $InPS_4$. However, the 0.81 eV deviation for SiP_2 is probably caused by something else, as already the PBE-gaps reported in the Materials Project Database[63] (1.42 eV) and in Ref. 100 (0.8 eV) differ significantly. Nevertheless, looking at these unfavorable cases, we see that our results are in better agreement with the experimental data. This indicates that it is probably better to employ PBE-optimised rather than experimental structures, when these structures differ. For the other compounds, a reasonable agreement is reached.

Compared to experimental data, we observe an overestimation for ternaries and an underestimation for binaries, except for Si_3N_4 and SiP_2. We obtain a mean absolute error of 0.30 eV, which is mainly given by the high deviations for AgI, Si_3N_4, P_3N_5, and SiP_2. Without these outliers, we would reduce our mean absolute deviation to 0.1 eV. The ternaries are performing worse since they have no strongly deviating compounds. The mean absolute error is 0.26 eV and only BiOCl and $Rb_3Sb_2Br_9$ show deviations

Table 3.3: Band gaps for selected compounds. MP-ID is the Materials Project ID; the value after density gives the number of k-points per atom; and the last two columns are values reported in the study by Borlido *et al.*[100] The compounds are grouped starting with binary halides followed by binary pnictides, ternary halides and ternary pnictide. The last group is listing binary thallium halides. Within each group, the compounds are sorted by their computed band gap.

Compound	MP-ID	Density 50	Density 100	Density 200	HSE[100]	Experiment[100]
TlI	mp-571102	3.16 eV	2.81 eV	2,81 eV	2.52 eV	2.92 eV
AgI	mp-22925	2.90 eV	2.52 eV	2.52 eV	2.50 eV	2.91 eV
Si_3N_4	mp-988	5.73 eV	5.72 eV	5.72 eV	5.78 eV	5.10 eV
P_3N_5	mp-567907	4.97 eV	4.99 eV	5.04 eV	5.10 eV	5.87 eV
B_6P	mp-28395	3.23 eV	3.70 eV	3.52 eV	3.15 eV	3.35 eV
GaP	mp-2490	2.36 eV	2.36 eV	2.34 eV	2.30 eV	2.35 eV
AlP	mp-1550	2.33 eV	2.33 eV	2.33 eV	2.28 eV	2.45 eV
SiP_2	mp-9996	2.25 eV	2.24 eV	2.20 eV	1.39 eV	1.89 eV
BP	mp-1479	2.02 eV	1.98 eV	1.98 eV	2.02 eV	2.10 eV
BiOCl	mp-22939	3.60 eV	3.68 eV	3.61 eV	3.64 eV	3.46 eV
$Rb_3Sb_2Br_9$	mp-2490	2.52 eV	2.52 eV	2.52 eV	2.35 eV	2.48 eV
SbSI	mp-23041	2.37 eV	2.35 eV	2.34 eV	2.28 eV	1.88 eV
BiOI	mp-22987	2.28 eV	2.27 eV	2.28 eV	2.40 eV	1.89 eV
$InPS_4$	mp-20790	3.41 eV	3.52 eV	3.40 eV	3.59 eV	3.12 eV
TlCl	mp-569639	3.86 eV	3.60 eV	3.31 eV		
TlBr	mp-568560	3.49 eV	3.01 eV	3.01 eV		
TlI	mp-571102	3.16 eV	2.81 eV	2.81 eV		

smaller than 0.2 eV. Nonetheless, our results seem fine when comparing them with the ones of Borlido *et al.*, who estimated a mean absolute deviation of 0.53 eV for all examined compounds.[100] Overall, we can conclude that the performance of HSE is not sufficient for a reliable and exact estimation of band gaps, but it should be good enough for our screening. For further investigations, the size of the errors should be kept in mind, so that more sophisticated approaches might be used to improve the estimate of the band gap. Such an approach was recently implemented into atomate, which uses a PBE calculation in order to identify the CBM and VBM. The HSE-calculation is then just run for these two points.[72]

3.5.4 Branch point for predicting p- or n-type behavior

The branch point concept might also be employed to predict n- or p-type behavior of a material. For this purpose, the position of the branch point is compared to the positions of valence and conduction band. If the branch point energy is close to the valence band,

p-type behavior is expected and when it is close to the conduction band, n-type behavior is assumed. If none of these two cases is fulfilled, the compounds are expected to be ambipolar.[97,98] Based on this hypothesis, we have investigated halides and pnictides. The details and results are reported in the sections on halides (section 4.3) and pnictides (section 4.4).

3.6 Defect chemistry

Some of the main questions for the search of a transparent **p-type** semiconductor will be discussed in this chapter: Is a material intrinsically p-type or can it be doped to become a p-type semiconductor and if so how can this be achieved? On the one hand, these questions can be investigated by analyzing the defects of the materials. On the other, some groups try to avoid such computationally demanding analysis by either employing the branch point concept[97,98] or a hydrogen descriptor[101] to address the question of p-type dopability. However, the predictive power of these two approaches is under discussion.[64] Furthermore, we should also keep in mind that the hydrogen descriptor was developed and tested for oxides only[101] and that Woods-Robinson *et. al*[86] assessed the branch point concept on some known p-type and n-type materials. They reached the conclusion that defect calculations still need to be employed in order to correctly determine p-type dopability. Also, these two concepts cannot be used to identify possible p-dopants.

As of now, there is no way around the bottleneck of defect calculations. About 50 calculations are necessary for binaries and some hundreds for ternaries in order to calculate point defect formation energies. This is in contrast to the single calculations required for the other properties. The other factor rendering the computation of defect formation energies expensive is the use of supercells containing up to some hundred atoms to minimize interactions between periodic images. Therefore, we decided to employ PYCDT,[75] which is handling the defect calculations on the GGA-level of theory *via* the PBE functional.[56] We chose the supercells in such a way that they are larger than 10 $\AA$ in each direction. This results in cells with 60 to 250 atoms.

3.6.1 Computation of point defects

The optimized structures from the branch point workflow are used in PyCDT[75] to calculate the formation energy for neutral and charged defects in the selected semiconductors. The formation energy is calculated as:

$$\Delta E^f[X^q] = E_{tot}[X^q] - E_{tot}[bulk] - \sum_i n_i \mu_i + qE_F + E^q_{corr}, \tag{3.29}$$

where $E_{tot}[bulk]$ is the total energy of the bulk cell, which is subtracted from the total energy of the defect cell $E_{tot}[X^q]$. The next term takes the difference in energy between atomic species in the bulk and defect cell into account: $n_i = 1$ for adding one atom of species i and $n_i = -1$ for removing an atom of species i. This energy is dependent on

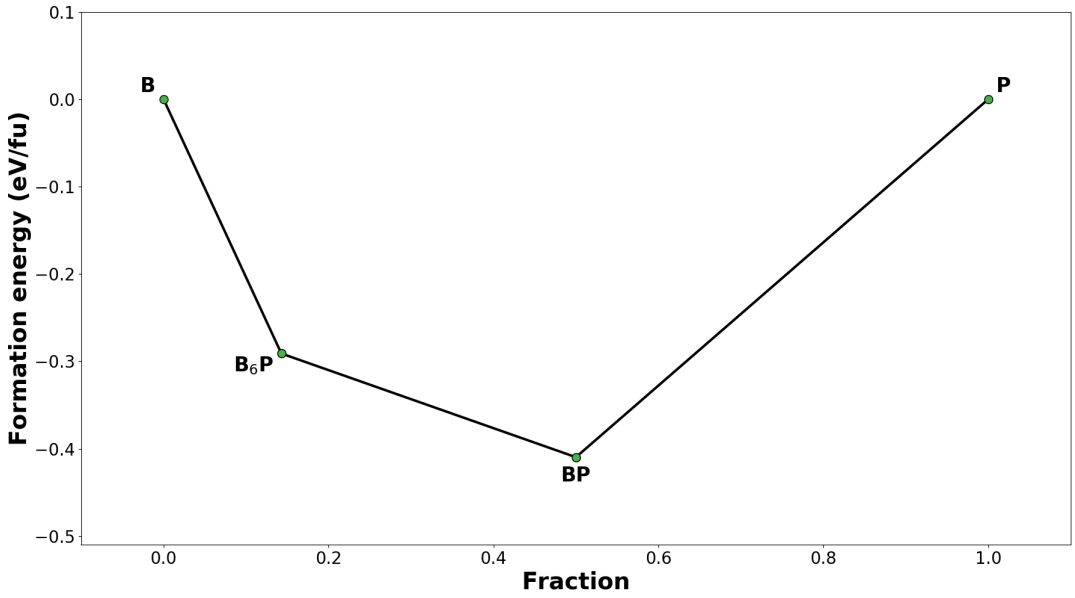

Figure 3.5: Phase diagram of BP showing two possible conditions under which it can be synthesized: cation-rich (B_6P) and anion-rich (P). Phase diagram was created by and with data from MPDB.[63]

the chemical potential μ_i of the species. For charged systems, *i.e.* $q \neq 0$, we also have to consider the cost of removing or adding electrons. This is achieved by considering the Fermi energy E_F. Finally, a second correction for charged systems, E^q_{corr}, is required owing to the periodicity of the cell. For this term either the definition by Freysoldt[102] for isotropic systems or by Kumagai[103] for anisotropic systems can be employed. Further details on these corrections can be found in Ref. 75.

In PyCDT, the individual chemical potentials are determined *via* the grand-canonical ensemble approach,*i.e.* bounds on the chemical potentials are set from zero-temperature energies.[75,104] The phase diagram is constructed from data found in the MPDB.[63] For binaries, this procedure is intuitive. In case of BP, we can look at the cation-rich limit B_6P, or at the anion-rich limit P, see Fig. 3.5. For ternaries, the number of regions is depending on the neighboring points in the phase diagram. For the example of Ca_2PN_3 with nine neighboring phases, there are 9 planes in the phase diagram translating into nine possible regions, see Fig. 3.6.

Vacancies of anions are a common cause to prevent hole doping. By varying the Fermi energy, these defects can exhibit negative formation energies before reaching the valence band. This will lead to the release of electrons into the system during the attempt to dope the material p-type. Therefore, we define a hole killing defect as a defect, for which the formation energy reaches a negative value before the Fermi energy is shifted beyond the valence band. The creation of anion vacancies can be hindered by creating compounds under anion-rich conditions. Therefore, these regions are promising, as one would expect the highest chances for finding hole dopability in these regions. In fact,

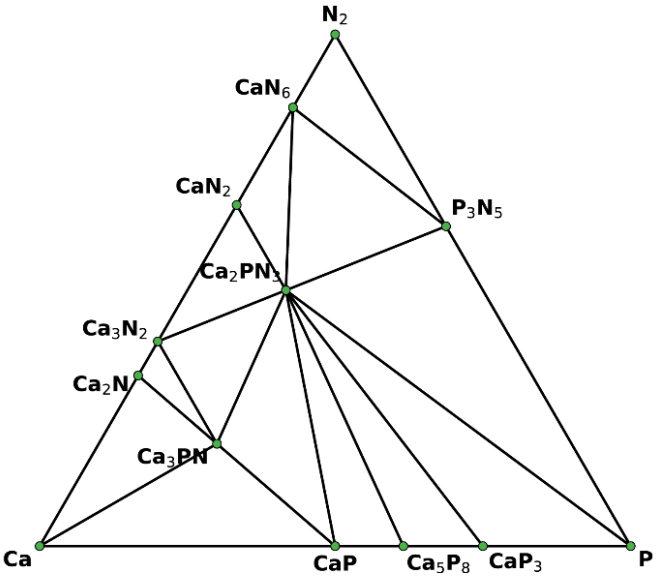

Figure 3.6: Phase diagram of Ca_2PN_3 showing nine possible regions. Phase diagram was created by and with data from MPDB.[63]

we can categorize most of our binaries and ternaries, which pass the intrinsic defect screening, in two classes: no hole killing defects under-anion rich conditions and no hole killing defects under both anion- and cation-rich conditions. So it is quite rare for a material to pass the intrinsic screening only under cation-rich conditions.

In order to identify a suitable dopant, we need to find an extrinsic substituent resulting in a shallow acceptor defect. Therefore, the charge transition from -1 to 0 should be near the valence band. The distance between the charge transition and the valence band is the activation energy, which is of importance for the calculation of the carrier concentration. On the GGA level of theory, the activation energy might be too inaccurate.[105] Owing to this, we just try to judge if we are dealing with a shallow or deep acceptor defect. As a further requirement, the formation energy of the shallow acceptor defect should also not be crossed by a donor defect. This would result in Fermi pinning and limit the dopability for that dopant and material. In some cases, a cation vacancy is already fulfilling these requirements, so that we can label that material p-type after the intrinsic screening. We call such a material intrinsic p-type. Nevertheless, we also perform the dopant screening for these materials. If the material is also passing this step, one last screening step remains: we have to make sure that the dopant is not causing self-compensation. For this, we have to check if interstitials and possible n-type substitutions of that dopant are either Fermi pinning the dopant or even hole killing. In the case of BP with silicon as p-dopant on phoshphorus, we have to consider silicon substitution on boron and silicon interstitials. Therefore, the defect screening is composed of three steps: intrinsic screening, dopant screening and screening for self-compensation. In general, extrinsic screening refers to the latter two steps.

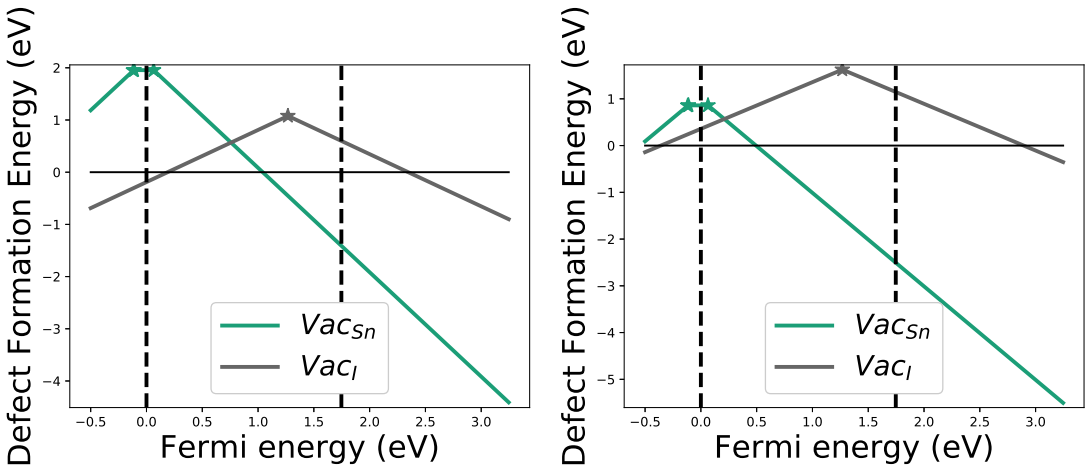

Figure 3.7: Defect chemistry of SnI_2 showing cation and anion vacancies under cation- (left) and anion-rich (right) conditions. The dashed lines represent the valence band maxima and conduction band minima. The vacancy of tin is a shallow acceptor defect illustrating the characteristics of a good p-dopant. In contrast to this, the vacancy of iodine is hole killing under cation-rich conditions, because its formation energy is becoming negative before reaching the valence band maximum leading to its spontaneous formation after the crossing point. Furthermore, Fermi pinning is observed under anion-rich conditions for this vacancy. This means that the Fermi energy is pinned at the point where the formation energies of both vacancies cross each other. Trying to go beyond that point to further shift the Fermi-level results in compensation. Owing to this, the tin vacancy would fail in our screening.

4 Results of the high-throughput screening

4.1 Binary screening

We used mainly binary compounds based on nitrogen and phoshpor (pnictides) or chlorine, bromine and iodine (halides) for validation, since the properties of binaries are better known than the ones of ternaries. Owing to this, we decided to provide an overview of some binaries in this section. This section has some overlap with the halide (section 4.3) and the pnictide (section 4.4) studies. However, not all of the compounds are discussed in full detail in this section, in order to minimize this overlap. For the study here, we employed a loose k-point mesh of 50 k-points per atom, which means that some of the gaps might be overestimated, see section 3.5. We screened the intrinsic defects In order to identify some trends in defect chemistry, but decided against dopant screening. In addition, we compare the different screening criteria that we employed by utilizing a color code. Lastly, we tried to further improve some of the more promising binaries by adding a third element to their formula.

4.1.1 Data description

Replacing an element by another element with lower electronegativity and assuming that the symmetry is not changed, we expect a decrease of both the effective mass and the optical band gap for this compound. The thallium salts TlX with X = Cl, Br or I exhibit exactly this behavior. Thalium(I)chloride has a HSE-band gap of 3.86 eV and a harmonic average for the hole effective mass of 0.57 m_e. By keeping the symmetry and changing chloride with bromide and iodide the HSE-band gap decreases to 3.47 and 3.16 m_e. In case of the hole effective mass, it reduces to 0.51 and 0.48 m_e for Thalium(I)bromide and Thalium(I)iodide, respectively.

For the copper salts CuX with X = Cl, Br or I, the harmonic average of the hole effective mass is behaving as expected, going down from 1.78 (CuCl) to 1.30 (CuBr) and 0.86 m_e (CuI). Interestingly, this is not true for the experimentally measured band gap, which decreases first from 3.4 (CuCl) to 3.07 eV (CuBr), but then rises to 3.12 eV (CuI).[106] The values for copper(I)bromide and copper(I)iodide are pretty close, so that the wrong trend could also arise from experimental uncertainties. The HSE-band gaps for copper halides of 2.37 eV (CuCl), 2.18 eV (CuBr), and 2.54 eV (CuI) do not compare well with the experimental band gaps. This seems to be a specific problem of the HSE functional, since also for HSE06 similar values are reported and better agreement is obtained with other hybrid functionals in Ref. 100. Interestingly, also most of the functionals in that reference show a higher gap for CuI than for CuCl. The neglect of spin orbit coupling could be one of the factors causing this discrepancy. For gold(I)bromide

and gold(I)iodide this behavior is even more pronounced: The HSE-gap rises from 2.76 (AuBr) to 3.08 eV (AuI). It should be kept in mind that relativistic effects are not considered in the calculations and the HSE-band gaps might therefore be quite approximate. Although gold(I)chloride exhibits a different symmetry than gold(I)bromide, the band gap is behaving as expected. It goes down from 3.01 to 2.76 eV and the harmonic average of the hole effective mass decreases also from 0.86 to 0.84 m_e.

Tin salts are following the expected trend, but we should note that the symmetry of tin(II)iodide is different from the one of tin(II)chloride and tin(II)bromide. This might explain the huge jump in the two properties. The harmonic average of the hole effective mass is going down from 3.59 ($SnCl_2$) to 2.77 ($SnBr_2$) and 0.88 m_e (SnI_2). The HSE-band gap decreases from 3.98 ($SnCl_2$) to 3.34 ($SnBr_2$) and 2.41 eV (SnI_2). The symmetries of the bismuth salts BiX_3 with X = Cl, Br or I are all different, so it is not surprising that these compounds do not follow the trend for the harmonic average of the hole effective mass stated in the beginning. In fact, $BiCl_3$ exhibits the lowest hole effective mass with 4.18 m_e. In contrast to this, the band gap is exhibiting the expected behavior. The computed HSE-band gaps are going down from 4.44 ($BiCl_3$) to 3.76 ($BiBr_3$) and 3.27 eV (BiI_3). For BiI_3, the HSE06 value of 3.11 eV from Ref. 100 is in agreement with our results, whereas the experimental gap of 1.67 eV[107] is indicating a huge overestimation. The best fit to this value in Ref. 100 is the PBE functional including spin orbit coupling. On the other hand, all hybrid functionals employed in Ref. 100 overestimate this gap by more than 1 eV.

For beryllium and indium, we investigated bromide and iodide salts only. The beryllium salts exhibit the expected trends when going from bromine to iodide, as the HSE-band gap reduces from 6.43 to 5.11 eV and the hole effective mass from 3.73 to 2.89 m_e. Contrary to this, the indium salts show the opposite behavior. The HSE-band gap rises from 2.32 to 2.62 eV and the harmonic average of the hole effective mass increases from 0.32 to 0.39 m_e.

The difference in electronegativity between nitrogen and phosphorus is fairly large. Therefore, we expect larger differences for the band gaps and the hole effective masses. The magnesium salts Mg_3N_2 and Mg_3P_2 are good examples. The harmonic average of the hole effective mass drops from 4.70 (Mg_3N_2) to 1.35 m_e (Mg_3P_2) and the experimental band gap reduces from 2.8 (Mg_3N_2,[108] to 1.4 eV (Mg_3P_2).[54] Our calculated HSE-band gaps are resulting in a smaller change due to an underestimation of the Mg_3N_2 (2.59 eV) and an overestimation of the Mg_3P_2 (2.26 eV) band gaps. The PBE calculations are even worse with 1.51 eV for Mg_3N_2 and 1.61 eV for Mg_3P_2 indicating the wrong trend.[63]

Owing to the huge difference in electronegativity, even changes in composition and symmetry do not have much influence on the trend. Going from BP to B_6P both values increase, but they are not reaching the corresponding values of boron nitride BN with a band gap of 5.96 eV and a hole effective mass average of 1.4 m_e. The silicon salts do not even exhibit the same stoichiometric composition, but the HSE-band gaps are still following the trend. Si_3N_4 exhibits the highest band gap with 5.73 eV and SiP_2 the smallest with 2.25 eV. The band gap of SiP (2.52 eV) is close to SiP. Interestingly, the harmonic average of the hole effective mass in Si_3N_4 (1.13 m_e) is smaller than in SiP (2.60 m_e) and SiP_2 (1.53 m_e). The aluminum salts AlN, AlP and AlSb are following the

expected trend. Starting with AlN, the band gap is 6.11 eV and the hole effective mass is 1.03 m_e. For AlP, these values decrease to 2.33 eV and 0.56 m_e. Finally, for AlSb they are 1.69 eV and 0.41 m_e.

Looking at the stability, one can stumble upon B_6P, CuP_2, KP, Li_3P_7, SiP, SiP_2, and TlP_5, which might appear a little bit odd when counting the valence electrons. Based on our screening approach, all of the mentioned compounds should be stable, as they satisfy our stability criterion of 0 eV above the convex hull. Taking into account some inorganic textbook knowledge,[109,110] we realize that B_6P can also be written as $B_{12}P_2$ and boron is known to also form icosahedra, so this compound appears not so unlikely anymore. Similar and by realizing that phosphorus can form various polyanions, the stability of the phosphorus compounds can also be rationalized with exceptions being SiP and KP. For SiP, we can look into the phase diagram.[111] There SiP is found to be stable and SiP_2 is metastable. The energy above convex hull of SiP_2 should therefore not be 0 eV. KP is only stable when it is synthesized in an ampule using stoichiometric amounts of starting materials and inert gas during processing.[83] A detailed discussion on the stability of potassium- and phosphorus-containing compounds is given in section 3.3.

The stability with respect to environmental conditions such as air and moisture, can not be judged by our stability criterion. Therefore, we can not claim that Li_3P_7 should not lie on the convex hull, even though it has to be synthesized under inert conditions.[112] Owing to this, we are not surprised that also some other compounds either react or decompose or are highly soluble in water. Magnesium nitride and magnesium phosphide are known to react in water and the toxicity of the latter is based on the formation of phosphine in the stomach.[109,113] Bismuth chloride and bismuth bromide will also react in water and form BiOCl and BiOBr, respectively.[109] Already these few examples demonstrate that caution has to be exercised when the stability is judged, in particular if the judgment is based on the convex hull criterion, see also section 3.3).

4.1.2 Defect chemistry

In general, we might expect a relation between stability and defect chemistry. However, looking at the defect chemistry of CuP_2 and KP (Fig. 4.1), it can be shown that this does not hold and that care has to be taken, when making assumptions about the stability of a compound based on its defect chemistry. Both materials pass our intrinsic defect screening and the anion vacancy is even making both materials intrinsic p-type. In addition, stability is sometimes also discussed in terms of vacancy formation energy. If a vacancy exhibits negative formation energy the material is considered to be unstable. However, we should also be careful with this reasoning since the copper vacancy forms more easily and one might reach the conclusion that KP is more stable than CuP_2.

As will be discussed in this section, the defect chemistry of both materials is better than the one of most halides. One important factor for the defect chemistry is the anion. Halides form in general a soft lattice, which is prone to defect formation.[124] This also implicates that halide materials are less promising for p-type TCM application. In fact, looking into Tab. 4.1 we see that many of the halides listed there fail the intrinsic defect

Table 4.1: Table of binary candidates sorted alphabetically listing MPDB IDs, symmetries, experimental (E_g^{Exp}) and HSE-band gaps (E_g^{HSE}) as well as harmonic mean hole effective masses ($\overline{m}_h^*$). The color code is explained in subsection 4.1.3. * indicates different symmetries between calculations and experiments.

Material	MPDB ID	Space group	E_g^{Exp} (eV)	E_g^{HSE} (eV)	$\overline{m}_h^*$ (m_e)	intr. defects
AgBr	mp-866291	$F\bar{4}3m$	2.71*[106]	2.50	1.25	p-type
AlN	mp-661	$P6_3mc$	6.11[114]	5.43	1.03	p-type
AlSb	mp-2624	$F\bar{4}3m$	1.69[106]	1.77	0.41	p-type
AuBr	mp-505366	$P4_2/ncm$		2.76	0.84	p-type
AuCl	mp-32780	$I4_1/amd$		3.01	0.86	p-type
AuI	mp-27725	$P4_2/ncm$		3.08	0.70	p-type
$BaBr_2$	mp-27456	Pnma		5.53	2.46	negative
$BaCl_2$	mp-569639	$Fm\bar{3}m$	7.00*[115]	6.71	1.43	p-type
BaP_{10}	mp-28035	$Cmc2_1$		2.00	0.92	p-type
$BeBr_2$	mp-30139	Ibam		6.43	3.73	p-type
BeI_2	mp-570886	Ibam		5.11	2.89	p-type
Be_3N_2	mp-18337	$Ia\bar{3}$		4.56	1.17	negative
$BiBr_3$	mp-752602	$P2_1/c$		3.76	7.77	negative
$BiCl_3$	mp-22908	Pnma		4.44	4.18	negative
BiI_3	mp-22849	$R\bar{3}$	1.67[107]	3.27	5.33	negative
BN	mp-984	$P6_3/mmc$	5.96[116]	5.72	1.40	p-type
BP	mp-1479	$F\bar{4}3m$	2.10[106]	2.02	0.34	p-type
B_6P	mp-28395	$R\bar{3}m$	3.35[117]	3.23	0.84	p-type
CuBr	mp-22913	$F\bar{4}3m$	3.07[106]	2.18	1.30	p-type
CuCl	mp-22914	$F\bar{4}3m$	3.4[106]	2.37	1.78	p-type
CuI	mp-22895	$F\bar{4}3m$	3.12[106]	2.54	0.86	p-type
CuP_2	mp-927	$P2_1$	1.51[118]	1.75	0.54	p-type
GeI_2	mp-27922	$P\bar{3}m1$		2.81	1.48	negative
Ge_3N_4	mp-672289	P31c		3.52	1.52	p-type
InP	mp-20351	$F\bar{4}3m$	1.42[106]	1.24	0.53	p-type
KP	mp-7441	$P2_12_12_1$		1.72	1.03	p-type
Li_3P_7	mp-28336	$P2_12_12_1$		2.51	1.72	p-type
Mg_3N_2	mp-1559	$Ia\bar{3}$	2.8[108]	2.59	4.70	p-type
Mg_3P_2	mp-2514	$Ia\bar{3}$	1.4[54]	2.26	1.35	p-type
P_3N_5	mp-567907	C2/c	5.87[119]	4.97	1.08	p-type
SbI_3	mp-23281	$R\bar{3}$	2.41*[106]	2.81	3.61	negative
Si_3N_4	mp-988	$P6_3/m$	5.10[120]	5.73	1.13	p-type
SiP	mp-2798	$Cmc2_1$		2.52	2.6	p-type
SiP_2	mp-9996	Pbam	1.89[106]	2.25	1.53	negative
$SnBr_2$	mp-29862	Pnma	3.45[121]	3.34	2.77	negative
$SnCl_2$	mp-569152	Pnma	3.80[122]	3.98	3.59	negative
SnI_2	mp-27194	C2/m		2.41	0.88	p-type
TiI_4	mp-541013	C2/c		2.0	1.5	not clear
TlBr	mp-568560	$Fm\bar{3}m$	2.66*[123]	3.49	0.51	p-type
TlCl	mp-569639	$Fm\bar{3}m$	3.23*[106]	3.86	0.57	p-type
TlI	mp-571102	$Fm\bar{3}m$	3.07[106]	3.16	0.48	p-type
TlP_5	mp-27411	$Pmc2_1$		1.99	1.18	p-type
Zn_3N_2	mp-9460	$Ia\bar{3}$		0.77	n. a.	negative

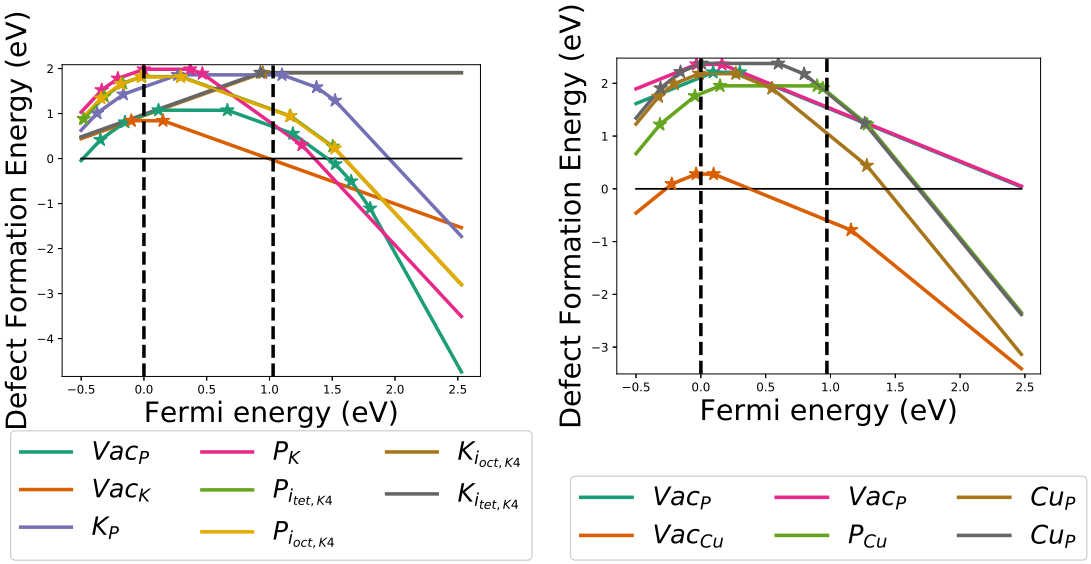

Figure 4.1: Left: Defect chemistry of KP under P-rich conditions, which is experimentally unstable as mentioned in the text. Right: Defect chemistry of CuP_2 under P-rich conditions, a stable material. These two compounds demonstrate that the defect chemistry does not indicate stability.

screening. The tin halides SnX_2 with X = Cl, Br or I are good examples for this, see Fig. 4.2. Their defect chemistry improves when going from chloride to bromide and iodide. Therefore, tin iodide is even passing our intrinsic defect screening.

A similar situation is encountered for bismuth halides BiX_3 with X = Cl, Br or I, where the defect chemistry is also becoming better by going from chloride to bromide and iodide. For these materials, we note a decreasing importance of the anion vacancy, so that holes in bismuth iodide are mainly killed by the formation of a bismuth interstitial defect. The mentioned anion vacancies are normally the hole killing defects, which have to be avoided for p-type TCMs. For this purpose, anion-rich conditions are helpful to prevent the formation of hole killing vacancies. Thalium halides are possible p-type TCMs when grown under anion-rich conditions. The defect formation energies in copper halides are rather high compared to other halides rendering these materials possible p-type TCMs under both anion-rich and -poor conditions. The gold halides are also possible p-type materials under both conditions as they are quite resistant to the release electrons. Only the anion vacancy is showing the potential for releasing electrons, but it is not hole killing since the formation energy of the vacancy stays positive for the positively charged state in the band gap.

The case of barium chloride and barium bromide is quite interesting, since barium chloride is passing and barium bromide is failing the intrinsic defect screening. In both cases, the anion vacancies are problematic, but in $BaCl_2$ this vacancy exhibits a slightly higher formation energy. We suspect symmetry reasons for this behavior: In case of

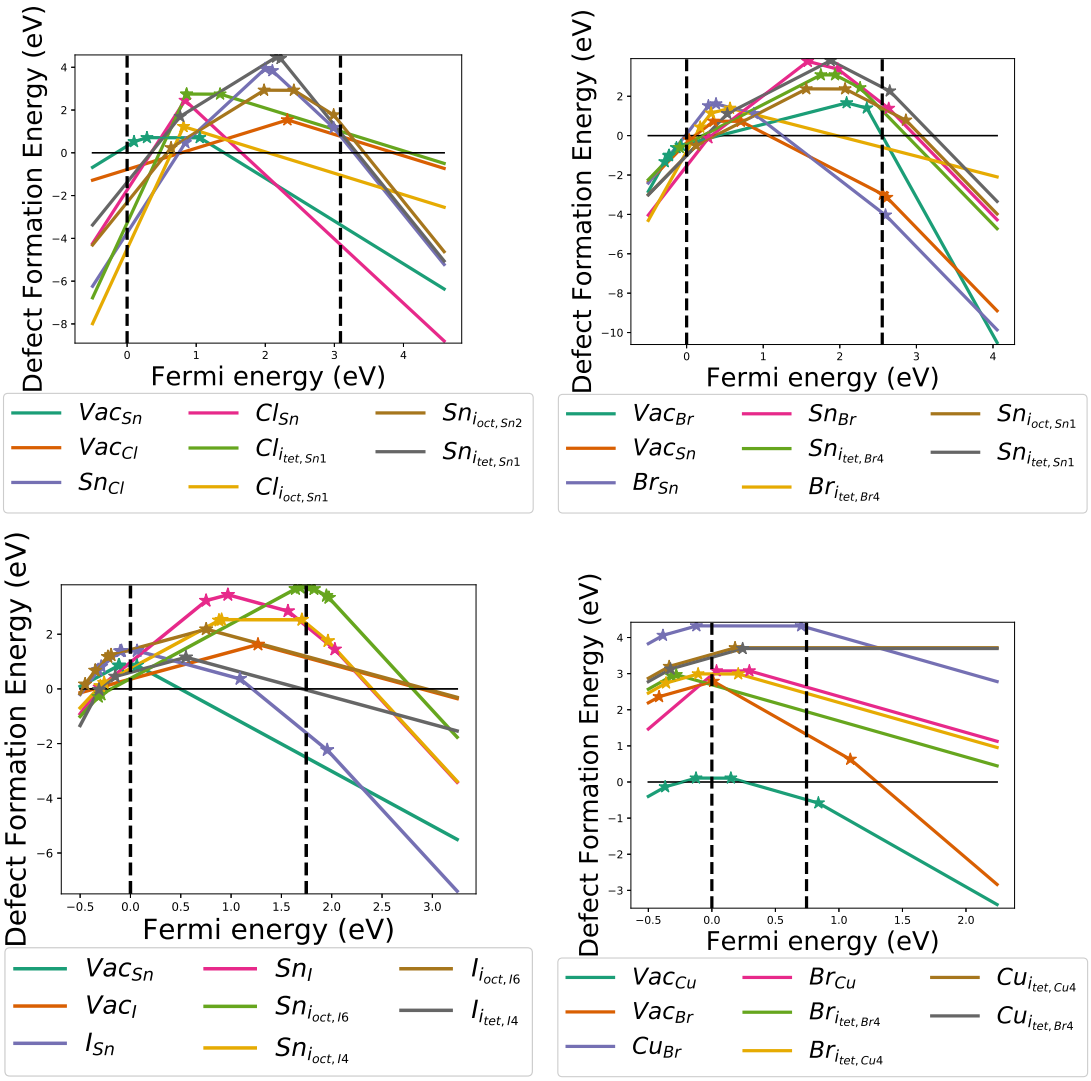

Figure 4.2: Top left: Defect chemistry of $SnCl_2$ under Cl-rich conditions. Top right: Defect chemistry of $SnBr_2$ under Br-rich conditions. Bottom left: Defect chemistry of SnI_2 under I-rich conditions. The tin halides show the improving intrinsic defect chemistry, when going from tin chloride to tin bromide and tin iodine. Bottom Right: Defect chemistry of CuBr under Br-rich conditions showing the high defect formation energies of donor defects and the low formation energy of the acceptor defect (copper vacancy).

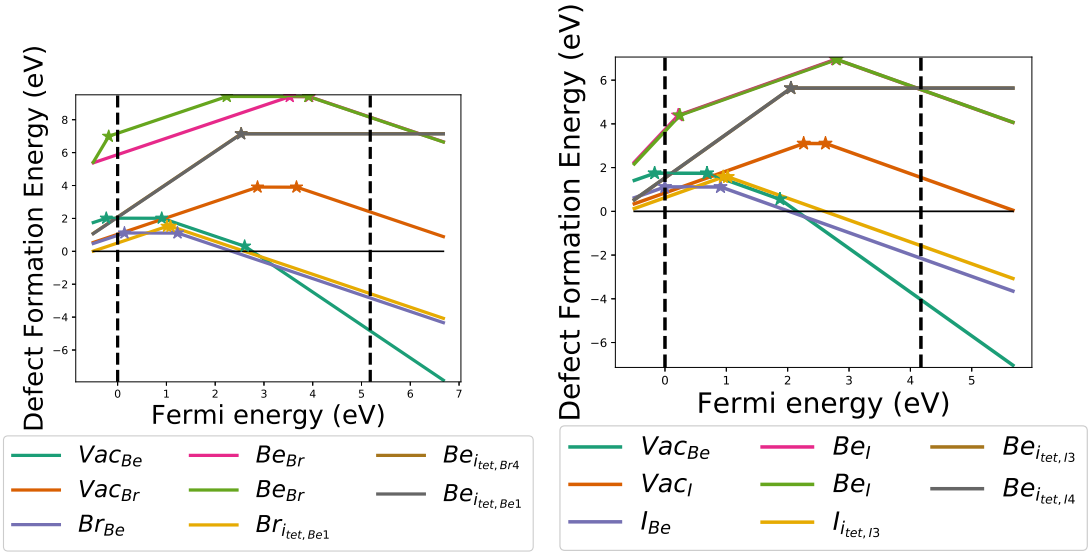

Figure 4.3: Left: Defect chemistry of $BeBr_2$ under Br-rich conditions. Right: Defect chemistry of BeI_2 under I-rich conditions. We observe similar defect chemistry for both materials.

$BaCl_2$, we used the $Fm\bar{3}m$ space group and fluorite structure, but for $BaBr_2$ the Pnma space group with cotunnite structure was employed. In the fluorite structure, chloride is surrounded by eight barium atoms with a distance of 3.21 $\mathring{A}$, whereas it is surrounded by nine barium atoms with distances ranging from 3.12 to 3.71 $\mathring{A}$ in the cotunnite structure. Unfortunately, the fluoride structure of $BaBr_2$ is not available in the Materials Project Database. On the other hand, for $BaCl_2$ in cotunnite structure, we would expect a failure in the intrinsic defect screening.

Beryllium bromide and beryllium iodide are barely passing the intrinsic defect screening. Their anion vacancies are under control when synthesized under anion-rich conditions. However, under these conditions, the anion interstitial is becoming problematic for both materials, see Fig. 4.3. We note a small improvement when going from beryllium bromide to beryllium iodide. Therefore, beryllium chloride could fail the intrinsic defect screening.

Regarding silver-containing compounds, we just investigated silver bromide, which is passing our intrinsic defect screening, see Fig. 4.4. Interestingly, it is passing in both regions rendering this material quite promising in terms of defect chemistry. Although the branch point of silver-containing compounds is often indicating the opposite, the conduction band minimum is only shifted by about 0.32 eV or 12.6 % from the branch point. Using the classification of Sarmadian *et al.*[98] we would classify this material as n-type with no chance for it being p-type. Finding a suitable dopant could be difficult, since we can not substitute silver, which is already in oxidation state I. Therefore, we would require a dopant with oxidation state 0. This leaves the substitution of bromide and the possibility to use it as an intrinsic p-type semiconductor, if it was stable, but

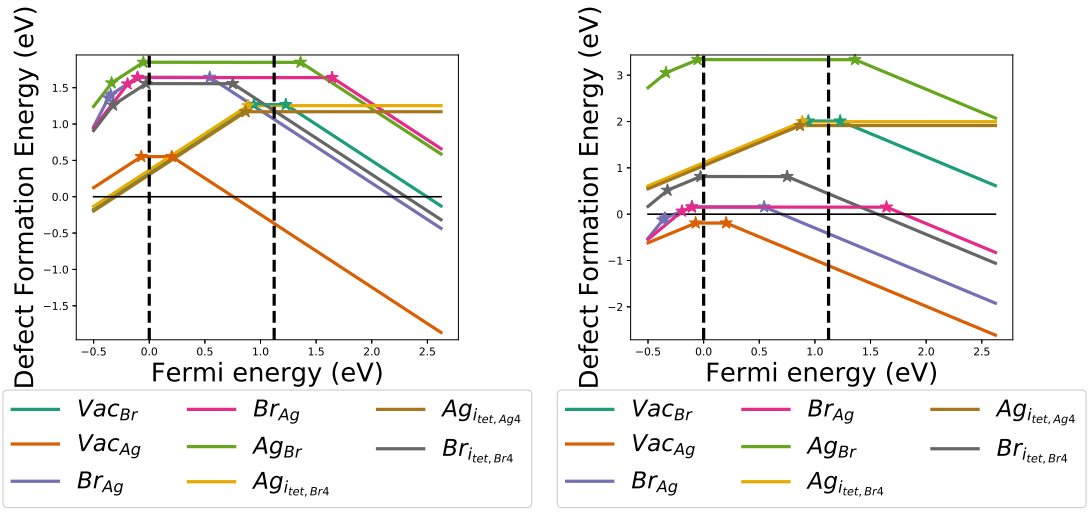

Figure 4.4: Left: Defect chemistry of AgBr under Ag-rich conditions. Right: Defect chemistry of AgBr under Br-rich conditions. Silver bromide is passing the intrinsic defect chemistry screening under both conditions, even though the Br-rich conditions are more promising due to the higher formation energies of Br-vacancy and Ag-interstitials.

silver bromide is known for its photosensitivity.[125]

In case of iodine, we additionally screened germanium(II)iodide, antimony triiodide and titanium tetraiodide without investigating the chloride or bromide counterparts. For GeI_2, it turns out that the vacancy of iodine is not so important and instead interstitial defects of germanium and iodine are killing the electrons under both conditions. Therefore, this material fails our intrinsic defect screening. We encounter a similar situation for SbI_3, where also the intrinsic defects are the major hole killing defects making this compound also fail our intrinsic defect screening. For TiI_4, the intrinsic defects are not that problematic. However, this material fails our intrinsic defect screening under cation-rich conditions because of the iodine vacancy. Under anion-rich conditions, this material turns out to be a borderline case between passing or failing the screening, see Fig. 4.5. Independent of that, the dopant search is expected to be difficult.

Defects in nitrogen-containing materials exhibit often high formation energies. This behavior is especially pronounced in BN, for which we investigated the hexagonal phase. We are not surprised that many of these materials are passing our intrinsic defect screening. Therefore, the compounds failing our screening become more interesting, which are beryllium and zinc nitride. Be_3N_2 is suffering from an interstitial defect of beryllium, which is rendering this material, similar to TiI_4 and its iodine interstitial, a borderline case under anion-rich conditions, see Fig. 4.5. The elemental chemical potential for Zn_3N_2 under anion- and cation-rich conditions are barely changing, see Fig. 4.6. Therefore, it is not enough to employ N-rich conditions in order to get rid of the N-vacancy, which is hole killing under both conditions. Except for Zn_3N_2, the defect chemistry for

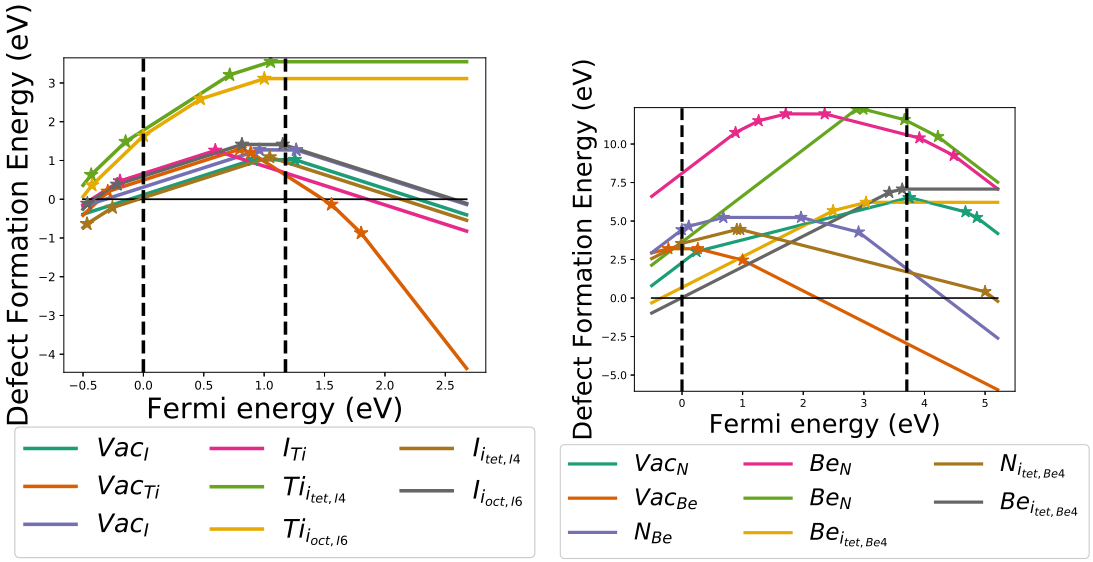

Figure 4.5: Left: Defect chemistry of TiI_4 under I-rich conditions. Right: Defect chemistry of Be_3N_2 under N-rich conditions. In both cases, an interstitial defect (iodine for TiI_4 and beryllium for Be_3N_2) is rendering them borderline cases.

the nitrides will be discussed in the section 4.4 on pnictides.

The behavior of phosphorus-containing materials is quite interesting. Similar to Zn_3N_2 the influence of the chemical potential is minimal in BaP_{10}, CuP_2 and KP and cation-rich as well as P-rich conditions are resulting in nearly the same figures. All of these materials pass our intrinsic screening criteria, so suitable dopants have to be found. Since we can employ both conditions, we could also consider to dope them with silicon in position of phosphorus. In the section on pnictides, we will discuss that this strategy is quite effective. Owing to this, a closer look at silicon phosphide SiP is interesting, see Fig. 4.7. We observe that in that compound the reverse substitution or antisite defect of phosphorus in position of silicon is the main obstacle for achieving p-type dopability. Therefore, we have employed silicon-rich conditions to overcome this. Beside for SiP, cation-rich conditions are also more favorable for BP and B_6P. BP is also passing under P-rich conditions, so that p-dopants for boron can be tried as well as p-dopants for phosphorus under B-rich conditions. B_6P is only barely passing our screening criteria under phosphorus-rich conditions, so attempts to dope it on the boron site are less promising.

Although the formula TlP_5 is looking weird, the defect chemistry appears very promising, see Fig. 4.7. Under both conditions, the defects have quite high formation energies. The defect chemistry of InP is also convincing: this compound is also passing under both conditions, but P-rich conditions are more promising due to the higher formation energy of the phosphorus vacancy. Mg_3P_2 struggles with interstitial defects, especially the magnesium interstitial defect is problematic enforcing Mg-poor/P-rich conditions.

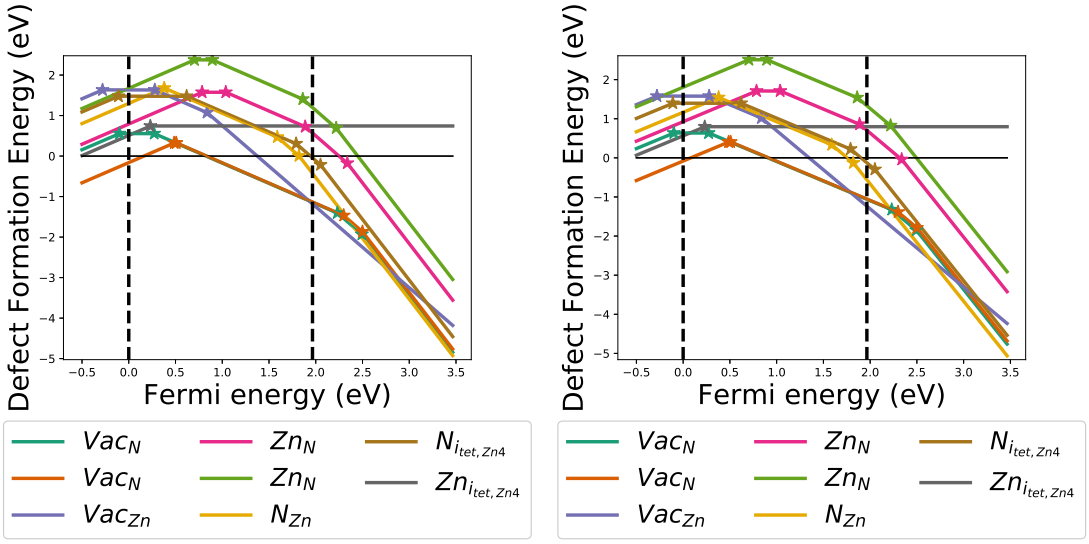

Figure 4.6: Left: Defect chemistry of Zn_3N_2 under Zn-rich conditions. Right: Defect chemistry of Zn_3N_2 under N-rich conditions. Both show nearly the same intrinsic defect chemistry due to the small variation in chemical potential.

Under these conditions, both interstitials are equally detrimental, but not hole killing. Li_3P_7 is barely passing our intrinsic defect screening under P-rich conditions. In particular, the lithium interstitial defect should be avoided enforcing Li-poor/P-rich conditions.

4.1.3 Overview of screening criteria

The screening criteria for the HSE-band gap and the effective mass were adapted for the different studies. The chalcogenides were screened requiring the effective mass to be less than or equal to $1\,m_e$. Furthermore, the band gap had to be larger than 1.70 eV in case of binaries and for ternaries this value had to be between 3.00 and 4.30 eV. For the investigations of pnictides and halides, we relaxed the effective mass criterion to less than $1.50\,m_e$, kept the lower limit of 3.0 eV for the HSE-band gap, but did not apply any upper limit for this quantity. In Tab. 4.1, compounds violating these criteria are either given in red or orange. The latter color is chosen for HSE-band gaps between 1.70 and 3.00 eV and for effective masses between 1.00 and $1.50\,m_e$. Additionally, HSE-band gaps larger than 4.30 eV are shown in blue, since such materials could also be insulating owing to their large band gap.

Based on this color coding, it can be directly seen that just a few substances survive the screening with such criteria. Especially phosphides are struggling with the band gap criterion, so that only B_6P fulfills it. AlN, $BaCl_2$, $BeBr_2$, BeI_2, BN, $BaCl_2$ and Si_3N_4 exhibit large HSE-band gaps. Therefore, it needs to be tested if these materials are still semiconductors. The effective mass poses a challenge for halides and some of them even have effective masses larger than $3.0\,m_e$ indicating bad hole conduction.

Table 4.2: List of derived ternaries. The binary compounds written in **bold** are the starting points, for which we tried to find a better material by adding a third element to compensate the shortcomings of the binary. The binary compounds are ordered following the discussion in the last section. For each binary, the proposed ternary compounds are sorted by their HSE-band gaps. For each material, its MPDB ID, symmetry, HSE-band gap (E_g^{HSE}), eigenvalues of the hole effective mass and harmonic mean hole effective mass ($\overline{m}_h^*$) in m_e and relative shift of the CBM are given. The calculations were performed with a density of 50 k-points per reciprocal atom.

Material	MPDB ID	Space group	E_g^{HSE} (eV)	m_h^*1	m_h^*2	m_h^*3	$\overline{m}_h^*$	shift CBM
AlSb	mp-2624	F$\bar{4}$3m	1.77	0.41	0.41	0.41	0.41	73.3%
$AlSbO_4$	mp-676861	Cmmm	3.37	1.02	1.59	1.82	1.39	26.6%
KMgSb	mp-7089	P4/nmm	1.83	0.44	0.44	77.1	0.66	46.4%
TiCoSb	mp-5967	F$\bar{4}$3m	1.39	1.22	1.22	1.22	1.22	52.5%
h−BN	mp-984	$P6_3/mmc$	5.72	0.96	0.96	18.5	1.40	53.5%
c−BN	mp-1639	F$\bar{4}$3m	5.78	0.62	0.62	0.62	0.62	47.6%
Li_3BN_2	mp-8926	$P4_2/mnm$	4.73	1.03	1.03	188	1.54	44.5%
$PrBN_2$	mp-9028	R$\bar{3}$c	3.17	0.95	0.95	1.82	1.13	44.5%
MgB_9N	mp-30091	R$\bar{3}$m	2.37	0.56	1.37	1.37	0.92	45.4%
BP	mp-1479	F$\bar{4}$3m	2.02	0.34	0.34	0.34	0.34	85.4%
Na_3BP_2	mp-29370	$P2_1/c$	2.62	0.86	1.57	3.84	1.45	49.6%
CuBr	mp-22913	F$\bar{4}$3m	2.18	1.33	1.33	1.33	1.33	5.7%
$CuSe_2Br$	mp-29567	$P2_1/c$	0.90	0.82	1.32	17.0	1.45	43.1%
CuP_2	mp-927	$P2_1/c$	1.75	0.37	0.51	1.12	0.54	50.3%
Cu_4SiP_8	mp-28995	$I4_1/a$	2.29	0.95	1.05	1.05	1.01	57.0%
AgBr	mp-866291	F$\bar{4}$3m	2.50	1.25	1.25	1.25	1.25	12.7%
$CsAgBr_2$	mp-23454	Cmcm	3.52	0.46	3.43	31.5	1.21	32.6%
$AgPbBr_5$	mp-621612	C2/2	3.07	0.66	0.79	122	1.07	53.9%
$CsAgBr_2$	mp-571100	P4/nmm	3.07	0.73	0.73	5972	1.10	31.4%

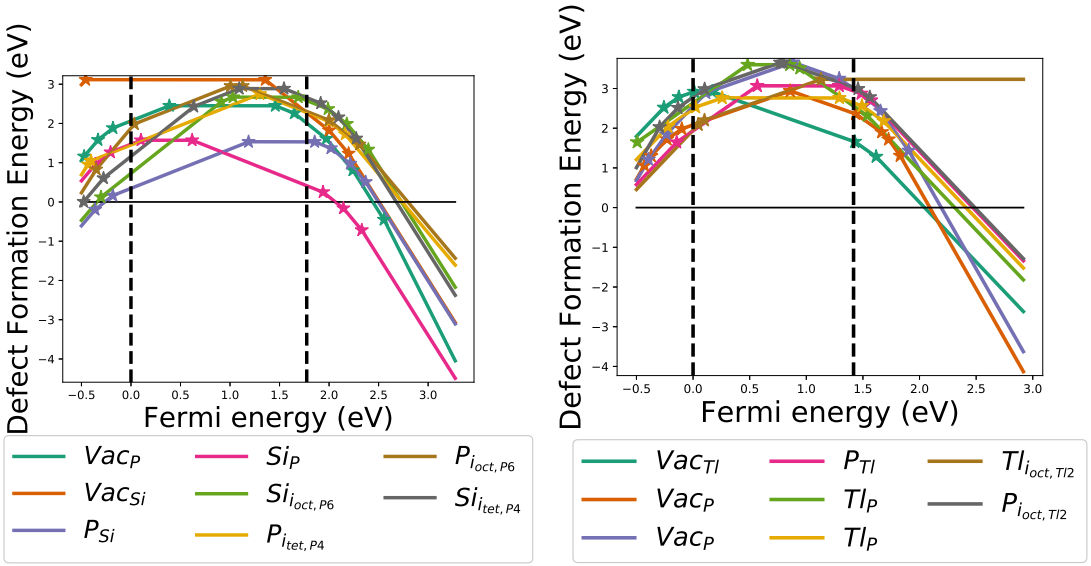

Figure 4.7: Left: Defect chemistry of SiP under Si-rich conditions. The antisite defect of phosphorus in position of silicon is the most troublesome and forcing the employment of Si-rich conditions. Right: Defect chemistry of TlP_5 under P-rich conditions. All defects show high formation energies making this material very promising in terms of p-type as well as n-type doping.

4.1.4 Ternary compounds as a means to improve binaries?

As discussed in the previous section, most of the screened binaries have some drawbacks. Nonetheless, we will take a closer look at some of the more promising materials in this section owing to their favorable defect chemistry and try to rationally improve their properties *via* the introduction of a third element, see Tab. 4.2 for an overview of the ternary compounds derived from this strategy.

We start with AlSb, which was not discussed in detail since it is neither a halide nor a pnictide, see Fig. 4.8. It is p-dopable under both conditions. Its major drawback is the band gap of 1.69 eV, which is too small, even though it is already quite remarkable that an alloy exhibits such a large band gap. Therefore, we need to look for a third element, which is able to widen the band gap. Anions are logical choice for this purpose and in fact the HSE-band gap of $AlSbO_4$ is 3.37 eV. However, when introducing oxygen to the mix we have to be aware that this might lead to the typical disadvantages of oxygen-containing compounds. For example, the harmonic average of the hole effective mass is already worsening by increasing from 0.41 to 1.39 m_e. Based on the branch point concept, we could also face troubles with the defect chemistry. The relative shift of the CBM is only 26.6 %, so this material should still be ambipolar, but below 25 % we would file it under n-type material.

This observation leads us to the question if there are other alloys, which are transparent? Therefore, we further looked into antimony alloys and found TiCoSb as well

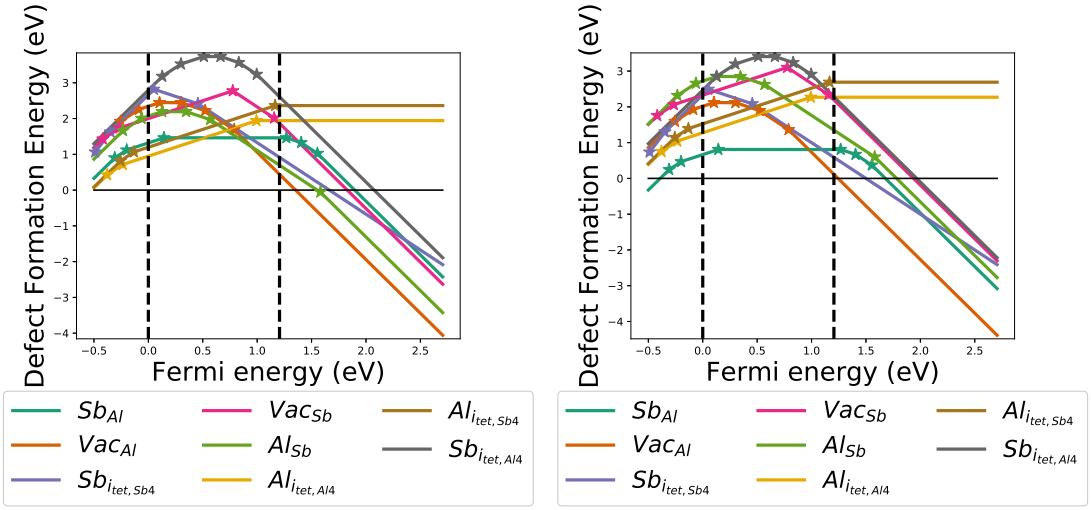

Figure 4.8: Left: Defect chemistry of AlSb under Al-rich conditions. Right: Defect chemistry of AlSb under Sb-rich conditions. Al-rich conditions are more promising than Sb-rich conditions, because of the antisite defect antimony on aluminum.

as KMgSb to be promising. The harmonic average of the hole effective masses is 1.22 for TiCoSb and 0.66 m_e for KMgSb. However, they fail with respect to the required transparency, as their HSE-band gaps of 1.39 (TiCoSb) and 1.83 eV (KMgSb) are too small.

As will be discussed in the pnictide subsection 4.4, BN is passing our intrinsic defect screening for both regions. It crystallyzes into three modifications α- β- and $\gamma-$BN also known as hexagonal (h$-$BN), cubic (c$-$BN) and wurtzite (w$-$BN) boron nitride.[126] For this study we also looked into cubic boron nitride. The major drawback of the hexagonal form is the large band gap of 5.72 eV (HSE). The harmonic average of the effective mass is also not very promising. The band gap is similar for the cubic form. But the effective mass is indicating a better hole conduction for the cubic form. For the ternaries we searched for a second metal in order to improve both properties of hexagonal boron nitride. We found lithium, magnesium and praseodymium to form interesting compounds in combination with BN. The harmonic average of the hole effective masses is ranging from 0.92 (MgB_9N) to 1.13 ($PrBN_2$) and 1.54 m_e (Li_3BN_2). So it is improved for two of the three materials and the exception is the lithium compound. We also observe that the HSE-band gap becomes smaller than 5.72 eV. In the case of MgB_9N, the HSE-band gap of 2.37 eV is even already too small, so that we cannot guarantee transparency anymore. On the other hand, the HSE-band gap of 4.73 eV for Li_3BN_2 is still quite large, so that it has to be checked, if this material is not an insulator. Despite that, the material was already investigated for its ion conductivity.[127] We have to be careful with the HSE-band gap 3.17 eV for $PrBN_2$. This value could exhibit large uncertainties, as relativistic effects were neglected. Apart from this methodological aspect, $PrBN_2$

seems promising, since its band gap fits quite well to our requirements and it exhibits a low effective mass. For all three compounds, the relative shift of the CBM is around 45 %. Therefore, these materials belong to the ambipolar category of the branch point classification scheme and the possibility of p-type dopability is given.

The other promising boron-containing material is BP, which is also passing our intrinsic defect screening under both conditions. This time, we are facing a band gap of 2.10 eV, which is too small for transparency. The harmonic average of the effective mass is remarkably small with a value of 0.34 m_e. Compared to B_6P, see Tab. 4.1, Na_3BP_2 is clearly the less promising candidate. Its HSE-band gap of 2.62 eV is not large enough to ensure transparency and the hole effective mass of 1.45 m_e is quite close to 1.5 m_e. Only the relative shift of the CBM 49.6 % seems to be fine.

Copper halides and copper phosphides turned out to be p-dopable under both conditions. Therefore, we looked into $CuSe_2Br$ and Cu_4SiP_8 in order to check if we can improve the harmonic average of the hole effective mass of CuBr and the band gap of CuP_2. However, the HSE-band gap of Cu_4SiP_8 is 2.05 eV, so the increase in the size of the band gap is not enough for transparency. Furthermore, the effective mass of $CuSe_2Br$ is 1.47 m_e indicating worser p-conductivity than CuBr. In addition, a HSE-band gap of 0.9 eV is rendering this compound even less attractive. For Cu_4SiP_8, the harmonic average of the effective mass is also worsening with 1.01 m_e, but it is still acceptable. So our approach did not work out in this case.

At last let us look into AgBr, which is also passing the intrinsic defect screening under both conditions, but suffering from a big stability issue: the photoreaction to silver and bromine. We looked into $CsAgBr_2$ and $AgPb_2Br_5$, but did not investigate if these compounds still react under light. For $CsAgBr_2$, we found 2 polymorphs, which appear to be promising. The polymorph with Cmcm symmetry exhibits a HSE- band gap of 3.52 eV and a harmonic average of the hole effective mass of 1.21 m_e. The other one crystallized in P4/nmm symmetry, has a HSE-band gap of 3.07 eV and an effective mass of 1.10 m_e. The relative shiftss of 33.8 % (Cmcm) and 31.6 % (P4/nmm) are forecasting that these compounds could have problems in fulfilling our requirements for the intrinsic defect screening. This is not the case for $AgPb_2Br_5$, as a relative shift of 59.1 % renders this material rather promising in terms of defect chemistry. An harmonic average of the hole effective mass of 1.07 m_e and a HSE-band gap of 3.07 eV are also acceptable. The major issue with $AgPb_2Br_5$ is the use of lead. Therefore, environmental concerns prevent the usage of this material.

4.2 Study of established p-type materials

Some of the better known p-type materials were further investigated experimentally by one of the SpeedCIGS project partners: the Helmholtz-Zentrum Berlin.[128] Therefore, this chapter serves as a comparison between experimentally known properties and our theoretical calculations. Its structure is along the line of the cited article starting with nickel oxide, followed by copper iodide, copper gallium oxide, molybdenum oxide and finishing with vanadium oxide. The results indicate that, there is still a gap between our

models and experiments in some cases. We suspect that these gaps often result because of incomplete description and underlying assumptions in our models. As an example for an incomplete description, we can look at the hole conductance of a material. It is determined by the hole mobility and concentration. The considered hole effective mass can be used to assess the mobility but not the concentration. We also model perfect crystals with exact stoichiometry. This can be seen as an example of an underlying assumption that is not fulfilled, since in reality we are often dealing with amorphous off-stoichiometry thin films. Detailed understanding of these cases could help to improve the used models.

4.2.1 Nickel oxide and copper iodide

The calculated HSE-band gap is 4.4 eV and differs from the reported values, which are ranging between 3.6 and 4.0 eV. This difference might be traced back to the observation that nickel oxide is often deposited as crystalline thin film without clear defined stoichiometry, whereas for the calculations, NiO with space group $Fm\bar{3}m$ was employed. This also impedes the comparison of the band alignment. Furthermore, the defect chemistry of NiO is also unusual, see Fig. 4.9. The nickel vacancy renders this material intrinsic p-type, but it appears that the suggested dopants do not work. If we assume an error for Li and shift the +I to 0 transition into the gap, then lithium would be a suitable p-dopant, but Cu would still be problematic. We assume that this discrepancy is caused by the fact that we model single crystalline NiO and in reality polycrystalline NiOx is synthesized.[128] This could mean that some of the nickel is in a higher oxidation state, most likely III. In this case copper could work as a p-dopant. But we would still expect that the substitution of Nickel(II) with copper is harmful and expect compensation. In the article, it is mentioned that good crystallinity enhances the performance.[128] Therefore, copper could contribute in some other way, for example by increasing the grain size or promoting the creation of nickel vacancies. We should also mention that p-type undoped nanocrystalline NiO was synthesized by Liang *et. al.*[129] This is in agreement with our findings since the nickel vacancy is rendering this material p-type and no other dopants were used in that study.

In the case of copper iodide, there are three different symmetries, in which it crystallizes: α, β and γ. In the Materials Project Database, a fourth phase is predicted to be the most stable.[63] We investigated β- and γ-CuI, since α-CuI was missing in the database. In the original article, good conduction properties were reported for this compound.[128] This is in agreement with theory, because we find a harmonic average of the hole effective mass of about $0.86\,m_e$ for γ-CuI and $1.17\,m_e$ for β-CuI. This is better than the corresponding values for most of the other examined p-type materials.[86] In the previous section 4.1, we already discussed the good defect chemistry of copper halides. Also it is challenging to find suitable dopants with our screening. We already identified the copper vacancy as a reason for the intrinsic p-type properties of CuI. Experimentally, it is known that CuI can be doped p-type by iodine treatment, which results in an electrochemical reaction between I_2 and CuI withdrawing electrons from the latter.[130] This is again beyond our model since we looked into point defects and did not account

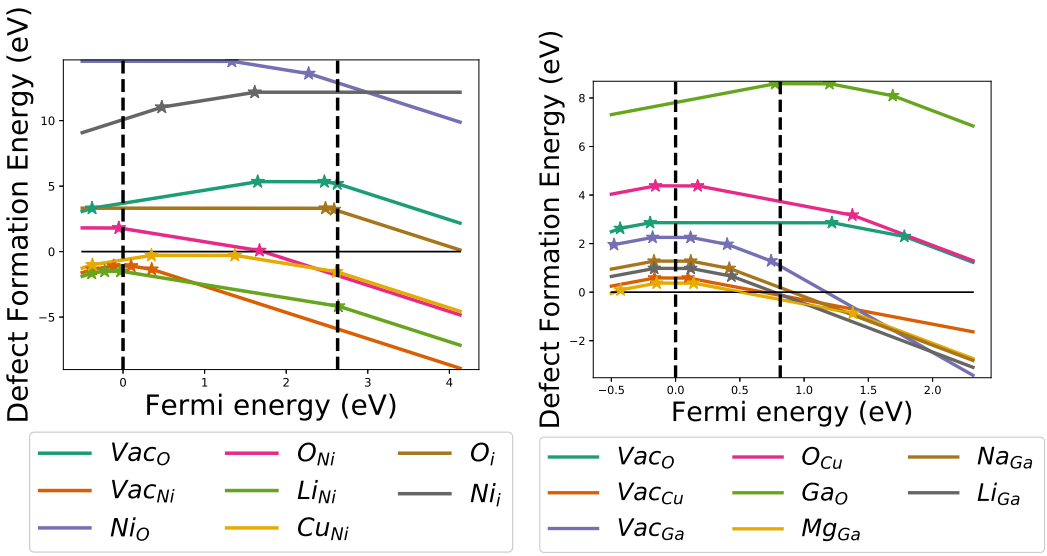

Figure 4.9: Left: Defect chemistry of NiO under O-rich conditions. Lithium and copper are not working as p-dopants. Their failure is likely caused by the assumption of a single crystal of NiO, whereas in reality polycrystaline NiOx is synthesized. Right: Defect chemistry of the delafossite $CuGaO_2$ under O-rich conditions with lithium, magnesium and sodium as p-dopants.

for electrochemical processes.

4.2.2 $CuGaO_2$ and $CuCrO_2$

For copper gallium oxide, we investigated two structures: the experimentally known delafossite structure with R3m symmetry and the theoretically similarly stable $P6_3/mmc$ symmetry, which was not found experimentally. In the original article, it was mentioned that $CuGaO_2$ exhibits a high hole mobility.[128] The eigenvalues of the effective mass tensor are 1.80, 1.80 and 4.07 m_e indicating an anisotropic behavior of the hole mobility for the delafossite structure. Therefore, the harmonic average of the hole effective mass is 2.21 m_e. Although widely used p-type materials have effective masses above 2 m_e, this material does not meet our effective mass screening criterion of being smaller than 1.5 m_e. Owing to this, we would not further consider this material in our screening approach and $CuGaO_2$ demonstrates the strictness of our effective mass criterion. We probably have to relax this criterion even more in order to investigate all p-type materials that are experimentally of relevance. In the article by Rachel Woods-Robinson *et al.*,[86] an effective mass criterion of being smaller than 3 m_e is suggested in order to screen all promising p-type materials. The second investigated structure of $CuGaO_2$ with $P6_3/mmc$ symmetry is even worse in terms of hole effective mass. Its eigenvalues are 2.46, 2.46 and 5.04 m_e yielding a harmonic average of 2.96 m_e. Based on this, it can be concluded that $CuGaO_2$ should crystallize in the delafossite structure for optimal

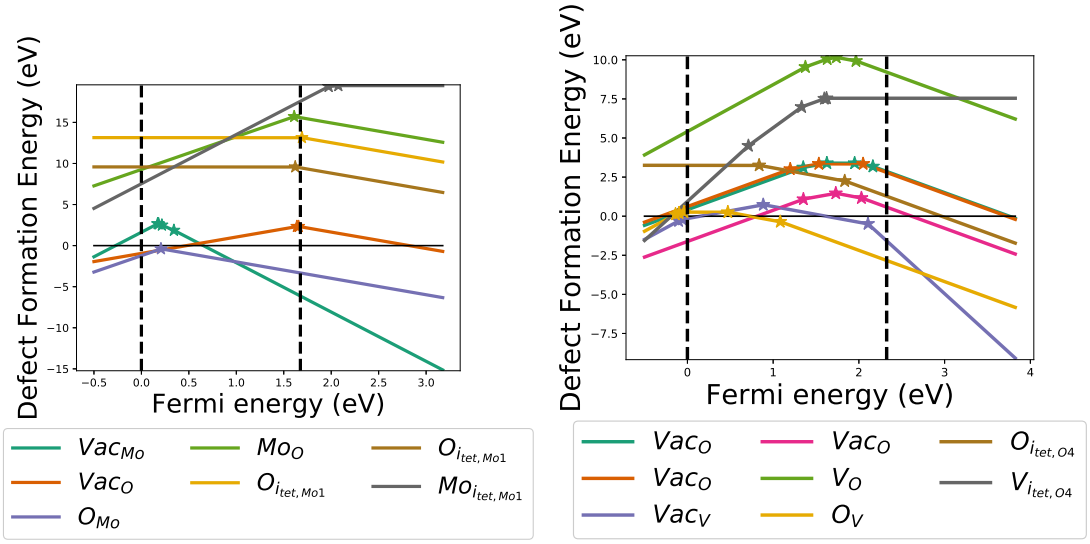

Figure 4.10: Left: Defect chemistry of MoO_3 under O-rich conditions. Right: Defect chemistry of V_2O_5 under O-rich conditions. In both cases, the intrinsic defect chemistry based on point defects is indicating bad p-type performance.

performance.

We also looked into the delafossite structure of $CuCrO_2$, where we found similarities with $CuGaO_2$. The defect chemistry is looking somewhat more promising, since the Cr-vacancy forms more easily supporting the copper vacancy by rendering this material p-type. The distribution of the eigenvalues from the hole effective mass tensor is also similar. There are two directions, in which the transport is more efficient and one associated with a relative high hole effective mass. Overall, the effective masses of 2.69, 2.69 and 18.4 m_e resulting in a harmonic average of the hole effective mass of 3.76 m_e are indicating worse hole mobilities than in case of $CuGaO_2$.

4.2.3 MoO_3 and V_2O_5

Based on the harmonic average of the hole effective masses of 2.30 m_e for MoO_3 and 4.04 m_e for V_2O_5, we expect MoO_3 to exhibit average and V_2O_5 relatively poor performance in terms of hole mobility. The defect chemistry of both materials does not appear promising, see Fig. 4.10. In both cases, the oxygen vacancy is a hole killer defect and therefore strongly limiting the usability of these materials in our opinion. MoO_3 was reported to be an n-type semiconductor and that it can form a p-n-junction, when it is combined with another layer of MoO_3, which is probably in a different structure.[131] The authors explained the differences in hole and electron concentrations by postulating the migration of oxygen. This would result in oxygen vacancies, which could release electrons on one side of the interface and might create oxygen interstitial or antisite defects resulting in holes on the other side. Our simple point defect picture is probably not

sufficient to explain these phenomena for both materials, since we assume the materials to be perfect crystals with a well defined stoichiometry.

Recent results indicate good performance of VOx as hole extraction layer, which is surprising based on our results.[132] But once again, VOx is reported instead of a single crystalline material, which is assumed in our calculations. The other point is the fact that VOx was employed as hole extraction layer. P-type dopability and dopants are not important for this kind of application, but understanding band alignment, carrier-recombination and device-performance is crucial. We calculate the natural band alignment, which is fine with 48.6 % for V_2O_5 for the Pmmn spacegroup symmetry, but does not explain the good performance of VOx. The other two factors are not modeled in our high throughput screening. Owing to this, we are not able to identify good hole extraction layers like VOx in our screening approach. To achieve this, we would have to severely rework our screening process. We would need to use a target absorber surface in order to obtain more realistic band alignment results, to model dynamic processes and to combine device modeling or at least to include findings from device modeling in our screening.

The experimental results on MoO_3 and NiOx are demonstrating that our screening procedure is not able to gather all information indicative of good p-type performance. Different stoichiometries, grain boundaries, amorphous state and interactions with other materials are not taken into account. It would be interesting to theoretically understand the p-type performance of MoO_3 and NiOx. This could lead to the identification of new screening parameters. Furthermore, even a new theoretical screening scheme for hole extraction layers could be established in case of VOx.

4.3 Halide study

The halide study was the first study carried out by the author of this thesis. The relatively strict screening criteria reduced the candidates drastically. In the end, only a handful of materials met these criteria. A literature survey further reduced them and showed some issues with applying our general screening strategy for the specific case of halides. We investigated further materials by relaxing some of the criteria, in order to understand the poor performance of halides. However, these investigations were not carried out rigorously. So some band gaps were only determined on a loose k-point mesh and for some other further investigated materials we have not screened the defect chemistry. For the ones with defect chemistry screening, we stopped after investigating the intrinsic defect chemistry.

4.3.1 Database screening

As of November 2018 around 87000 inorganic compounds could be found in the MPDB and our database query returned 13832 binaries and 41549 ternaries.[63] In this database, the band gap was calculated via DFT employing the GGA functional PBE and for some compounds the GGA+U method was also applied.[80,133] We used a value of 1 eV as PBE-band gap criterion, since the real band gap is often drastically underestimated by

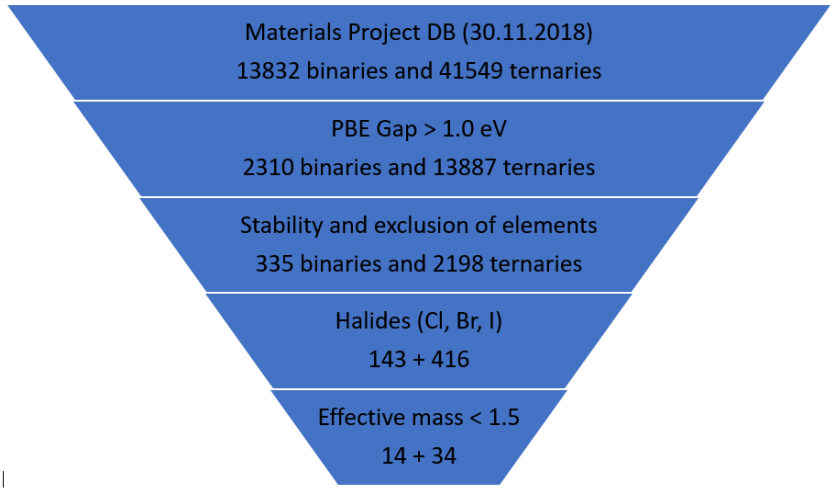

Figure 4.11: Overview of the database screening procedure for halides including the number of investigated compounds in each stage. Further information on the different criteria are given in the text.

this functional.[57,100] This criterion was passed by 2310 binaries and 13887 ternaries. In addition, we restricted the search space to compounds whose energy above the convex hull is 0 eV, as we are only interested in stable materials. From the resulting 646 binary and 5151 ternary compounds, we excluded some materials containing either elements of small interest, *i.e.* hydrogen, elements of the 7th period, noble gases, strontium, cesium, technetium, tantalum, and rare earth elements except scandium, or toxic elements, *i.g.* mercury, cadmium, lead, and arsenic, or fluorine. We expect for the latter to suffer from similar problems as oxides, due to its electronegativity, which is even higher than that of oxygen. From the remaining 335 binary and 2198 ternary compounds, we had to eliminate the ones with more than 50 atoms in their primitive cells due to technical reasons. The obtained 315 binaries and 1809 ternaries were composed of the following halogenides: 56 binaries and 214 ternaries containing chlorine, 44 binaries and 105 ternaries containing bromine, and 43 binaries and 97 ternaries containing iodine. With respect to the effective mass, we are looking further into compounds with a harmonic average for the hole effective mass being smaller than 1.50 m_e and we also excluded 12 binaries and 66 ternaries for which no corresponding value of the harmonic average of the hole effective mass is reported in the dryad repository. For the remaining 15 binaries and 54 ternaries the band alignment was calculated, *vide infra*, yielding also a more accurate estimate for the real value. Therefore, we refined the band gap criterion by requiring that the HSE-band gap is equal or greater than 3.0 eV to ensure transparency. As can be seen in Tabs. 4.3 and 4.4, the described approach based on database screening and band alignment calculations results in 5 binary and 10 ternary halides that are candidates for use as p-type TCM. To further investigate this, we need to calculate the defect chemistry in order to determine p-type dopability and possible dopants.

Table 4.3: List of binary candidates sorted by their HSE-band gaps. For each compound, its MPDB ID, symmetry, HSE-band gap (E_g^{HSE}), harmonic mean hole effective mass ($\overline{m}_h^*$) and relative shift of the CBM are given.

Compound	MPDB ID	Space group	E_g^{HSE} (eV)	$\overline{m}_h^*$ (m_e)	shift CBM
$BaCl_2$	mp-569639	$Fm\bar{3}m$	6.71	1.43	47.7 %
TlCl	mp-568662	$Fm\bar{3}m$	3.60	0.57	52.8 %
AuI	mp-27725	$P4_2/ncm$	3.08	0.70	55.0 %
AuCl	mp-32780	$I4_1/amd$	3.04	0.87	51.8 %
TlBr	mp-568560	$Fm\bar{3}m$	3.01	0.51	50.6 %
TlI	mp-571102	$Fm\bar{3}m$	2.81	0.48	50.1 %
GeI_2	mp-27922	$P\bar{3}m1$	2.76	1.47	38.3 %
AuBr	mp-505366	$P4_2/ncm$	2.76	0.84	50.9 %
AgI	mp-22925	$F\bar{4}3m$	2.52	0.92	27,0 %
AgBr	mp-866291	$F\bar{4}3m$	2.50	1.25	12.6 %
SnI_2	mp-27194	C2/m	2.44	0.88	52.7 %
TiI_4	mp-541013	C2/c	2.01	1.50	53.9 %
InBr	mp-22870	Cmcm	1.85	0.39	47.8 %
InI	mp-23202	Cmcm	1.84	0.32	46.0 %

4.3.2 Band alignment and branch point

We decided to employ and test the relative shift of the CBM as a metric to indicate dopability. For this purpose, the conduction band shift is divided by the size of the band gap. We are using this metric in spirit of the work from Samardian *et. al.*,[98] where oxides were divided into three classes based on position of branch point energy or charge neutrality level. Class I is easily p-type dopable with a branch point energy lying either in the valence band or in the lower fourth of the band gap. This corresponds to a value of at least 75 % in our metric. Class II is easily n-type dopable with a branch point energy lying either in the conduction band or upper fourth of the band gap. Therefore, compounds of this class score less than 25 % in our metric. Class III comprises of the intermediate cases that do not fulfill the requirements for the other two classes and indicates the possibility of ambipolar doping.

As can be seen in Tabs. 4.3 and 4.4, we find no compound that classifies either for class I or class II with the exception of AgBr. The latter exhihibits remarkable good intrinsic defect chemistry, *vide infra*, and is therefore an exception to the rule. The relative shift of the CBM for the binary halides passing our band gap criterion is found around 50 % with a maximum value of 55.0 % and a minimum value of 47.7 %. The latter value is found for $BaCl_2$ and indicates that the shift of the valence band is slightly greater than that of the conduction band. Owing to this, this compound is slightly in favor of n-type doping, whereas for the other four binary compounds with HSE-band gaps above 3 eV it is the other way around resulting in a slight favor of p-type doping. For the ten ternaries with HSE-band gaps above 3 eV, we find a more diverse picture:

Table 4.4: List of ternary candidates sorted by their HSE-band gaps. For each compound, its MPDB ID, symmetry, HSE-band gap (E_g^{HSE}), harmonic mean hole effective mass ($\overline{m}_h^*$) and relative shift of the CBM are given.

Compound	MPDB ID	Space group	E_g^{HSE} (eV)	$\overline{m}_h^*$ (m_e)	shift CBM
Rb_2MnCl_4	mp-22978	I4/mmm	4.34	0.63	53.0%
Rb_2ZnI_4	mp-30018	$P2_1/m$	4.15	1.44	44.9%
KIO_3	mp-23487	P1	3.85	1.28	49.7%
BiClO	mp-22939	P4/nmm	3.68	1.12	38.9%
$Sb_4Cl_2O_5$	mp-23419	$P2_1/c$	3.57	0.72	52.6%
$Sb_4Br_2O_5$	mp-27700	$P2_1/c$	3.25	0.76	51.5%
ScIO	mp-559760	C2/m	3.14	0.72	59.4%
CrClO	mp-24905	Pnnm	3.09	0.82	53.5%
$S(IO_3)_2$	mp-30984	C2/c	3.07	1.44	44.3%
GaTeCl	mp-27449	Pnnm	3.05	0.55	51.7%
Li_4NCl	mp-29149	$R\bar{3}m$	2.84	1.42	43.5%
Ca_3PCl_3	mp-29342	Pm3m	2.83	0.63	43.4%
$RbGeBr_3$	mp-28558	$Pna2_1$	2.71	0.39	58.0%
ZrNCl	mp-568592	$R\bar{3}m$	2.70	1.40	48.4%
$Sb_4I_2O_5$	mp-772282	$P2_1/c$	2.68	0.77	50.4%
InTeBr	mp-29236	$P2_1/c$	2.60	0.86	48.0%
$Rb_3Sb_2Br_9$	mp-28222	$P\bar{3}m1$	2.52	0.92	60.9%
ZrBrN	mp-541912	$R\bar{3}m$	2.52	1.28	49.7%
Ag_2PdCl_4	mp-28557	Cmce	2.46	1.40	55.6%
InTeCl	mp-504630	$P2_1/c$	2.45	1.10	49.1%
SbSI	mp-23041	Pnma	2.35	1.49	45.5%
Tl_6SI_4	mp-27938	P4/mnc	2.35	0.53	46.9%
Tl_2PdCl_4	mp-29889	P4/mmm	2.29	0.85	53.8%
BiIO	mp-22987	P4/nmm	2.27	0.74	35.2%
Tl_6SeI_4	mp-28517	P4/mnc	2.24	0.48	46.2%
BiTeCl	mp-28944	$P6_3mc$	2.16	1.41	34.5%
ZrIN	mp-23052	Pmmn	2.11	0.43	41.4%
In_5S_5Cl	mp-31263	$P2_1/m$	2.07	1.21	53.8%
In_5S_5Br	mp-510347	$Pmn2_1$	1.90	0.82	58.4%
BiTeBr	mp-33723	P3m1	1.89	1.01	38.7%
$NbIO_2$	mp-557685	Pnma	1.88	1.21	51.6%
BiTeI	mp-22965	P3m1	1.86	0.99	41.6%
Zr_6CoCl_{15}	mp-28734	$Im\bar{3}m$	n.DB	1.21	n.DB%
Ba_8P_5Br	mp-34034	$I\bar{4}$	n.DB	1.01	n.DB%

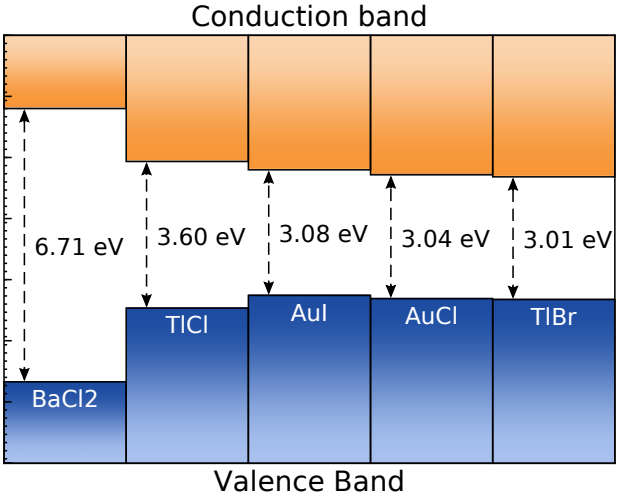

Figure 4.12: Band alignment around the branch point energy for the five binary compounds that fulfilled our HSE-band gap criterion.

KIO_3, Rb_2ZnI_4, BiClO and $S(IO_3)_2$ are in favor of n-type dopability and Rb_2MnCl_4, $Sb_4Cl_2O_5$, $Sb_4Br_2O_5$, ScIO, GaTeCl, and CrClO are in favor of p-type dopability.The minimum and maximum values are 38.9 % and 59.4 %, respectively.

In Figs. 4.12 and 4.13, the band alignment of the halides meeting our HSE-band gap criterion is shown. Ideally, p-type semiconductors should have high-lying conduction and valence bands. No binary halide shows a promising band alignment owing to the similar shifts of both bands. For the ternary halides, ScIO exhibits the biggest relative shift of the CBM and due to a band gap of 3.14 eV, the shift of the VBM (−1.28 eV) is also the smallest among the ternaries passing the HSE-gap criterion. ScIO is therefore the most promising material based on the considerations in this section. In addition, the relative CBM shift of Rb_2MnCl_4 is indicating p-type dopability, but the size of the band gap is shifting the VBM 2.04 eV downwards indicating problems with hole extraction.

4.3.3 Intrinsic defect chemistry

Since the branch point calculations are indicating ambipolar behavior and the relative shift of the CBM is just an indication, we investigated the defect chemistry of all compounds passing our HSE-band gap criterion. Starting with the binaries, we find no hole killer defects for $BaCl_2$, TlBr and TlCl in the anion rich region, and no hole killer defects in both regions for AuCl and AuI. From branch point calculations, we only expect $BaCl_2$ not to be in favor of p-type dopability. Employing this approach also for ternary halides, we would expect KIO_3, Rb_2ZnI_4, BiClO and $S(IO_3)_2$ to fail our p-dopability criterion and in fact we find that these components form hole killing defects in all regions with the exception of KIO_3, which passes our criterion in the anion rich region.

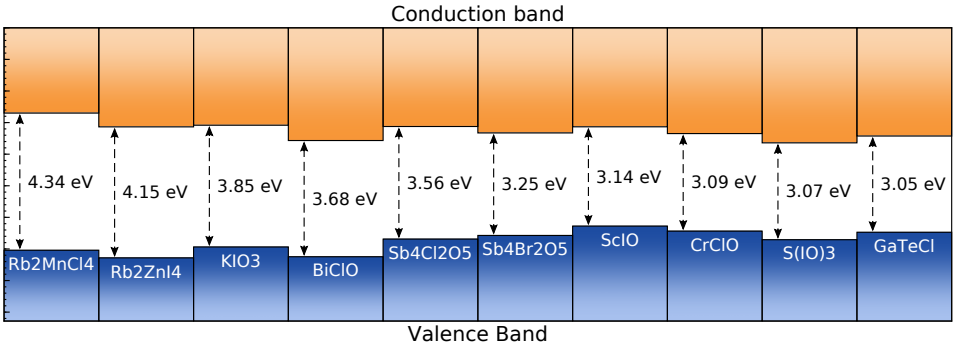

Figure 4.13: Band alignment around the branch point energy for the ten ternary compounds that fulfilled our HSE-band gap criterion.

For Rb_2MnCl_4, $Sb_4Cl_2O_5$, $Sb_4Br_2O_5$, ScIO, GaTeCl and CrClO, which were indicated to be likely p-dopable based on band alignment, we find that the two oxides containing antimony are not p-dopable at all. Interestingly, the other chloro oxide, CrClO, does show p-dopability in all regions. Therefore, it is the most promising ternary compound after this intrinsic defect screening, since Rb_2MnCl_4, ScIO and GaTeCl require to be synthesized in anion rich conditions. Overall, we observe for the binaries good agreement between the predictions from branch point calculations with their computed intrinsic defect chemistry. For the ternaries, there is some disagreement between branch point calculations and defect chemistry. Nevertheless, the branch point concept appears to be working fine for these materials. Accepting the possibility of discarding some suitable compounds, computations can be saved by relying more on the branch point concept and defining appropriate alignment and relative shift criteria.

4.3.4 Dopants

We are assessing suitable dopants by investigating extrinsic point defects, but we do not take into account dopants such as iodine or bromine, which could withdraw electrons from a compound *via* an electrochemical reaction. Therefore, the binaries containing thallium do not meet this requirement, as they can be doped p-type only in the anion rich region suggesting that we have to substitute thallium with an oxidation state of +1 with an element of lower oxidation state. The binaries containing gold are better suited, since they are also p-dopable in the cation rich region and therefore we can search for suitable dopants, which will replace the halide in these compounds. We tried to substitute it with the elements O, S, or Se. Although Se leads to a low formation energy, the state is rather deep in the gap indicating that this defect will not create holes in the valence band. Nonetheless, the gold vacancies are promising and since this is also true for the thallium vacancies, we conclude that AuCl and AuI as well as TlCl and TlBr could be used as intrinsic p-type semiconductors without any dopant. As shown

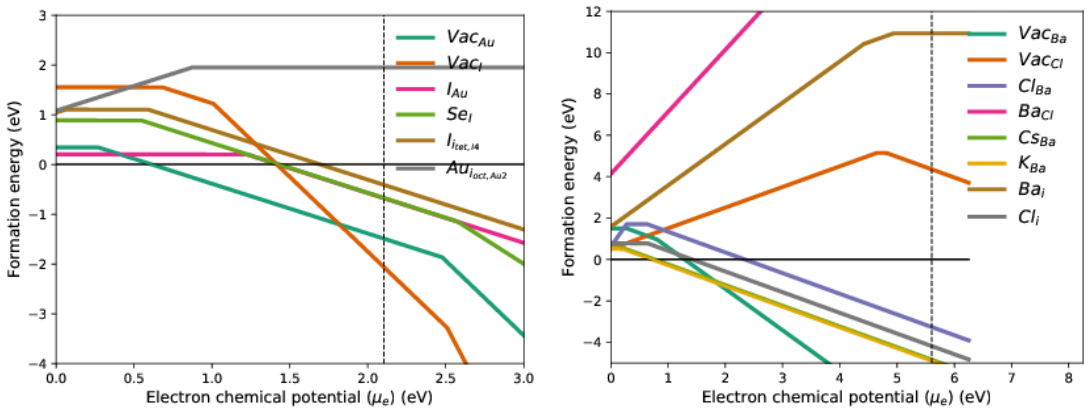

Figure 4.14: Left: Defect chemistry of AuI under I-rich conditions. Intrinsic doping caused by the Au-vacancy seems to be the only way to achieve a hole concentration in AuI. Right: Defect chemistry of $BaCl_2$ under Cl-rich conditions with K and Cs, which as possible dopants have nearly the same formation energy.

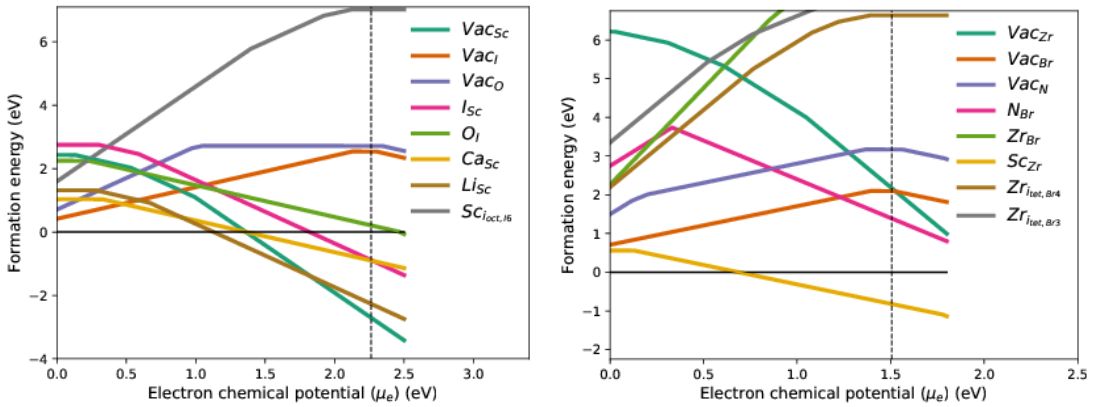

Figure 4.15: Left: Defect chemistry of ScIO in the I−ScOI−Sc_2O_3 region. Although the intrinsic defects are promising, we did not find any suitable dopant due to Fermi-pinning, which is shown for the more promising candidates Li and Ca. Right: Defect chemistry of ZrNBr in the N_2−ZrNBr−$ZrBr_3$ region. With Sc as potential dopant.

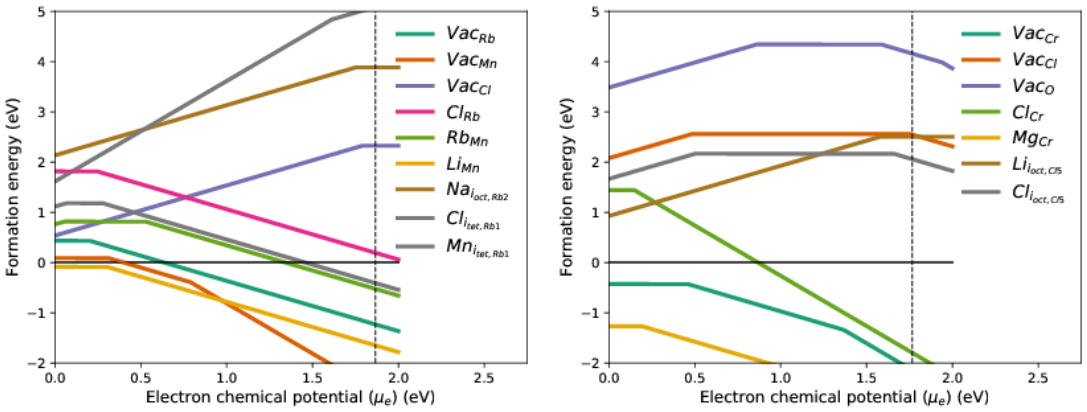

Figure 4.16: Left: Defect chemistry of Rb_2MnCl_4 in the RbCl−Rb_2MnCl_4−Rb_2MnCl_6 region. Most of the 0 to 1 transitions are near the valence band and the -1 to 0 transitions are near the conduction band. Right: Defect chemistry of CrOCl in the $CrCl_3$−CrOCl−ClO_2 region. The activation energy for the vacancy of chromium is rather high. Doping the material with magnesium seems to be the better strategy in order to achieve a high hole concentration.

in the right picture of Fig. 4.14, potassium and cesium seem to be good candidates in order to dope $BaCl_2$ p-type. However, this is a close call, as the Cl-vacancy is crossing the formation energy near the valence band energy. If this happens before reaching the valence band, we would have Fermi pinning and we would consider the dopant not suitable.

For the ternaries, we can first eliminate KIO_3, as it is similar to the case of thallium halides and there is also the chance that this material is intrinsic p-type due to the potassium vacancy. Furthermore, Fermi pinning could happen, since it is crossed by the oxygen vacancy shortly before the valence band. This would imply that no high hole carrier concentrations could be reached in this material. GaTeCl, ScIO, and ZrNCl are just barely passing our intrinsic defect criterion under anion rich conditions. Owing to this, it is not surprising that all the assessed dopants were either not acceptable or got pinned. ScIO is shown as an example for this in Fig. 4.15, as this compound was considered to be most promising based on branch point calculations.

The intrinsic defect chemistry of Rb_2MnCl_4 is depicted in Fig. 4.16. This compound is also passing our intrinsic defect criterion under anion rich conditions and we find that substitution of manganese with, *e.g.*, sodium should increase the hole concentration. The final compound, CrClO, is passing the intrinsic defect criterion in all regions. For this compound, several possible p-dopants are found, which are all in the position of chromium. Unfortunately, this eliminates also two of the possible regions, since we have to apply Cr-poor conditions to achieve successful doping.

4.3.5 Discussion and literature survey

Our database and HSE-band gap screening is rather strict for halides. It reduces the number of interesting materials to 5 binary and 10 ternary halides including some unusual compounds. All five binaries contain cations that can be found in the sixth row of the periodic table. Most of the ternary halides that are meeting our database and band gap screening criteria consist of two anions with the exception of Rb_2MnCl_4 and Rb_2ZnI_4. In addition, GaTeCl assumes an exceptional role, as all the other compounds are composed of oxyhalides. Interestingly, this compound also passes our band gap criterion, which is not met by the other non-oxo chalcohalides. Noteworthy is also oxoiodine(III) sulfate $(IO)_2SO_4$: It consists of three elements, which are normally anionic. It is therefore not surprising that this compound is unstable to moisture.[134]

Intrinsic p-type

AuCl, AuI, TlBr, TlCl and KIO_3 did not pass our dopant screening. Nevertheless, the cation vacancy should create holes rendering these materials intrinsic p-type. AuCl is a yellowish solid, which will react to Trichlorhydroxogold(III) acid when solved in water.[109] AuI is also a yellow solid, which will decompose when contacted with water, moisture or light.[109] This indicates that we overestimated the band gap in our HSE-band gap screening. The overestimation of the band gap is probably due to the neglect of relativistic effects, which are important for materials containing heavy elements and or gold.[135]

The structures for AuCl ($I4_1/amd$) and AuI ($P4_2/ncm$) found in the MPDB are based on experimentally determined crystal structures and in absentia of theoretical alternatives they of course match the experimental data. The toxic materials TlBr and TlCl are experimentally found to crystallize in the CsCl-type.[110] The rock-salt structure is the most stable one according to MPDB. As the energies of these structures are nearly the same,[136–138] it was found that a rock-salt thin film can be created when grown on a suitable substrate, for example KBr.[139,140] The low effective mass of the rock-salt structure can be explained by the results of Ha *et al.*:[141] They found a favorable coordination for the hole effective mass if the angle between alkali or earth alkaline metal cation, anion, and second cation is 180°. This is fulfilled in the rock-salt structure of TlBr and TlCl. It should also be mentioned that TlBr is discussed as material for X-ray applications owing to its scintillator properties.[142]

Potassium iodate, KIO_3, is a white crystalline powder, a well known oxidizing agent and with five phases its phase diagram is rather complex.[143] MPDB predicts the triclinic phase with space group P1, which is stable at room temperature, to be the most stable. DFT predicts stability at 0 K and 0 atm and as such the low temperature phases of KIO_3 should have been found to be the most stable. Crystals with triclinic symmetry can be grown on KI via an reaction involving ozone.[144] Our results indicate that KIO_3 could form electron-hole pairs due to the potassium vacancy. It would therefore be interesting if a hole concentration can be detected for this compound.

Table 4.5: List of polymorphs for the compounds that pass the screening in the main study by either having suggested dopants or being potentially intrinsic p-type. The structures, which we investigated in our study, are marked by writing the compound name in **bold**. Binaries are sorted alphabetically by their cation and from the lighter to the heavier anions. The only ternary material KIO_3 with its polymorphs is found at the bottom of this table. Different structures are sorted by their HSE-band gaps. For each material, its MPDB ID, symmetry, HSE-band gap (E_g^{HSE}), eigenvalues of the hole effective mass and harmonic mean hole effective mass ($\overline{m}_h^*$) in m_e and relative shift of the CBM are given. The HSE band gap calculations were performed with a density of 100 k-points per reciprocal atom.

Material	MPDB ID	Space group	E_g^{HSE} (eV)	m_h^*1	m_h^*2	m_h^*3	$\overline{m}_h^*$	shift CBM
AuCl	mp-1120780	$P4_2/ncm$	3.09	n.a.	n.a.	n.a.	n.a.	52.2%
AuCl	mp-32780	$I4_1/amd$	3.04	0.40	2.02	2.03	0.87	51.8%
AuBr	mp-570140	$I4_1/amd$	3.08	0.43	2,54	2.55	0.96	48.2%
AuBr	mp-505366	$P4_2/ncm$	2.76	0.56	0.56	61.0	0.84	50.9%
AuI	mp-27725	$P4_2/ncm$	3.08	0.47	0.47	38.4	0.70	55.0%
$BaCl_2$	mp-569639	$Fm\bar{3}m$	6.71	1.43	1.43	1.43	1.43	47.7%
$BaCl_2$	mp-23199	Pnma	6.41	2.19	2.74	3.66	2.74	46.2%
$BaCl_2$	mp-567680	$P\bar{6}2m$	5.87	2.45	3.74	3.74	3.18	41.5%
TlCl	mp-568662	$Fm\bar{3}m$	3.60	0.57	0.57	0.57	0.57	52.8%
TlCl	mp-571079	Cmcm	3.46	0.63	0.85	1.26	0.84	44.6%
TlCl	mp-23197	$Pm\bar{3}m$	3.39	0.54	0.54	0.54	0.54	43.7%
TlBr	mp-22875	$Pm\bar{3}m$	3.09	0.66	0.66	0.66	0.66	42.0%
TlBr	mp-568560	$Fm\bar{3}m$	3.01	0.51	0.51	0.51	0.51	50.6%
TlBr	mp-568949	Cmcm	2.94	0.34	0.48	1.23	0.51	42.6%
TlI	mp-571102	$Fm\bar{3}m$	2.81	0.48	0.48	0.48	0.48	50.1%
TlI	mp-22858	Cmcm	2.81	0.38	0.40	5.66	0.57	43.0%
TlI	mp-23197	$Pm\bar{3}m$	2.47	0.66	0.66	0.66	0.66	35.8%
KIO_3	mp-23487	P1	3.85	0.90	1.58	1.67	1.28	n.a.%
KIO_3	mp-552729	R3m	3.49	0.72	1.34	1.34	1.04	42.8%
KIO_3	mp-1080058	R3c	n.a.	n.a.	n.a.	n.a.	n.a.	n.a.%
KIO_3	mp-558843	$Pm\bar{3}m$	n.a.	n.a.	n.a.	n.a.	n.a.	n.a.%

$BaCl_2$

$BaCl_2$ is soluble in water, hygroscopic and toxic. Depending on the conditions, it can crystallize in one of three forms: cubic, hexagonal or orthorhombic.[145] The cubic form is of CaF_2-fluorite type and according to MPDB the most stable one. Experimentally, this form is reported to be metastable at room temperature and stable at higher temperatures.[145] As shown in Tab. 4.5, it is the most interesting phase for hole conduction due to its low hole effective mass. Recently, transparent ceramics made of cubic $BaCl_2$ were reported.[146] This raises the question if the addition of KCl and CsCl would increase the hole concentration in these ceramics.

For the Pnma-phase of $BaCl_2$ Kumar *et. al.* reported some interesting results.[147] Already the PBE functional yields a band gap of 5.14 eV overestimating the experimental value of 4.96 eV by 0.16 eV. Consequently, our HSE result of 6.41 eV, further overestimates this gap. There is also disagreement regarding the effective mass: $0.95\,m_e$ was found by Kumar via curve fitting, but $2.19\,m_e$ is the smallest value stated in the dryad database.

For p-type semiconductor applications, $BaCl_2$ with $Fm\bar{3}m$ symmetry seems less favorable and one can even question if it is still a semiconductor owing to its large HSE-band gap of 6.7 eV. Although this value could be an overestimation, a gap larger than > 5 eV is still large. In combination with the nearly homogeneous shift of the VBM and CBM relative to the branch point energy, a very low-lying VBM is found. This will lead to a band alignment, where the extraction of holes from another material by $BaCl_2$ is difficult. Additionally, superionic properties due to migration *via* anion Frenkel defects are also discussed for the CaF_2-structure of $BaCl_2$.[148]

Rb_2MnCl_4

Rb_2MnCl_4 is a transparent, orange, antiferromagnetic perovskite.[149,150] Crystals can be grown *via* the vertical Bridgman technique.[151] The structure consists of layers of $MnCl_6$ octahedra, where 4 in-plane lying Cl-atoms are shared with the next Mn-atom. It has a tetragonal unit cell, since the layers are shifted by $a/2$.[149,150] The orange color can be attributed to a photoluminescence process.[152] The absorption spectrum exhibits several bands for energies higher than 550 nm, see ref. 153 and references therein. In contrast to this, our screening is indicating no absorption in the visible range and an indirect gap. This is also remarkable, because perovskites usually exhibit a direct band gap.[154]

Nonetheless, we also see the mixing of anion p-orbitals with orbitals from the metal, which is typical for perovskites.[154] In contrast to methylammonium lead iodide, $MAPbI_3$, where the iodine p-orbital is contributing the most to the VBM, we find for Rb_2MnCl_4 that the manganese d-orbital is dominant. There is also agreement for the Rb_2MnCl_4 results regarding the shallow nature of the defects and the fact that the cation vacancies will make the perovskite p-type under the right growth conditions.[154] However, we did not see any particular defect tolerance. We are aware of the challenges of doping perovskite p-type[155] and therefore expect problems when trying to perform the doping with the suggested dopants.

CrClO

The magnetic material CrClO can be doped p-type with Li, Be, Ca, and Mg in the position of Cr. Mg on Cr is proving to be the most promising dopant, since it has the lowest formation energy and it is also the one that is the closest to the valence band. Owing to its strongly correlated electrons, oxyhalides are well known as Mott-Hubbard insulators.[156] CrClO is a green solid, so it is also colored violating our transparency criterion.[156] The cause of the coloration could be unrelated to our HSE-band gap result. Nevertheless, our description of this material seems to be improvable and further theoretical investigations might be required to assess the validity of our results. For this purpose, dynamical mean field theory could be employed, similar to what was published for CrO_2.[157]

4.3.6 Shortcomings of the screening approach

As shown in the discussion, the screening of halides was not very successful. After literature comparisons, only barium chloride is surviving the screening, because Rb_2MnCl_4 and CrClO are not transparent. It is therefore interesting to ask ourselves: What is the reason behind the failure of our screening strategy? In order to illuminate this question, we will analyze some of our screening criteria.

We already discussed the issue of polymorphism. Therefore, we will start with the stability criterion, which is closely related to it. We expect this to be important for binaries, since polymorphism is more often encountered in the binary compound space. This is also the reason, why the known p-type semiconductor CuI is not appearing in our starting list. The stability criterion, energy above the convex hull equals 0 eV, did lead to the selection of CuI in the $Pm\bar{3}m$ symmetry. The eigenvalues of the hole effective mass tensor are 2.07, 2.07 and 7.70 m_e and therefore failing our hole effective mass screening criterion. As shown the in the binary study in section 4.1 $\beta-$CuI and $\gamma-$CuI would pass that criterion, although they would still fail the HSE-band gap criterion, due to their small band gaps. But nevertheless, this could mean that other materials exhibit polymorphs, which would pass our screening or that we overlooked materials, which are deemed unstable by the convex hull criterion, but are still synthesizable.

Energy above convex hull

We have slightly relaxed the stability criterion for Tab. 4.6 and owing to this synthesizability is not guaranteed for these compounds. Except for IO_2, $NbBr_5$ and Te_3Cl_2, we found polymorphs of already investigated binary materials. We also note that just TlCl and AuBr are passing the band gap criterion and that, with the exception of InCl, the relative shift of CBM is predicting ambipolar behavior with an n-type tendency. The ternaries are more interesting, as most of them are new compounds. KIO_3 and ZrBrN are the only polymorphs and Li_5NCl_2 and $Rb_3Mn_2Cl_7$ are based on Li_4NCl and Rb_2MnCl_4. Interestingly Li_5NCl_2 is passing the HSE-band gap criterion, whereas Li_4NCl did fail. However we have to be careful with these values, since these materials have been screened on a loose k-point mesh.

Table 4.6: List of candidates with an energy above the convex hull between 0 and 0.02 eV divided into binary and ternary compounds and sorted by their HSE-band gaps. For each compound, the relation to our screened compound (N = new material, P = structural polymorph, S = different stoichiometry), MPDB ID, energy above convex hull ($E_{\text{above hull}}$), symmetry, HSE-band gap (E_g^{HSE}), harmonic mean hole effective mass ($\overline{m}_h^*$) and relative shift of the CBM are given. The calculations were performed with a density of 50 k-points per reciprocal atom.

Compound	kind	MPDB ID	$E_{\text{above hull}}$ (eV)	Space group	E_g^{HSE} (eV)	$\overline{m}_h^*$ (m_e)	shift CBM
TlCl	P	mp-571079	0.02	Cmcm	3.77	0.85	46.7%
AuBr	P	mp-570140	0.012	$I4_1/amd$	3.08	0.96	48.0%
CuI	P	mp-22863	0.014	P4/nmm	2.90	0.90	40.3%
CuI	P	mp-569346	0.009	$P6_3mc$	2.69	1.17	39.5%
CuI	P	mp-32750	0.007	R3m	2.67	1.18	40.6%
CuI	P	mp-673245	0.009	Pc	2.65	0.95	37.2%
CuI	P	mp-22895	0.002	$F\bar{4}3m$	2.61	0.86	36.5%
$NbBr_5$	N	mp-568245	0.002	$P\bar{1}$	2.57	0.38	50.8%
IO_2	N	mp-23170	0.011	$P2_1/c$	2.53	1.14	51.9%
AgI	P	mp-684580	0.002	$I\bar{4}m2$	2.47	0.91	27.2%
InCl	P	mp-571636	0.002	$Cmc2_1$	2.34	0.492	57.0%
InCl	P	mp-571555	0.002	Cmcm	2.34	0.490	56.7%
Te_3Cl_2	N	mp-27628	0.013	$P2_1/c$	2.04	1.22	49.1%
Ba_2CaI_6	N	mp-756725	0.007	$P2_1/c$	4.60	1.47	50.1%
KIO_3	P	mp-552729	0.005	R3m	4.24	1.04	46.1%
$Rb_3Mn_2Cl_7$	S	mp-23556	0.002	I4/mmm	4.03	0.90	49.4%
$KMnCl_3$	N	mp-23049	0.013	Pnma	4.01	0.86	50.9%
Rb_2MnBr_4	N	mp-27263	0.017	I4/mmm	3.67	0.53	n.a.%
Li_5NCl_2	S	mp-29151	0.005	$R\bar{3}m$	3.08	1.44	48.7%
$InSn_2Br_5$	N	mp-23507	0.005	I4/mcm	3.07	1.23	43.5%
$MgInBr_3$	N	mp-29483	0.011	Pnma	3.02	1.30	44.1%
ZrBrN	P	mp-570157	0.014	Pmmn	2.72	0.74	48.2%
$TlGeI_3$	N	mp-29288	0.014	Pnma	2.58	1.49	44.8%
Ba_2P_7Cl	N	mp-569613	0.001	$P2_1/m$	2.55	0.68	54.9%
Tl_6SCl_4	N	mp-28242	0.011	P4/mnc	2.45	0.37	51.4%
Tl_6SBr_4	N	mp-28518	0.001	P4/mnc	2.45	0.43	50.2%
Sn_4SI_6	N	mp-540644	0.001	C2/m	2.06	1.08	41.4%
$AgTe_3I$	N	mp-570431	0.018	Pmna	1.8	0.89	50.4%

Table 4.7: List of compounds with low effective masses in one direction sorted by their HSE-band gaps. For each material, its MPDB ID, symmetry, HSE-band gap (E_g^{HSE}), eigenvalues of the hole effective mass and harmonic mean hole effective mass ($\overline{m}_h^*$) in m_e and relative shift of the CBM are given. The calculations were performed with a density of 50 k-points per reciprocal atom.

Material	MPDB ID	Space group	E_g^{HSE} (eV)	m_h^*1	m_h^*2	m_h^*3	$\overline{m}_h^*$	shift CBM
$RbGeCl_3$	mp-27369	$P2_1/m$	4.99	0.93	6.59	64.8	2.43	50.9%
K_2ZnBr_4	mp-23535	$P2_1$	4.92	0.81	10.20	27.0	2.19	42.4%
ScBrO	mp-546279	Pmmn	4.76	0.77	2.73	108	1.79	51.2%
$AlInI_4$	mp-571260	$P2_1/m$	3.84	0.82	1.97	4.55	1.54	52.0%
$AuPCl_4$	mp-23355	$P2_1/c$	3.83	0.67	5.91	11.0	1.71	53.3%
$NbOBr_3$	mp-606393	$P\bar{4}2_1m$	3.06	0.94	183.5	183.5	2.79	51.6%

Except for Li_5NCl_2 and KIO_3, all of the passing compounds have two metals in their composition and are therefore metal halides, which we missed in the main study. Their branch point is classifying them as ambipolar, so that defect chemistry needs to be checked, although the relative shifts of $InSn_2Br_5$ (43.5%) and $MgInBr_3$ (44.1%) are suggesting favorable n-type doping. This is of interest, since indium chloride has the opposite tendency (57.0% and 56.7%). For the materials not passing the HSE-band gap criterion, we have a similar picture as for the ones not passing this criterion in the main study.Chalcohalides, except for ZrNBr, Ba_2P_7Cl and $TlGeI_3$.

The HSE-band gap of Ba_2P_7Cl 2.55 eV is quite remarkable, since phosphor compounds in general suffer under small band gaps as can be seen in the binary (section 4.1) and pnictide (section 4.4) studies. The relative shift of the CBM for Ba_2P_7Cl of 54.9% is also indicating p-type favorable defect chemistry. Additionally, $Cu_3P_{15}I_2$ did pass our intrinsic screening in all regions and it is therefore likely that Ba_2P_7Cl would also pass this screening. However, we stopped the investigation of the compounds mentioned in this section after the HSE-band gap screening on a loose k-point mesh and we have not performed intrinsic defect screening for any of the components, since the new materials do not have stable phases on the convex hull. If we just used our routine approach, PyCDT would try to relate the defects to the next stable composition leading to questionable results. We therefore would need a way to relax the stability criterion in PyCDT in order to find the right phase or to provide a phase diagram of our own.

Effective mass

For Tab. 4.7, we changed the definition of the hole effective mass criterion by just considering the smallest value of the eigenvalues. We also calculated the intrinsic defect chemistry for these materials with the exception of $AlInI_4$, for which we stopped the calculations, as they turned out to be too time consuming. Instead, we changed the indium pseudo potential (In d to In), which did speed up the calculations. We therefore

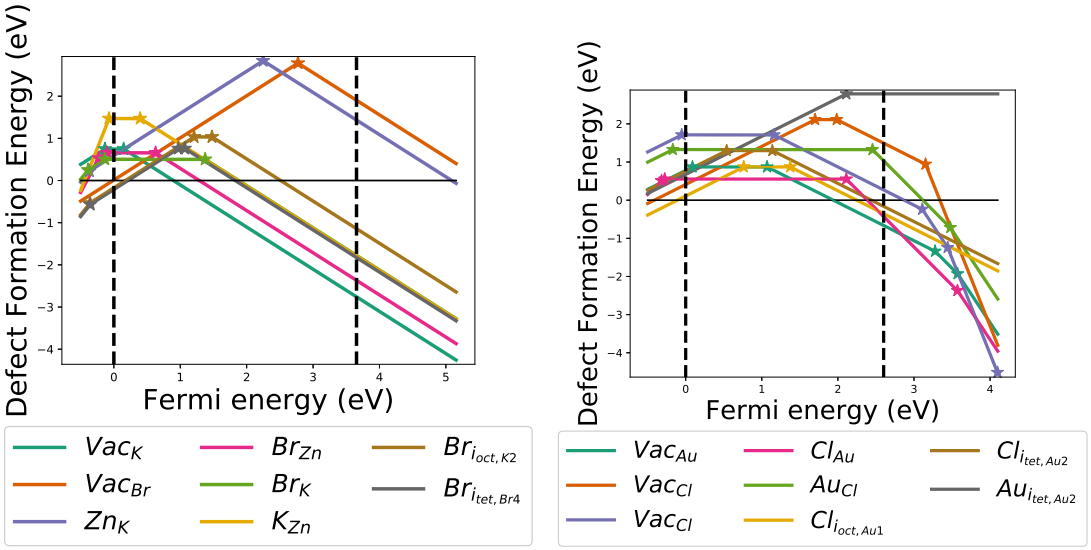

Figure 4.17: Left: Defect chemistry of K_2ZnBr_4 in the K_2ZnBr_4−KBr−Br-region. The bromine interstitial defects are hole killing. Right: Defect chemistry of $AuPCl_4$ in the $PAuCl_8$−$PAuCl_4$−PCl_3-region. The gold vacancy is not critical, but the chlorine insterstitial is not leaving much room for dopants.

were able to get some preliminary results for this compound indicating no p-dopability and defects with low formation energies. But as mentioned the results are incomplete and could also be misleading, due to the missing phase diagram calculations.

Based on the branch point, we expect most of the compounds to be in favor of p-type dopability. K_2ZnBr_4 is the only compound, where we would expect favorable n-type dopability. The defect chemistry is showing the opposite trend, as the potassium vacancy is surely killing electrons in all regions, see Fig. 4.17. In contrast to this, p-type dopability is looking more promising as the bromine vacancy can be controlled by choosing Br-rich conditions. Interestingly, we encountered problems with bromine interstitial defects, which are hole killing in the bromine-rich environment. This material is therefore not dopable at all. In ScOBr we also found problems with bromine interstitial defects, when we try to control the formation of bromine vacancy and scandium antisite defects. In both cases, the use of Br-rich conditions is helpful, but bromine interstitial defects become hole killing under these conditions rendering this materials also not p-dopable. For $NbOBr_3$, we are not able to control the vacancy of oxygen, which is hole killing in all regions.

This leaves $AuPCl_4$, which exhibits a quite interesting defect chemistry, see Fig. 4.17. In this structure, three Cl-atoms are bound to phosphorus, whereas the remaining one is bound to the gold atom.[158] This results in a little odd behavior: The vacancies of the three chlorine atoms bound to phosphorus are not that aggressive when it comes to releasing electrons, but the one bounded to the gold atom is still problematic. Therefore, Cl-rich conditions seem advantageous, but they are not necessary since this compound is

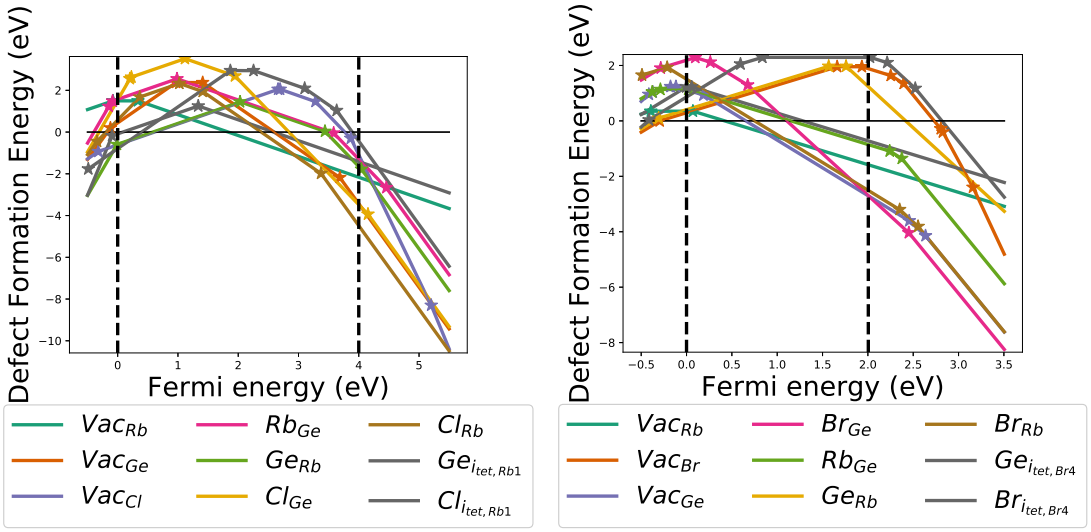

Figure 4.18: Left: Defect chemistry of $RbGeCl_3$ in the $Ge_3Cl_8-RbGeCl_3-Ge$-region. Cl-rich conditions are not enough to render the chlorine vacancy not hole killing and the antisite defect of germanium in the position of rubidium is becoming just as troublesome. Right: Defect chemistry of $RbGeBr_3$ in the $GeBr_2-RbGeBr_3-GeBr_4$-region. The vacancy of bromine and the antisite defect have a similar behavior as for the previous compound, but they are not hole killing anymore due to the smaller band gap.

already passing the intrinsic screening under Cl-poor conditions. For Cl-rich conditions we are facing a new problem, as chlorine is able to form one interstitial, which can release electrons rendering these conditions not much better than the Cl-poor ones. Finding a p-dopant is therefore becoming a challenging task. Gold has the oxidation state I, which does not support any dopant. P has the oxidation state III and is π backbonded to gold. Owing to this, we need an element with oxidation state II, which is also π backbonded to gold in order to keep the geometry. Chlorine in oxidation state -I is the only candidate were we do not have arguments against finding a p-dopant. The only problem is the chlorine interstitial or chlorine vacancy, which will highly likely lead to Fermi pinning of p-dopants.

Finally, $RbGeCl_3$ is the last material, for which we have to discuss its intrinsic defect chemistry, see Fig. 4.18. The PBE-band gap of around 4 eV is troublesome. Even though the defect chemistry is comparable to $RbGeBr_3$, see the following subsection, the gap is leading to a situation, where a lot of defects are hole killing.

HSE-band gap

The other parameter that could be relaxed, is the HSE-band gap criterion. These compounds are already listed in the main table and we therefore only list the materials in Tab. 4.8 again, for which we screened the intrinsic defect chemistry. We ended the last

Table 4.8: List of ternary candidates with low HSE-band gaps, but screened intrinsic defect chemistry sorted by their HSE-band gaps. For each compound, its MPDB ID, symmetry, HSE-band gap (E_g^{HSE}), harmonic mean hole effective mass ($\overline{m}_h^*$), relative shift of the CBM as well as the result of the intrinsic defect screening are given. The calculations were performed with a density of 100 k-points per reciprocal atom.

Compound	MPDB ID	Space group	E_g^{HSE} (eV)	$\overline{m}_h^*$ (m_e)	shift CBM	intr. defects
Li_4NCl	mp-29149	$R\bar{3}m$	2.84	1.42	43.5%	p-type
Ca_3PCl_3	mp-29342	Pm3m	2.83	0.63	43.4%	negative
$RbGeBr_3$	mp-28558	$Pna2_1$	2.71	0.39	58.0%	p-type
ZrNCl	mp-568592	$R\bar{3}m$	2.70	1.40	48.4%	p-type
$Sb_4I_2O_5$	mp-772282	$P2_1/c$	2.68	0.77	50.4%	negative
$Rb_3Sb_2Br_9$	mp-28222	$P\bar{3}m1$	2.52	0.92	60.9%	negative
ZrNBr	mp-541912	$R\bar{3}m$	2.52	1.28	49.7%	p-type
ZrIN	mp-23052	Pmmn	2.11	0.43	41.4%	negative

subsection mentioning $RbGeBr_3$ which was not able to pass our HSE-band gap criterion in the main study, but did exhibit a remarkable good value for the harmonic average of the hole effective mass. The eigenvalues are 0.32, 0.42 and 0.47 m_e resulting in a harmonic average of 0.39 m_e. Compared to $RbGeCl_3$, which was failing the hole effective mass criterion, this can not only be attributed to the substitution of chlorine with bromine in the formula. In fact, we also have a change in symmetry: $RbGeCl_3$ crystalizes in $P2_1/m$ symmetry, whereas $RbGeBr_3$ crystalizes in $Pna2_1$, am orthorhombic perovskite structure.

Compared to $RbGeCl_3$, the defect chemistry of $RbGeBr_3$ is more typical for perovskites, *e.g.* the charge transition happens near the valence or conduction band, where in $RbGeCl_3$ the charge transition is found more in the center. This makes especially the bromine vacancy, which exhibits a comparable formation energy than the chlorine vacancy in $RbGeCl_3$, dangerous for $RbGeBr_3$. Owing to the smaller PBE-band gap of around 2 eV, $RbGeBr_3$ is passing the intrinsic defect screening, where $RbGeCl_3$ failed. The branch point concept applied to $RbGeBr_3$ agrees also with these results. We note that the relative shift of the CBM 58 % is indicating ambipolar behavior. For the other material $Rb_3Sb_2Br_9$ which has a high relative shift of the CBM 60.9 % and for which we would strongly expect p-type dopability, we see facile formation of many kinds of defects making this material most likely not dopable with both p- and n-dopants.

The other materials failing the intrinsic defect screening are $CaPCl_3$ and $Sb_4O_5I_2$. For $Sb_4O_5I_2$, we already screened the related compounds $Sb_4O_5Cl_2$ and $Sb_4O_5Br_2$. We again note the same trend that was observed in the binary section 4.1, *i.e.* an improvement of the defect chemistry when going from chlorine to bromine to iodine. But this time, the improvement for the iodine compound is not sufficient to ensure p-dopability. Therefore, $Sb_4O_5I_2$ as well as the other two compounds in the main study fail the intrinsic defect screening, although the branch point is indicating a slight favor for p-type dopability. For

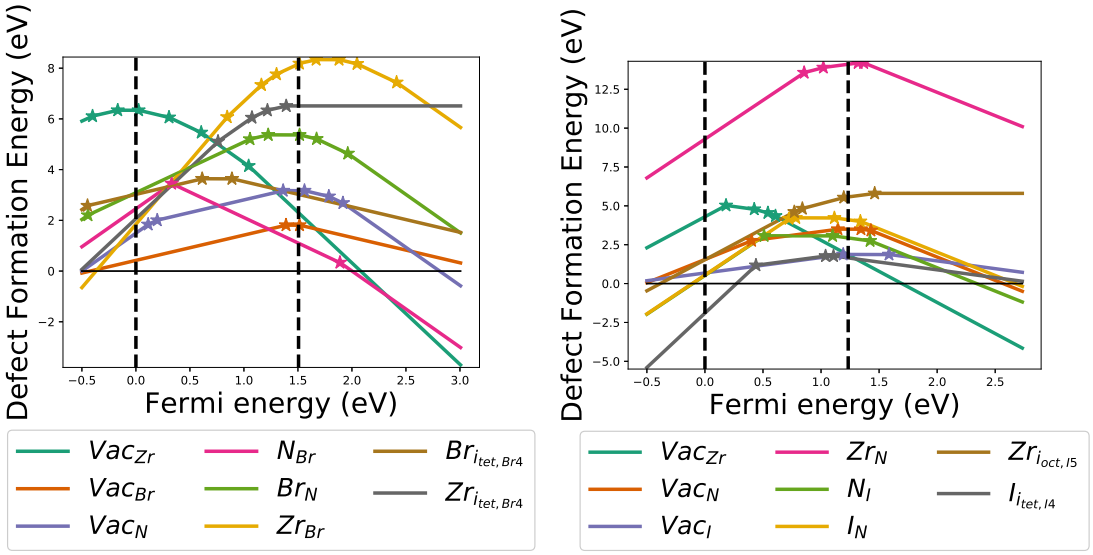

Figure 4.19: Left: Defect chemistry of ZrNBr in the $ZrNBr-ZrBr_4-N_2$-region. Although the bromine vacancy is not hole killing anymore, it is still the most troubling defect and could be problematic for doping attempts. Right: Defect chemistry of ZrNI in the ZrI_4-IN_4-ZrNI-region. We do not see a better intrinsic defect chemistry compared to ZrNBr due to the different structure. The iodine interstitial is even hole killing.

Ca_3PCl_3, the branch point is indicating the opposite and the defect chemistry confirms it. Ca_3PCl_3 is also failing the intrinsic defect chemistry screening. The chlorine vacancy can be controlled by employing Cl-rich conditions, but the antisite defect Cl on P and the calcium interstitial defect remain hole killing under these conditions. Compared to other halides, the defects in Ca_3PCl_3 exhibit quite high formation energies leaving hope for the remaining metal nitride halides.

Even though the branch points of ZrNCl, ZrNBr, ZrNI and Li_4NCl are indicating favorable n-type dopability, almost all of them pass our intrinsic defect screening and Li_4NCl even in all regions, see Figs 4.19 and 4.20. ZrNX compounds with X = Cl, Br or I are special, since they are known superconductors.[159] They exist as layered structures with $R\bar{3}m$ symmetry (ZrNCl and ZrNBr) and Pmmn symmetry (ZrNI). Interestingly, we see the formation of hole killing iodine interstitial defects in ZrNI rendering this material not p-dopable in all regions, which is not a problem for ZrNCl and ZrNBr, as both are p-dopable under anion-rich conditions. We investigated intercalation for these materials, as it could introduce a new source of hole killing defects if metals occupy these positions. On the other hand, intercalation could also be an opportunity for p-type doping *via* an electron withdrawing compound, *e.g.* oxygen. Since the bromine and chlorine atoms are pointing outwards in that structure, it is probably more likely that metal intercalation takes place.

A lot of chalcohalides were also among the compounds that did not meet the HSE-band

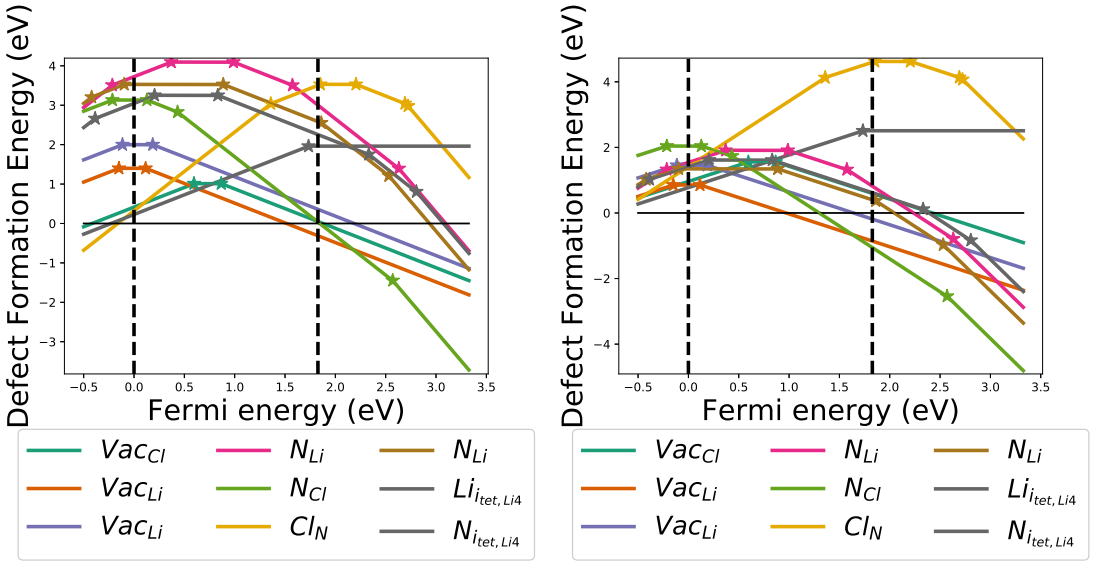

Figure 4.20: Left: Defect chemistry of Li_4NCl in the $Li_4NCl-LiCl-Li$-region. The vacancy of chlorine, the antisite defect chlorine on nitrogen and the interstitial defect of lithium are problematic for p-type doping. Right: Defect chemistry of Li_4NCl in the $Li_4NCl-LiN_3-LiCl$-region. All of the mentioned defects can be controlled by applying Cl-rich and Li-poor conditions.

gap criterion. We investigated GaTeCl in our main study, this component did pass the intrinsic defect screening, but we were not able to find a suitable dopant. Other ternary halides with tellurium, selenium or sulfur could also have favorable defect chemistry, but they were not investigated further.

Choice of elements

The choice of elements is also something, which we can tweak in order to find more promising materials. Our decision to leave out fluorides seems to be questionable, as in a recent high-throughput study undertaken by Ha *et al.*, most of the halides that qualified for further investigations were fluorides.[160] Indeed, if we include fluorides in our screening, we obtain several promising perovskite structures, see Tab. 4.9. Interestingly, this was not the case for chlorine, bromine and iodine containing compounds. The A-site of the perovskites is dominated by potassium leading to the argument, that there is a stability maximum for this kind of compounds due to the similar size of potassium and fluorine.[161] By looking at the relative CBM shifts, we note that perovskites with manganese as B-site ions are most likely to be p-dopable ($52.2 - 57.5\,\%$). In contrast to this, perovskites with nickel as B-site ion appear most likely to be n-dopable ($35.5 - 36.2\,\%$).

Perovskites based on potassium and manganese seem to be promising. With about 4 eV, they also exhibit the lowest band gaps of the screened perovskites. However,

Table 4.9: List of ternary fluoride perovskites sorted by their HSE-band gaps. For each compound, its MPDB ID, symmetry, perovskite structure classification, HSE-band gap (E_g^{HSE}), harmonic mean hole effective mass ($\overline{m}_h^*$) and relative shift of the CBM are given. The calculations were performed with a density of 50 k-points per reciprocal atom.

Compound	MPDB ID	Space group	Perovskite	E_g^{HSE} (eV)	$\overline{m}_h^*$ (m_e)	shift CBM
K_2ZnF_4	mp-9583	I4/mmm	2D	6.76	1.44	37.4%
$KZnF_3$	mp-5878	$Pm\overline{3}m$	3D	6.22	1.30	33.5%
Tl_2SiF_6	mp-5033	$Fm\overline{3}m$	0D	6.21*	1.40	45.9%*
Rb_2NiF_4	mp-561317	I4/mmm	2D	5.26	1.06	36.3%
K_2NiF_4	mp-556546	I4/mmm	2D	5.25	0.17	36.1%
$K_3Ni_2F_7$	mp-560449	I4/mmm	2.5D	5.24	0.10	36.1%
$TiTl_2F_6$	mp-10402	$P\overline{3}ml$	0D	5.17	1.55	52.1%
$AlTl_2F_5$	mp-27758	Cmcm	1D	5.10	1.32	46.6%
$K_3Mn_2F_7$	mp-554144	I4/mmm	2.5D	4.15*	1.32	52.8%
$RbMnF_3$	mp-558749	$Pm\overline{3}m$	3D	4.09	1.20	55.0%
K_2MnF_4	mp-558547	I4/mmm	2D	4.03	1.21	55.6%
$KMnF_3$	mp-558046	Pnma	3D	3.98*	1.31	57.5%*
Sn_2OF_2	mp-27480	C2/m		3.52	1.47	50.4%
Sn_2IF_3	mp-27167	$C222_1$		3.25	0.89	50.2%
InOF	mp-27175	Fddd		2.84	1.15	16.6%
Ca_2NF	mp-33588	$I4_1/amd$		2.72	1.22	32.7%

we stopped the investigations on p-type perovskites, as theoretical investigations of perovskites are challenging and because it is hard to dope them p-type. The non-perovskites are similar to what we have found for most of the halides in the main study, *i.e.* double anion compounds and preferably oxides. In the same study it was found that compounds containing hydrogen were not p-dopable because of hydrogen vacancies.[160] This further justifies our choice to leave out hydrogen.

Perovskites

In light of the results for fluorine based ternaries, we would have expected more perovskites in our main study, since they posses low hole effective masses. We can only speculate, why we have not encountered more of them. Firstly, we have confined our search to binary and ternary compounds, which will exclude perovskites like $CH_3NH_3PbI_3$, where the complex ion $CH_3NH_3^+$ is found at the A site of the perovskite. Secondly and based on a preliminary screening of the perovskite-tagged materials in the MPDB, we observe that among the compounds with a suitable PBE-band gap a lot of them do not contain any halide or are composed of elements, which we have excluded in our search. Therefore, we assume that we have eliminated most of the ternary halide perovskites with the PBE-band gap criterion and with excluding certain elements.

Further investigations would probably be interesting, but we should also keep in mind that the production of perovskite is solution based. We are therefore not sure if our single point defect picture is sufficient to describe the defect chemistry of this class of materials. As mentioned in the subsection 4.3.5 of the main study for Rb_2MnCl_4, perovskites can exhibit photoluminescence, which will make the HSE-band gap screening insufficient for guaranteeing transparency. Furthermore, p-doping is problematic for them. This would mean that we can not just look at the point defects, but also have to ask ourselves if this defect is achievable.

$BaCl_2$ and alkaline earth metal chemistry

We can also look more closely at the group of metal halides, in which we found the most promising material in this study: $BaCl_2$. All alkaline earth metals exhibit a more than sufficient band gap, but most of them do not meet the criterion for the effective mass, see Tab. 4.10. In the MPDB, the CaF_2-structure of $SrCl_2$ and $BaCl_2$ is found to be the most stable one. It seems that this structure is providing a good hole conduction and, as could be expected, the effective mass of $1.21\,m_e$ for $SrCl_2$ is indicating an even better conduction than for $BaCl_2$ with $1.43\,m_e$. Keeping the structure and substituting Sr or Ba with Ca, Mg, or Be should result in even better values, but these structures are not found in the MPDB.

We also looked at calcium fluoride, whose name is used for denoting the structure of the mentioned alkaline earth metal halides. We note for that structure that it has the best harmonic average of the hole effective mass compared to other CaF_2 structures. It is a pity that bromide and iodine combined with alkaline earth metals do not form CaF_2-structures, as we would expect even better hole effective masses and smaller band

Table 4.10: List of alkaline earth metal halides starting with $BaCl_2$ followed by lighter earth alkaline metals and ending with CaF_2. For a given compound, structures are sorted by their HSE-band gaps. Structures with 0 eV above convex hull are marked by writing the name in **bold**. Structures marked with * are not based on experimentally determined crystal structures. For each structure, its MPDB ID, symmetry, HSE-band gap (E_g^{HSE}), eigenvalues of the hole effective mass and harmonic mean hole effective mass ($\overline{m}_h^*$) in m_e and relative shift of the CBM are given. The calculations were performed with a density of 50 k-points per reciprocal atom.

Material	MPDB ID	Space group	E_g^{HSE} (eV)	m_h^*1	m_h^*2	m_h^*3	$\overline{m}_h^*$	shift CBM
$BaCl_2$	mp-569639	F$\bar{3}$m	6.71	1.43	1.43	1.43	1.43	47.7%
$BaCl_2$	mp-23199	Pnma	6.41	2.19	2.74	3.66	2.74	46.2%
$BaCl_2$	mp-567680	P$\bar{6}$2m	5.87	2.45	3.74	3.74	3.18	41.5%
$SrCl_2$	mp-23209	F$\bar{3}$m	6.50	1.21	1.21	1.21	1.21	46.5%
$CaCl_2$	mp-571642	Pbcn	7.02	2.57	8.91	9.19	4.92	46.8%
$CaCl_2$	mp-23214	Pnnm	6.89	1.94	3.14	5.22	2.93	47.4%
$CaCl_2$	mp-22904	$P4_2/mnm$	6.84	2.33	2.33	2.83	2.48	47.8%
$CaCl_2$	mp-571627	Pnma	6.64	4.52	15.5	20.7	8.98	44.7%
$CaCl_2$*	mp-1120739	F$\bar{3}$m	6.53	n. a.	n. a.	n. a.	n. a.	50.1%
$MgCl_2$	mp-23210	R$\bar{3}$m	7.07	1.58	6.97	6.97	3.26	39.8%
$MgCl_2$	mp-570259	P$\bar{3}$m1	6.99	1.27	6.83	6.83	2.78	40.2%
$MgCl_2$*	mp-570782	P$\bar{1}$	6.57	1.94	3.89	200	3.86	42.8%
$MgCl_2$*	mp-570922	P$\bar{4}$m2	6.32	3.89	3.89	56.4	5.64	36.5%
$MgCl_2$*	mp-571387	Pmma	5.66	0.73	6.44	104	1.95	42.0%
$MgCl_2$*	mp-569626	Ama2	4.79	1.21	2.85	3.72	2.07	33.7%
$BeCl_2$*	mp-570227	I$\bar{4}$3m	8.01	2.33	2.33	2.83	2.48	50.0%
$BeCl_2$	mp-570974	$I4_1/acd$	7.94	n. a.	n. a.	n. a.	n. a.	48.3%
$BeCl_2$*	mp-1190080	I$\bar{4}$3m	7.94	n. a.	n. a.	n. a.	n. a.	45.2%
$BeCl_2$	mp-23267	Ibam	7.73	2.01	5.11	268	4.30	44.8%
$BeCl_2$*	mp-569030	$P3_221$	7.68	n. a.	n. a.	n. a.	n. a.	47.0%
$BeCl_2$*	mp-1172909	I$\bar{4}$3m	n.a.	n. a.	n. a.	n. a.	n. a.	n.a.
CaF_2	mp-10464	Pnma	9.62	3.68	5.18	9.02	5.21	44.2%
CaF_2	mp-2741	F$\bar{3}$m	9.19	2.18	2.18	2.18	2.18	43.4%
CaF_2	mp-560030	$Pmc2_1$	8.46	3.51	3.87	10.0	4.66	43.5%
CaF_2	mp-554355	P4/mmm	7.49	1.90	1.90	33.4	2.77	41.5%

gaps. Band gaps are a general problem for these compounds and it is likely that a lot of the listed compounds are insulators and not semiconductors. The hypothetical Ama2 structure of $MgCl_2$ has the smallest HSE band gap, but with 4.79 eV, it would already violate the upper HSE-band gap limit of 4.3 eV, which was used in the ternary chalcogenide screening.

The special case of $Cu_3P_{15}I_2$

$Cu_3P_{15}I_2$ is a good example to show some limitations of our approach. The primitive cell contains 80 atoms. The eigenvalues of the effective mass are 0.49, 0.78 and 3.95 m_e resulting in a harmonic average of 0.84 m_e. This is exceptionally good for halides, although we should compare this compound more with phosphides due to the small amount of iodine compared to phosphorus. Phosphorus containing compounds are known to exhibit good hole effective masses.[162] The interesting point would therefore be the question if this compound will pass our HSE-band gap criterion. We can not answer that question since we have not calculated this property.

Our current workflow, which is using a normal workstation computer for the PBE optimization and one node (16 CPUs and 64 GB RAM) on a cluster for the HSE-band structure calculation, is not able to handle such big systems. The defect chemistry screening is of course doable, as a single node is sufficient to handle a 160 atom cell on the PBE level. The problem we faced with the defects was the creation of too many defect calculations. PyCDT was not able to recognize the symmetry and did therefore create 160 vacancy defects, 160 x 2 antisite defects and 99 interstitial defects, which could be occupied by one of the 3 elements. This resulted 777 defects and 6640 calculations, as the defects can have different charge states.

We manually intervened at this point and selected some of the defects to avoid screening all of them. So far, the intrinsic defect chemistry is quite promising, see Fig. 4.21. $Cu_3P_{15}I_2$ is passing our intrinsic defect screening in all regions and the copper vacancy is already providing an intrinsic hole concentration. Copper-poor conditions are needed in order to avoid copper interstitial defects, which can pin the vacancy. The big question for this compound is the HSE-band gap and therefore transparency, since phosphides exhibit in general small band gaps.

4.3.7 Conclusions

In this first computational screening study on Cl-, Br-, and I-containing compounds, most of those materials found in the Materials Project Database do not match our criteria for p-type TCMs. The criteria for stability, transparency and hole effective mass are already eliminating most of the candidates and the remaining compounds are relatively uncommon. Among them, we identify $BaCl_2$ doped with Cs and K as binary candidate for p-type TCM applications and CrClO doped with Mg and Rb_2MnCl_4 doped with Na, as ternary candidates. However, by performing a literature survey, we identified issues with the mentioned materials, which were not covered by our screening strategy.

One aspect related to stability is photochemistry. One of the binary candidates that

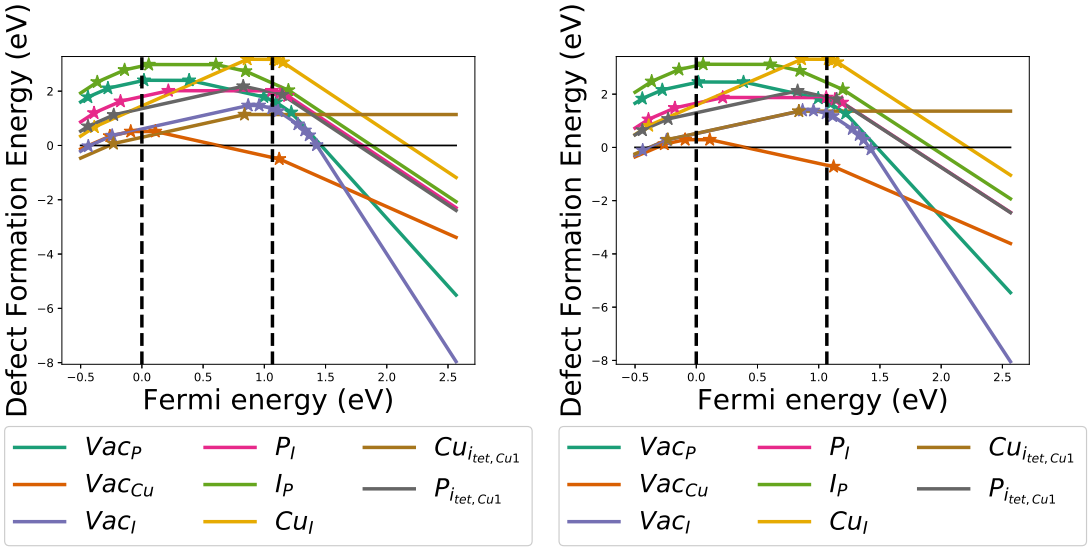

Figure 4.21: Left: Defect chemistry of $Cu_3P_{15}I_2$ in the Cu_2P_7–$Cu_3P_{15}I_2$–PI_2-region. The iodine vacancy and the copper interstitial are problematic for p-type dopants. Right: Defect chemistry of $Cu_3P_{15}I_2$ in the CuP_{10}–$Cu_3P_{15}I_2$–P-region. Under these conditions the mentioned defects are less harmful and we already have the copper vacancy as an intrinsic source for holes.

was eliminated because of the HSE-band gap was silver bromide, which is known for its photosensitivity.[125] If silver bromide had passed that step, we would have had no criterion to eliminate it. Other halides could also suffer from photoinstability. Another aspect of photoinduced processes is photoluminescence, for which we would need to look into excited states of the materials. This might have helped us to sort out Rb_2MnCl_4, which is a orange solid due to a photoluminescence process.

By relaxing some of our criteria, we discovered that the effective mass and stability criteria are the reason for sorting out ternary mixed cation compounds. Regarding their defect chemistry, these compounds do not seem to be promising except if they posses a perovskite structure. Perovskites are quite exceptional and are probably one way to find ternary p-type halides. The other would be the use of a second anion. Nitrogen and phosphorus appeared promising, although the HSE-band gap of these compounds was too small. This was the reason, why they were not discovered in the main study, and only by relaxing HSE-band gap criterion. Even though oxygen did not perform good for this purpose, other chalcohalides could also work, which were not investigated owing to their small HSE-band gaps. By comparing our screening criteria with the ones defined in ref. 86, we have to admit that we only investigated a fraction of the space, in which possible p-type TCMs can be found.

4.4 Pnictide study

In the second study carried out by the author of this thesis, we investigated nitrogen- and phosphorus-containing binaries and ternaries. These materials performed better than halides. This is mainly because of the promising properties of the nitrogen-containing materials. The phosphorus-containing materials face problems passing the band gap criteria and in fact, there is no phosphide among the candidates for defect chemistry screening with the exception of hexaboron phosphide. We decided to focus more on the chemical aspect and hence divided the intrinsic defect chemistry screening of ternaries into different classes. The focus of our literature survey is on our employed screening criteria and we provide a thorough discussion of the final candidates at the end of this section.

4.4.1 Database screening and branch point

From the 133,691 compounds that existed in the MPDB in February 2019, we are interested in the 9233 compounds containing nitrogen (N) and the 14052 compounds containing phosphorous (P). This includes nitrides and phosphides as well as nitrates, phosphates, and further 2 atomic anions. Based on our criterion for the band gap, the materials should exhibit a PBE-band gap greater than 1 eV, which reduces the list to 4834 N- and 7673 P-containing compounds. We also require these materials to be stable, therefore enforcing the strict criterion that they should lie on the convex hull ($E_{above\,hull} = 0\,\mathrm{eV}$). This reduces our candidates to 1007 N- and 2058 P-containing compounds. Furthermore, we only consider materials with less than 50 atoms in the primitive cell to allow efficient HSE-band gap screening. From the remaining 623 N- and 1257 P-containing compounds, we exclude the ones containing elements from the 7th period or gold, which is also known to exhibit strong relativistic effects,[135] since our screening does not account for such effects. Rare earth elements (except scandium), hydrogen, noble gases, arsenic, strontium, cadmium, cesium, hafnium, technetium, tantalum, mercury and lead are also excluded. This leads to 236 N- and 649 P-containing compounds and among them are 18 binaries and 154 ternaries containing N as well as 34 binaries and 204 ternaries containing P.

In general, our screening criteria are in favor of binary and ternary compounds with the exception of the PBE-band gap criterion and also of the stability criterion for binary nitrides. This explains the enrichment of binaries and ternaries among the total number of N- and P-containing compounds. In the beginning, 40 % of the N-containing compounds are binaries or ternaries, whereas in the end there are 73 %. We see a similar but weaker trend for P-containing compounds starting with 27 % and ending with 37 % binaries or ternaries.

Next, we require from our candidates to have a harmonic average of the hole effective mass smaller than $1.5\,\mathrm{m_e}$. 17 binaries as well as 58 ternaries fulfill this criterion. This also excludes 7 binaries and 108 ternaries, for which no data on the effective mass could be found in the Dryad repository. Since P is less electronegative than N, we expect more P-containing compounds and in fact 13 of the 17 binaries and 35 of the 57 ternaries

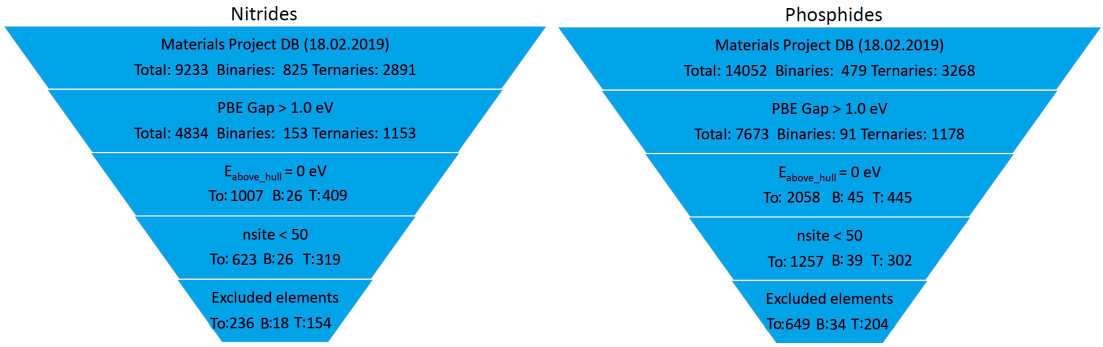

Figure 4.22: Overview of the database screening procedures for nitrides (left) and phosphides (right). Together with each step also the number of compounds fulfilling this criterion are given. These numbers are given for all N- and P-containing compounds (To) as well as for binaries (B) and ternaries (T).

contain this element. We should also mention that 1 binary and 3 ternaries contain both nitrogen and phosphorus.

The final criterion is the HSE-band gap. The size of the band gap correlates often with the difference in electronegativity. Thus it is more likely to find transparent materials in the compound space of a low electronegative metal or a high electronegative non-metal element. Therefore, we are now facing the opposite trend relative to the the effective mass. For the ternaries, this leads to the situation that all phosphides are eliminated. The remaining P-containing compounds are dominated by phosphates and chalcophosphates, but we also found 3 nitridophosphates. For the remaining 17 N-containing compounds, we obtain a mixed picture: 7 compounds with two anions and 11 compounds with two cations. Both P- and N-containing materials are dominated by main group elements, especially calcium and magnesium are quite often encountered.

We also use the HSE-calculations for predicting the band alignment *via* the branch point method. A good p-type semiconductor should have a small shift of the valence band maximum (VBM), but a strong shift of the conduction band minimum (CBM). Therefore, we are employing the relative shift of the CBM as a metric, which is defined as the CBM shift divided by the size of the band gap. From this perspective, our selected compounds are not performing very well, as most of the relative shifts are under 50 %. In contrast to this, common p-type materials exhibit often shifts between 50 - 60 %.[86] We want to point out that a shift under 50 % could be problematic for applications, where the band alignment is important. This holds in particular for systems with large band gaps, as such gaps are resulting also in huge shifts of the VBM, when the split is more or less even.

4.4.2 Defect chemistry

For the defect calculations, we employ the three steps mentioned in the method section 3.6. In the first step, we are looking for intrinsic hole killer defects, *i.e.* donor

Table 4.11: List of N- or P-containing binary candidates sorted by their HSE-band gaps. For each compound, its MPDB ID, symmetry, HSE-band gap (E_g^{HSE}), harmonic mean hole effective mass ($\overline{m}_h^*$) and relative shift of the CBM are given.

Compound	MPDB ID	Space group	E_g^{HSE} (eV)	$\overline{m}_h^*$ (m_e)	shift CBM
Si_3N_4	mp-988	$P6_3/m$	5.71	1.13	50.4%
AlN	mp-661	$P6_3/mc$	5.42	1.03	42.7%
BN	mp-7991	$P6_3/mmc$	5.41	0.94	54.6%
P_3N_5	mp-567907	C2/c	4.97	1.08	50.4%
Be_3N_2	mp-18337	$Ia\overline{3}$	4.56	1.17	36.9%
Ge_3N_4	mp-672289	P31c	3.55	1.52	34.5%
B_6P	mp-28395	$R\overline{3}m$	3.23	0.84	48.9%

defects with low formation energies. If a compound has hole killers in all regions it is failing this criterion. The next step is the p-dopant search. We are looking for shallow acceptor defects with a sufficient low formation energy to avoid Fermi pinning. Finally, we are investigating self-compensation and therefore looking at the interstitial and antisite defects of the dopant. If we see no self-compensation, the material and dopant pass our defect screening.

Binaries

The binaries that passed our screening criteria so far are shown in Tab. 4.11. We also included Ge_3N_4 due to its similarity Si_3N_4, even though its harmonic average of the effective mass of $1.52\,m_e$ is slightly above our screening threshold. Be_3N_2 is the only binary compound failing the intrinsic defect screening criterion due to beryllium interstitial defects. Furthermore, we find hole killer defects in AlN and Ge_3N_4. In both cases, the metal interstitial appears to be as problematic as the N-vacancy. However, the formation of both defects can be hindered by synthesizing the compounds under N-rich conditions. This is not sufficient for Ge_3N_4, as we see Fermi pinning for the tested dopants and therefore it is failing our extrinsic screening. In the case of AlN, the shift of the formation energies of the defects is relatively high and as can be seen in Fig. 4.23, we are able to identify Be, Mg and Zn in position of Al as dopant candidates. Although we observe Fermi pinning for beryllium in the position of aluminum caused by its interstitial defect, magnesium and zinc remain possible p-dopants.

No hole killing defects in any region of BN and Si_3N_4 are found, not even the Si interstitial defect in Si_3N_4,which is the most troublesome defect. In contrast to Ge_3N_4, the anion vacancy is the limiting factor in Si_3N_4. This defect is easily compensated due to the high formation energy of Ca on Si. For beryllium, we observe a problem with its interstitial defect and in the end, both elements are not suitable p-dopants for Si_3N_4. Al and Ga in the position of Si remain as possible p-dopants. For BN, beryllium in the position of boron does not look promising, since it is crossed by the antisite defect, *i.e.* N in position of B, slightly behind the valence band and the charge transition from +1

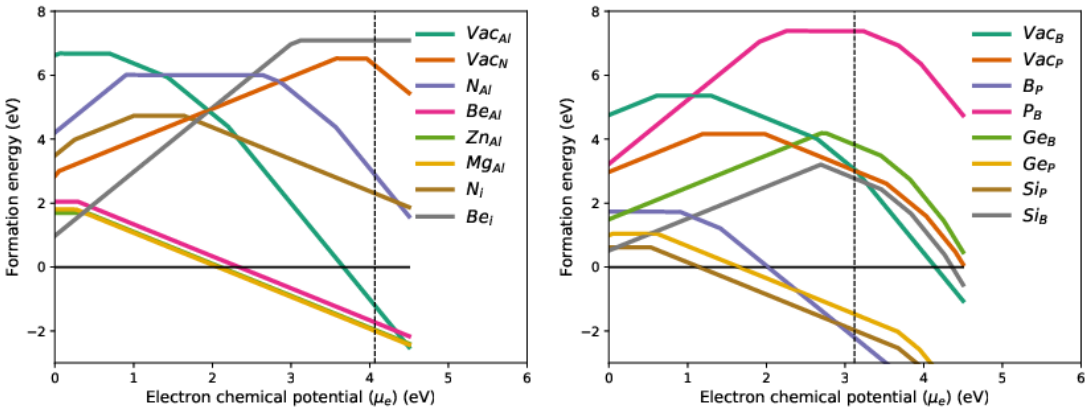

Figure 4.23: Left: Defect chemistry of AlN under N-rich conditions. Only zinc is a possible p-dopant due to Fermi pinning of beryllium. Right: Defect chemistry of B_6P under B-rich conditions. We find Fermi pinning of silicon and only germanium is a possible p-dopant.

to 0 is rather deep in the gap. Therefore, it is a rather bad candidate, so we were not able to identify any good dopant for boron nitride.

Triphosphorus pentanitride, P_3N_5, has no hole killing defects, but is suffering from N-vacancies. So during synthesis, N-rich conditions need to be employed in order to ensure p-dopability. Under these conditions, Si in the position of P appears to be promising for hole doping. The defect chemistry of hexaboron phosphide, B_6P, shown in Fig. 4.23, is a little uncommon. It also exhibits no hole killing defects in all regions and the defect that is the most dangerous for p-dopants is P in the position of B when comparing both conditions. This enforces P-poor conditions during synthesis. This defect is also the reason why we only identified Ge in position of P as possible p-dopant. We observe Fermi pinning for Si at the same position, which exhibits a slightly higher formation energy.

Ternary Nitrides

The ternary nitrides that passed our screening criteria up to the HSE-band gap are shown in Tab. 4.12. In the case of $MgGeN_2$, the hole killing defect is not a vacancy but the substitution of Mg with Ge. This antisite defect is a typical problem for nitrides with two cations. In general, it can be expected for these compounds, when they are containing two cations with different charges but similar ionic radii.[163] Interestingly, we encounter this hole killing defect in just one compound for all regions, even though Li_3GaN_2, LiMgN, Li_3ScN and $ZnGeN_2$ consist of cations with similar radii and different charges. Only MgGeN fails our intrinsic screening due to compensation in all regions.

For LiMgN and $ZnGeN_2$, this defect can be suppressed by synthesizing the compounds under anion-rich and Mg- or Ge-poor conditions. In Li_3GaN_2 and Li_3ScN, the formation energy of this defect is already so high that synthesizing them under anion-rich conditions

Table 4.12: List of ternary nitride candidates sorted by their HSE-band gaps. For each compound, its MPDB ID, symmetry, HSE-band gap (E_g^{HSE}), harmonic mean hole effective mass ($\overline{m}_h^*$) and relative shift of the CBM are given.

Compound	MPDB ID	Space group	E_g^{HSE} (eV)	$\overline{m}_h^*$ (m_e)	shift CBM
$MgGeN_2$	mp-7798	$Pna2_1$	3.93*	1.24	30.8%
Li_3GaN_2	mp-3887	$Ia\bar{3}$	3.65*	1.27	39.6%
LiMgN	mp-37906	$F\bar{4}3m$	3.45	1.40	30.7%
Li_3ScN	mp-542435	$Ia\bar{3}$	3.26	1.48	43.2%
$ZnGeN_2$	mp-2979	$Pna2_1$	3.05*	1.36	22.2%
$BaSiN_2$	mp-3777	Cmce	3.99	0.90	52.4%
$CaGeN_2$	mp-7801	$I\bar{4}2d$	3.58	1.01	43.3%
$Ca_5(SiN_3)_2$	mp-571333	C2/c	3.25*	1.22	46.5%
$Ca_3(GaN_2)_2$	mp-571162	C2/c	3.01*	0.77	39.9%
$MgBe_2N_2$	mp-11917	$P\bar{3}m1$	5.35	1.33	48.9%
$CaMg_2N_2$	mp-5795	$P\bar{3}m1$	3.05	1.36	36.2%

is sufficient to ensure hole dopability as shown in Fig. 4.24. For Li_3ScN, this can be rationalized by the finding that a four fold coordination of scandium is normally not preferred.[164] In the end, these four compounds fail our defect chemistry screening, since we are not able to find any suitable dopants: In LiMgN, we are facing the problem of high formation energies for the dopant defects; In $ZnGeN_2$ and in Li_3ScN, we see Fermi pinning due to the mentioned antisite defect and in addition a lithium interstitial defect is also pinning our dopants in case of Li_3ScN; Although we identify magnesium and zinc as possible dopants for Li_3GaN_2, the dopants tend to occupy gallium and lithium sites owing to the comparable size of both elements leading to Fermi pinning due to self-compensation.

The ionic radii of the cations in $BaSiN_2$, $CaGeN_2$, $Ca_5(SiN_3)_2$ and $Ca_3(GaN_2)_2$ do not match and therefore we do not expect issues with the antisite defect, which is confirmed by our calculations. The calcium-containing compounds suffer more from the nitrogen-vacancy defect and should be synthesized under N-rich conditions. Although $CaGeN_2$ and $Ca_3(GaN_2)_2$ have no hole killer defects, we are not able to find any suitable dopant due to Fermi pinning caused by the N-vacancy. The same vacancy in $Ca_5(SiN_3)_2$ is acting as a hole killer in nitrogen-poor regions, but its formation energy can be raised quite well in N-rich regions. Therefore, we identify lithium in the position of calcium as p-dopant candidate, but this does not work in the end due to a lithium interstitial defect. Finally, several possible dopants under N-rich conditions for the remaining $BaSiN_2$, see Fig. 4.24 are identified: Na, K, Rb in position of Ba and Al in position of Si.

In case of $MgBe_2N_2$ and $CaMg_2N_2$, we only need to take care of the N-vacancy, as the metal antisite defects are neutral because of equally charged cations. In $CaMg_2N_2$, we need to apply N-rich conditions in order to avoid hole killing defects and to make Li

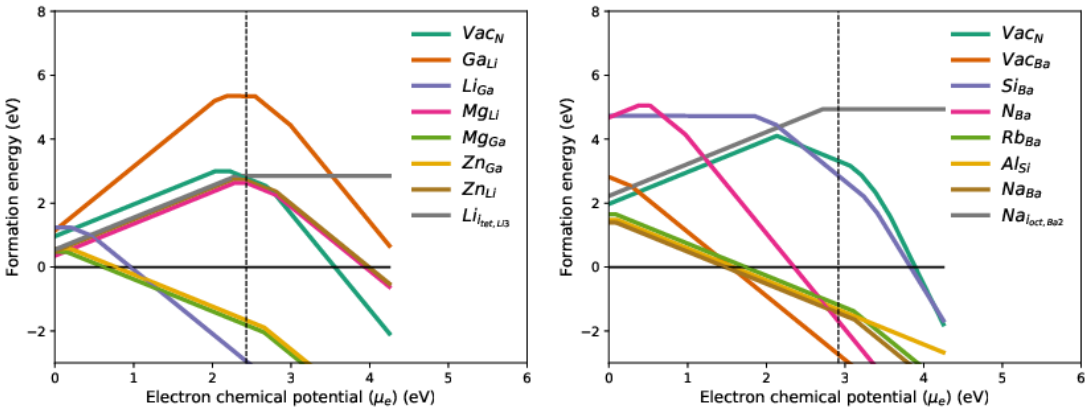

Figure 4.24: Left: Defect chemistry of Li_3GaN_2 under N-rich and Ga-poor conditions. Magnesium and zinc are Fermi pinned due to their antisite defect and lithium interstitial. Right: Defect chemistry of $BaSiN_2$ under N-rich conditions. The barium vacancy is Fermi pinned but aluminum, sodium, potassium (not shown) and rubidium are possible p-dopants.

Table 4.13: List of cyanamide candidates sorted by their HSE-band gaps. For each compound, its MPDB ID, symmetry, HSE-band gap (E_g^{HSE}), harmonic mean hole effective mass ($\overline{m}_h^*$) and relative shift of the CBM are given.

Compound	MPDB ID	Space group	E_g^{HSE} (eV)	$\overline{m}_h^*$ (m_e)	shift CBM
$BeCN_2$	mp-15703	$I\bar{4}2d$	5.19	0.76	34.5%
$MgCN_2$	mp-9166	$R\bar{3}m$	5.13	1.59	49.9%
Li_2CN_2	mp-9610	I4/mmm	4.88	1.34	37.2%
$CaCN_2$	mp-4124	$R\bar{3}m$	4.77	1.04	45.3%

in position of Mg function as possible p-dopant. $MgBe_2N_2$, see Fig. 4.25, shows no hole killing defects in all regions, but N-rich conditions are helping to avoid Fermi pinning of the possible p-dopants sodium in position of Mg and lithium in position of Mg and Be.

Cyanamides and beryllium carbonitride

Cyanamides MCN_2 with M = Ca, Li_2 and Mg should not suffer from antisite defects due to the covalently bound CN_2 group. We have also to remark that we added $MgCN_2$ to the list in Tab. 4.13, which exhibits a too high harmonic average of the hole effective mass of 1.59 m_e being above the screening criterion. However, it is interesting to compare $MgCN_2$ with $CaCN_2$ due to their similarity. The effective mass and HSE-band gap behave against the expected trend, because the less electronegative element Ca should have the larger band gap and larger effective mass. Beryllium carbonitride $BeCN_2$ is another story. We can not count this component to the cyanamides and therefore, expect

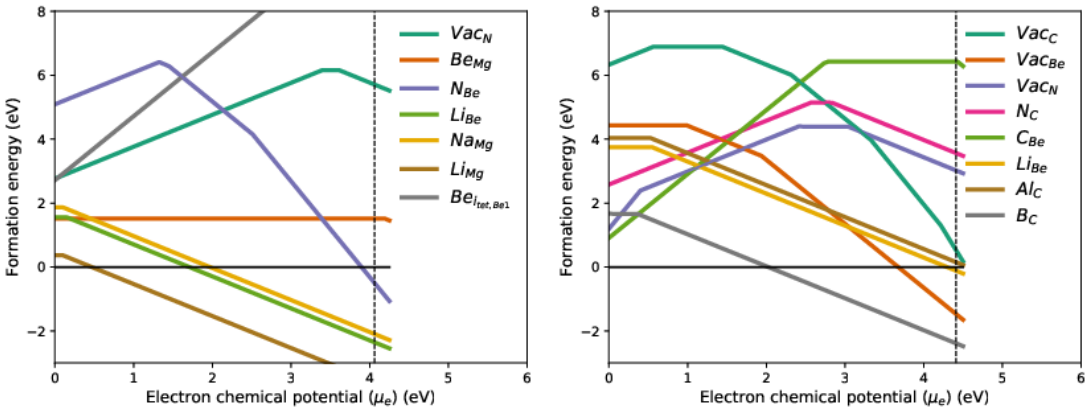

Figure 4.25: Left: Defect chemistry of $MgBe_2N_2$ under N-rich conditions. Lithium and sodium are possible p-dopants due to a neutral antisite defect. Right: Defect chemistry of $BeCN_2$ under N-rich conditions. The only promising p-dopant boron is Fermi pinned by the antisite and N-vacany defect.

quite different results. Owing to the small ionic radii of both beryllium and carbon, this compound faces the problem of antisite defects. As shown in Fig. 4.25, carbon in the position of beryllium is problematic for hole doping. No hole killing defects in any region are found, but we are also unable to identify a suitable dopant due to the high formation energies for lithium and other dopants and due to Fermi pinning for boron in the position of beryllium.

For the other cations, *i.e.* M = Mg, Li_2, and Ca, in the MCN_2 materials, we observe a mismatch between the radii. Based on the reasoning above, we do not expect cation antisite defects to be an issue and in fact the defect chemistry of these three materials is quite similar. All of them are barely passing our intrinsic defect screening and both anion vacancies are potential hole killer. Therefore, they need to be synthesized under C- and N-rich conditions. In this region, we see another defect gaining importance: nitrogen in the position of carbon. This leaves not much room for dopants and owing to this, Li_2CN_2 is already out of consideration, since we would have to substitute lithium with an element with even fewer valence electrons. For $CaCN_2$ and $MgCN_2$, we could for example dope them with lithium in the position of calcium or magnesium. Nonetheless, we encounter Fermi pinning. So these compounds only barely pass our intrinsic screening and in the end they fail our extrinsic screening.

Nitridophosphates

The nitridophosphates $LiPN_2$, Ca_2PN_3 and Mg_2PN_3 listed in Tab. 4.14 are performing quite well in our defect chemistry screening. The Li interstitial in $LiPN_2$ is quite bothersome and in combination with the N-vacancy this leads to the requirement of N-rich and Li-poor conditions for synthesis. It would also be good to have P-poor conditions, since we had to identify a suitable p-dopant for phosphorous. However, no suitable dopant

Table 4.14: List of nitridophosphate candidates sorted by their HSE-band gaps. For each compound, its MPDB ID, symmetry, HSE-band gap (E_g^{HSE}), harmonic mean hole effective mass ($\overline{m}_h^*$) and relative shift of the CBM are given.

Compound	MPDB ID	Space group	E_g^{HSE} (eV)	$\overline{m}_h^*$ (m_e)	shift CBM
$LiPN_2$	mp-3524	$I\bar{4}2d$	5.13	1.37	35.8%
Mg_2PN_3	mp-3933	$Cmc2_1$	4.88	1.29	46.1%
Ca_2PN_3	mp-8977	Cmce	3.87	0.87	47.3%

Table 4.15: List of chalcophosphate candidates sorted by their HSE-band gaps. For each compound, its MPDB ID, symmetry, HSE-band gap (E_g^{HSE}), harmonic mean hole effective mass ($\overline{m}_h^*$) and relative shift of the CBM are given.

Compound	MPDB ID	Space group	E_g^{HSE} (eV)	$\overline{m}_h^*$ (m_e)	shift CBM
$SbPO_4$	mp-3439	$P2_1/m$	5.34	1.27	51.2%
$BiPO_4$	mp-55879	$P2_1/m$	5.00	0.92	48.7%
$Mn_2P_2O_7$	mp-18721	C2/m	4.56	1.43	47.7%
$MgPS_3$	mp-675651	C2/m	3.90	1.13	48.6%
$InPS_4$	mp-20790	$I\bar{4}$	3.40	1.15	50.4%
$NaPS_4$	mp-28782	$P\bar{4}2_1/c$	3.39	1.47	44.8%
$MgPSe_3$	mp-28395	$R\bar{3}$	2.98	0.94	49.2%

is found, as the high formation energy of dopants and the Li interstitial easily lead to Fermi pinning. In Mg_2PN_3, shown in Fig. 4.26, the antisite defect of P in position of Mg is problematic, as this also becomes a hole killing defect in a phosphorous-rich region. Therefore, synthesizing it under P-poor and N-rich conditions seems to be a good strategy. This also makes the substitution of phosphorous attractive and indeed Si, Ge and Ti in position of P are found in our dopant screening. However, the screening fails to identify a p-dopant for magnesium, even though Li in position of Mg appears to be promising, but it gets Fermi pinned by its interstitial defect. The last nitridophosphate is Ca_2PN_3, where we find that the vacancy of nitrogen is problematic and even hole killing in N-poor regions implying N-rich conditions. We are unable to find a suitable dopant for calcium, but we identify Si in position of P as promising dopant. Compared to Mg_2PN_3, the defect chemistry in Ca_2PN_3 is less favorable and therefore, Ge in position of P is getting Fermi pinned, although this is a close call, because it is very close to the valence band.

Phosphates and chalcophosphates

As mentioned in subsection 4.4.1, only phosphorous-containing compounds composed of another anion are selected based on our screening criteria, see Tab. 4.15. We can

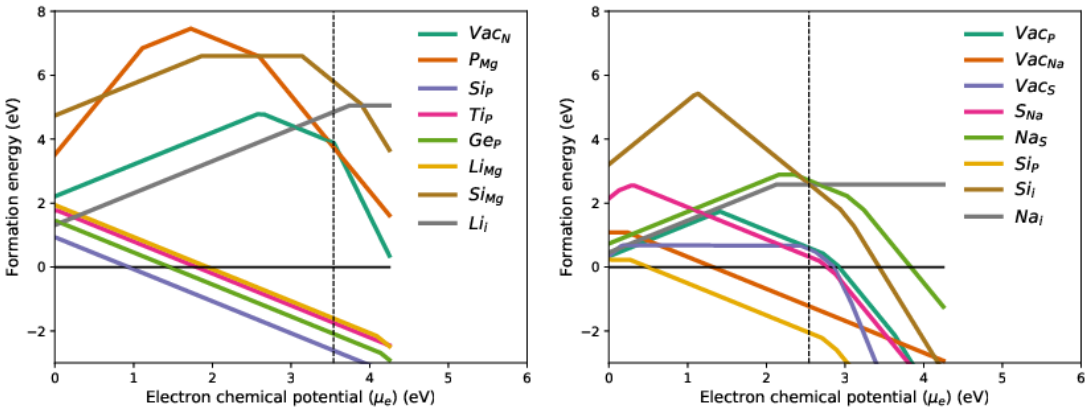

Figure 4.26: Left: Defect chemistry of Mg_2PN_3 under N-rich conditions. Although lithium is getting Fermi pinned, silicon, germanium and titanium on P are possible p-dopants . Right: Defect chemistry of Na_3PS_4 under P-poor and S-rich conditions. By adjusting the conditions, the vacancy can be utilized.

further classify them as either chalcogen- or nitride-containing. We will start with the chalcogen-containing phosphates, due to their high failure rate during the intrinsic defect screening. The phoshphates $BiPO_4$ and $SbPO_4$ as well as the thiophosphates $InPS_4$ and $MgPS_3$, exhibit hole killer defects in all regions and therefore fail the intrinsic screening. The hole killing defects in these compounds are anion-vacancies with the exception of $MgPS_3$, where the hole killing defect is the Mg interstitial defect in most of the regions. Interestingly, the vacancy of phosphorous is an issue in $BiPO_4$, whereas it does not cause any problems for $SbPO_4$ in all regions.

This leaves $Mn_2P_2O_7$, $MgPSe_3$ and Na_3PS_4 as possible p-type semiconductors. In comparison to other compounds, the defect formation energies in $MgPSe_3$ are quite high resulting in no hole killer defects in all regions and a promising situation for dopant screening. However, no possible dopant is identified, since the tested ones exhibit high formation energies. The intrinsic defects of Na_3PS_4 are not very promising and we have to avoid S-poor conditions, since the S vacancy and Na in position of S are hole killing defects in these regions. By applying P-poor and S-rich conditions during synthesis, silicon can be used as dopant in position of phosphorous. We should also mention that this material can be made intrinsic p-type under S-rich and Na-poor conditions, but then the dopant, Si in position of P, will get Fermi pinned. Under the first mentioned conditions and as shown in Fig. 4.26, we observe Fermi pinning for the vacancy. Because of the two situations it is unlikely that both defects can be used in order to create high hole concentrations. And one has to choose between intrinsic or extrinsic doping for Na_3PS_4.

We expect extrinsic doping to be superior. The pyrophosphate $Mn_2P_2O_7$ is passing the intrinsic defect screening and exhibiting promising defect chemistry. This is due to the behavior of the vacancies of oxygen and phosphorous, which have high formation energies and do not release electrons easily. The formation of a phosphorous or manganese

antisite defect under phosphorous-rich conditions can even be harmful for the dopants suggesting oxygen-rich or neutral conditions. Under these conditions, we identify quite a lot of dopant candidates. According to our calculations, $Mn_2P_2O_7$ can be doped p-type with hydrogen, lithium, sodium, potassium, rubidium and silver on manganese sites and carbon, silicon and germanium on phosphorous sites.

The failure of p-type doping in oxides is often caused by the formation of oxygen vacancies. In comparison with the other investigated materials, we observe higher formation energies for the corresponding vacancies, so they are less prone to the formation of hole killer defects. Indeed, most of the investigated compounds pass this criterion. On the other hand, this means also that we have to consider hole killing defects such as antisite defects of elements with more valence electrons replacing elements with fewer valence electrons and metal interstitial defects. To sum up the results of our defect chemistry screening, finding a suitable dopant turns out to be the major challenge for the investigated ternary compounds. Dopants for compounds that exhibit promising intrinsic defect chemistry are also often suffering from high formation energies, so that we often encounter Fermi pinning. From the 21 ternary compounds passing the intrinsic defect chemistry screening, we end up with only 6 compounds, for which we propose suitable dopants. As shown in our investigations, it makes sense to follow the rule of avoiding nitrides containing metals in unequal charge states and with similar ionic radii altogether, as it is highly likely that these compounds exhibit either hole killing defects or Fermi pinning of dopants.

The branch point concept might also be employed in order to predict the defect chemistry. Samardian *et. al.*[98] used the branch point energy in order to classify oxides into 3 classes. By applying this concept to our calculated branch point energies, we would expect $ZnGeN_2$ to be n-type, whereas the rest of the compounds falls into the intermediate class, for which both p- and n-type behavior is possible. However, it is more likely to encounter n-type behavior, since most of these compounds exhibit a greater shift of the VBM. Therefore, we find this concept not trustworthy when it comes to nitrogen- and phosphorous-containing materials.

4.4.3 Discussion

Literature survey

a) Atomic structure and stability: For stability, we have to consider at least two aspects: Transformation due to change in temperature or pressure and stability with regard to reactions that can occur due to contact to air, moisture, acids or bases. Combining these two aspects, there is also the possibility of decomposition due to heating. We used the convex hull data provided by the MPDB in order to judge the stability. This should in principle be fine for phase transformations and decomposition, but stability towards air, moisture, acids and bases is not considered. Furthermore, the choice of the PBE functional might be a possible source of error, as it might overestimate covalent bonds.[165,166] Therefore, employing PBE to construct a phase diagram can lead to predictions violating the octet rule. As mentioned in the binary section, KP is fulfilling

our stability criterion ($E_{above\,hull} = 0\,\mathrm{eV}$), but experimentally it is only stable when it is synthesized in an ampule using stoichiometric amounts of starting material and inert gas during processing.[83] Owing to this, we discuss the stability of the identified compounds based on a literature search.

Sensitivity to moisture and air were reported for $Mg(BeN)_2$,[167] Na_3PS_4,[168] $BaSiN_2$,[169] and $CaMg_2N_2$.[170] In the study of $BaSiN_2$,[169] the statement about stability is referring to all the used compounds, so $BaSiN_2$ has not been specifically investigated and could also be stable. A similar composition, $Ba_2Si_5N_8$, has also been tested in 2008 for application in light-emitting diodes.[171] Na_3PS_4 is considered for utilization as electrolyte in sodium batteries.[172,173] This shows that the mentioned materials can be used for technological applications, although they are sensitive to air. In addition, $Ca(MgN)_2$ is reported to be soluble in dilute sulfuric acid.[174] Furthermore, Ca_2PN_3 is found to be more sensitive to hydrolysis than Mg_2PN_3, which is not attacked by air, moisture, acids and bases under normal conditions.[175] This could mean that these compounds will degrade more facile than others. For the rest of the suggested compounds, no further information on their stability is given in the literature.

Si_3N_4 is known to exist in two phases: the low temperature phase $\alpha-Si_3N_4$ (P31c) and the high temperature phase $\beta-Si_3N_4$ ($P6_3/m$). $\alpha-Si_3N_4$ is a metastable configuration, so it can be transformed into $\beta-Si_3N_4$, whereas the reverse transformation is not possible. We also find two different space groups for $\beta-Si_3N_4$: $P6_3/m$[176] and $P6_3$.[177] Based on our stability criterion, we selected $\beta-Si_3N_4$ with $P6_3/m$ space group in agreement with Belkada *et al.*[176]

As discussed in Ref. 178, there was dispute in the phase diagram for BN. It was not clear if cubic boron nitride (c−BN, $F\bar{4}3m$) or hexagonal boron nitride (h−BN, $P6_3/mmc$) is the preferred structure at 0 K and 0 pressure. However, we propose h−BN based on our stability criterion. The most stable atomic structure for AlN in the MPDB is the wurtzite one ($P6_3/mc$), which is consistent with previous results.[179,180] P_3N_5 exhibits several phases, which are labeled as $\alpha-P_3N_5$ (C2/c), $\gamma-P_3N_5$ (Imm2) and $\delta-P_3N_5$ ($P112_1/m$).[181] $\delta-P_3N_5$ is a high pressure phase and not included in the MPDB. From the remaining two phases, $\alpha-P_3N_5$ is correctly identified to be more stable. For B_6P as well as for most ternaries, the MPDB contains just one structure, which match the experimental ones, as they are are derived from experimental data. The only ternary compounds, for which several phases are available in the MPDB, are $Mn_2P_2O_7$ and Na_3PS_4. From the three theoretical phases of $Mn_2P_2O_7$, the thortveitite-structure (C2/m) is only slightly more stable (0.001 eV) than the other two and therefore reported in the literature.[182] For Na_3PS_4, two phases are known experimentally and theoretically: $\alpha-Na_3PS_4$ ($P\bar{4}2_1/c$)[168] and $\beta-Na_3PS_4$ ($I\bar{4}3m$).[183] In the MPDB, the $\alpha-$phase is correctly identified to be more stable than the $\beta-$phase.

b) Band gap and transparency: We considered the size of the band gap as the criterion determining the transparency of compounds. It should be mentioned that we did not investigate the reflectance of the materials. For example, ceramics made of AlN, BN and Si_3N_4 are all reflective and therefore their color is white or gray. We note in passing that there are some efforts to increase the translucency of Si_3N_4.[184]

HSE band gap calculations show that this functional underestimates band gaps larger

than 5 eV.[57] This is true for P_3N_5, where we calculated a band gap of 4.99 eV and experimental results indicate a band gap of 5.87 ±0.2 eV.[119] It also holds for AlN (5.42 eV calculated compared to 6.2 eV experimentally) and BN (5.41 eV calculated compared to 6.0 eV experimentally).[116,185] In contrast to this, the agreement between a previously calculated band gap for AlN of 5.48 eV and our result of 5.42 eV is still good.[57] Overall, this underestimation is not of great importance to our screening strategy, since only gaps greater than 5 eV are afffected and we should probably stop screening materials with band gaps greater than 4.5 eV.

Considering the other wide-band gap compound, $\beta-Si_3N_4$, its gap is overestimated by 0.2 eV, as we calculated 5.7 eV compared to 5.5 eV measured by Carson *et al.*[186] Although the authors admit that this value is probably too large and the value of 5.2 eV measured by Goodman[120] is more realistic. It is also important to point out that the band gap of this material is very sensitive to the doping level.[187] As expected, B_6P with a calculated gap of 3.23 eV is in better agreement with the optically measured value of 3.35 eV[117] due to the small gap.

For our passing ternaries, we found five reported values in the literature. For $Mg(BeN)_2$, a gap of 6.1 eV was calculated by Khan *et al.*[188] using the modified Becke-Johnson functional.[189] This functional was designed for the calculation of band gaps and should be also accurate for values larger than 5.0 eV. Therefore, its result can be expected to be more accurate than the 5.36 eV calculated in this work. Our calculated gaps for Mg_2PN_3 with 4.88 eV and for $BaSiN_2$ with 3.99 eV are in good agreement with the measured gaps of 5.0 eV[190] and 4.1 eV,[191] respectively. A calculated band gap for Na_3PS_4 of 3.26 eV is reported by Kang *et al.*[192] using the screened exchange local density approximation (sX-LDA) as functional.[193,194] This value is slightly lower than from our HSE calculation with 3.39 eV and the results are therefore in reasonable agreement. For $CaMg_2N_2$, we obtain a band gap of 3.05 eV, which is not too far away from the 3.25 eV measured by diffuse IR reflectance spectroscopy.[195] To the best of our knowledge, no band gaps have been reported for $CaPN_3$ and $Mn_2P_2O_7$ so far.

c) Effective mass and conductivity: The effective masses can theoretically be calculated in two ways: calculating the curvature of a specific path in the reciprocal space or with Boltzmann transport theory. We obtained the effective mass values from Boltzmann transport theory *via* the dryad database, so they do not directly correspond to a certain curvature. Owing to this, the effective masses from Boltzmann transport theory for AlN, BN and Si_3N_4 are often between the mass of the lightest and the heaviest hole from curve fitting. However, one exception is BN, for which 0.33 and 1.26 m_e are reported as light and heavy hole effective masses, respectively,[196] but 0.7 and 3.31 m_e are computed with Boltzmann transport theory. For AlN, 0.36 and 4.24 m_e are found experimentally,[196] but 0.25 and 3.68 m_e were calculated for light and heavy hole effective masses, respectively.[197] This can be compared to the values of 0.43 and 3.58 m_e from Boltzmann transport theory. For Si_3N_4, 0.85 and 2.9 m_e are found in a computational study[198] as light and heavy hole effective masses, respectively, while 0.94, and 1.95 m_e is obtained from Boltzmann transport theory.

d) Dopants We identified Mg and Zn in the position of Al as possible p-dopants for AlN. Be was discarded, because of an interstitial defect compensating the hole doping.

This is in good agreement with recent calculations, as Zhang *et al.*[199] investigated p-type doping with Be, Mg and Ca and their reported defect chemistry is quite similar to our results. As mentioned in the defect chemistry section 3.6, activation energies are not accurate on the GGA level of theory. Therefore, one larger difference is found for the activation energy of Mg, which Zhang *et al.*[199] found to be 0.58 eV. This is also confirmed by Wu *et al.*,[200] who argued that an activation energy higher than 0.5 eV will lead to a carrier concentration that is too small. In our calculations, the activation energy of Mg is underestimated with about 0.3 eV, which might lead to the impression that Be performs worse than Mg as a dopant. Contrary to this, Wu *et al.*[200] found that Mg is unsuitable as dopant, whereas Be is suitable when it is co-doped with H. Another study came to the conclusion that doping with C might be working when co-doped with O.[201] However, we did not investigate more complex doping strategies, so that some of the dopants found unsuitable in our investigations could be working when co-doped or deployed in a more advanced doping scheme.

We also did not look into the possibility of electrochemical doping, which is for example employed for CuI with iodine. For BN, we encounter a similar problem by dismissing Mg in position of B because of the high formation energy. This results in Fermi pinning, although the epitaxial grown Mg-doped, p-type h−BN-layer was reported.[202,203] The experimental doping was realized with biscyclopentadienyl-magnesium, so that the failure of our calculations might be explainable with the simple single point defect model. Lu *et al.*[187] calculated properties of Ca and Al doped $\beta-Si_3N_4$. They reached the conclusion that the Al defect is more stable, which is in agreement with our calculations, where we see that the Al defect will form more easily and that the Ca defect is compensated by the higher formation energy.

In the end, the effective mass is used as an indicator for good hole conductivity. From this perspective, known properties of some materials can also be compared with the reported effective masses. Good hole conduction in ($700\,cm^2V^{-1}s^{-1}$) B_6P-thin films was reported in ref. 204. Na_3PS_4 is known as ion-conductor and therefore hole or electron transport is not the main source of its conductivity.[168,172] Thin films of P_3N_5 are used as an insulating layer.[205] Finally, the effective mass criterion can be relaxed even more since common p-type semiconductors exhibit effective masses of at least $2.0\,m_e$.[86]

4.4.4 Final remarks

The final list of promising binary and ternary pnictides is shown in Tab. 4.16. The p-type applicability of B_6P is not surprising, since BP and B_6O are already known as p-type semiconductors.[162,206] The more surprising aspect of this compound is the worsening of the band alignment, as the CBM is shifted by about 85 % in BP. In contrast to this, we only find a shift of 50 % for B_6P. This means that most of the 1.2 eV difference between the two gaps is caused by the shift of the VBM, which is disadvantageous for p-type applications.

Although the relative shift of 51 % is one of the better values among the remaining compounds, the large band gap of 5 eV for P_3N_5 is a hindrance for some p-type applications. Such a large band gap would be even more problematic, when it is combined with

Table 4.16: Final list of binary and ternary compounds. For each compound the HSE- (E_g^{HSE}) and experimental band gaps E_g^{exp}, harmonic mean hole effective mass ($\overline{m}_h^*$), relative shift of the CBM, and suggested dopants are given.

Compound	E_g^{HSE} (eV)	E_g^{exp} (eV)	$\overline{m}_h^*$ (m_e)	CBM shift	Dopants
Si_3N_4	5.71	5.2-5.5	1.13	50.4%	Si: Ga, Al
AlN	5.42	6.2	1.03	42.7%	Al: Mg, Zn
B_6P	3.23	3.35	0.84	48.9%	P: Ge
P_3N_5	4.97	5.87 ± 0.2	1.08	50.4%	P: Si
$MgBe_2N_2$	5.36	-	1.33	48.9%	Mg: Li, Na Be: Li
Mg_2PN_3	4.88	5.0	1.29	46.1%	P: Si, Ge, Ti
$Mn_2P_2O_7$	4.56	-	1.43	47.7%	Mn: Ag, K, Li, H, Rb, Na P: Si, C, Ge
$BaSiN_2$	3.99	4.1	0.90	52.4%	Ba: Na, K, Rb Si: Al
Ca_2PN_3	3.87	-	0.87	47.3%	P: Si, Ge
Na_3PS_4	3.39	-	1.47	44.8%	P: Si
$CaMg_2N_2$	3.05	3.25	1.36	36.2%	Mg: Li

a small relative shift of the CBM. We encounter exactly this problem in the 7 remaining ternary compounds. In particular, the magnesium-containing materials $MgBe_2N_2$ and Mg_2PN_3 are suffering from these two factors and the VBM is shifted down by 2.7 and 2.6 eV, respectively. $MgBe_2N_2$ is also sensitive to moisture and air, which makes this compound quite uninteresting for application.[167] Contrary to this, Mg_2PN_3 is still of interest, since its defect chemistry is indicating various possible dopants. Furthermore and as mentioned above, this compound seems to be fairly stable, as it is neither attacked by air, moisture, acids nor bases under normal conditions.[175]

Na_3PS_4, which exhibits the second lowest shift of the conduction band (-1.9 eV), could be problematic because of its good ion conduction properties.[173] Nevertheless, it seems to be quite interesting from a defect chemistry point of view: We found one region, where it can be doped by silicon in the position of phosphorous, and another region, where the sodium vacancy is making it p-type. In contrast to this, Li_3GaN_2, which is known as an ionic conductor,[207] failed in our dopant screening due to self-compensation.

Among the ternary compounds, $Ca_5Si_2N_6$ exhibits with -1.7 eV the lowest shift of the VBM, but its defect chemistry appears unfavorable due to Fermi pinning near the valence band. We believe that this material is uninteresting for application, due to the fact that it is highly air sensitive[208] and the fact that we were not able to find any suitable dopant.

As mentioned before, $CaMg_2N_2$ and Ca_2PN_3 appear to be a bit more stable. For both compounds, we find nitrogen-rich conditions to be necessary in order to avoid hole killing defects. $CaMg_2N$ can be doped p-type with lithium in the position of magnesium and Ca_2PN_3 with silicon in the position of phosphorous. We also want to point out, that Ca_2PN_3 exhibits the lowest effective mass among the ternary compounds and is

therefore promising in terms of hole conduction.

Although the defect chemistry of $Mn_2P_2O_7$ is very promising, we are not sure if this material is described properly in our defect calculations. They are based on single point defects, *i.e.* on removing a single atom. A chemist would probably expect a vacancy including PO_3^{2-}, PO_4^{2-} or $P_2O_7^{4-}$. We suspect this material to be insulating, because we did not find any indication that $Mn_2P_2O_7$ can be used as a semiconductor.[209]

Based on our screening, $BaSiN_2$ appears to be the most promising material. Among the ternary compounds, its effective mass of $0.91\,m_e$ is the second lowest, the valence band is shifted by $-1.9\,eV$, which is the third lowest value, and its defect chemistry is also promising, since only one region is critical regarding hole killing defects. We were also able to identify several dopants that make this material p-type and especially rubidium in the position of barium seems to be interesting. As mentioned in the stability discussion, a related material was also tested in 2008 for use in light-emitting diodes. For this purpose, $Ba_2Si_5N_8$ was doped with europium.[210] Nevertheless, it has to be stressed that the formed structures and properties depend on the method of synthesis and further conditions. Therefore, this study might serve as a starting point for further investigations of the promising compounds.

4.5 Chalcogenide studies

The chalcogenide studies were carried out by Dr. Ramya.[53,211] In the binary chalcogenide study, the original methodology as described in section 3.1.4 was used,[53] whereas the ternary chalcogenide study included some changes in the methodology and their implementation.[211] The data source and the employed screening criteria in the binary study deviate from the later studies, thus we decided to realize a comparison by applying the new criteria to the results of the binary study. In addition and after the summary of the ternary screening, we discuss the defect chemistry in more detail.

4.5.1 Binaries

The binary chalcogenide screening[53] is based on the work of Strehlow *et al.*[54] It should be mentioned that a relaxed band gap criterion was employed, as the experimental gap had to be greater than 1.7 eV. This led to the identification of less than 40 possible candidates. The effective mass was calculated *via* finite differences[55] and the smallest eigenvalue is reported. This criterion reduced the candidates to 22 materials, for which defects had to be calculated. After the defect chemistry screening, nine compounds appeared as promising materials.

For later studies we used the database of Ricci *et al.*[62] and considered the harmonic average of the eigenvalues for the effective mass. Owing to this, we show in Tab. 4.17 both mentioned values of the effective mass for the nine final candidates. In case of the isotropic materials ZnS, ZnSe, ZnTe and MgS, the agreement is reasonable. One exception is BeTe, for which we did not find a value in the database. MgTe exhibits a particular big discrepancy between its effective mass values. This could be caused by its highest lying valence bands, which are degenerate at the Γ-point, see Fig. 4.27.

Table 4.17: Final list of binary chalcogenides passing the screening sorted as discussed in ref. 53. For each compound, the MPDB ID, symmetry, HSE-band gap (E_g^{HSE}), experimental band gap (E_g^{exp}), hole effective mass (m_h^*) (smallest eigenvalue from finite differences[55]) and harmonic mean hole effective mass ($\overline{m}_h^*$) (from Boltzmann-transport theory[62]) are given.

Compound	MPDB ID	Space group	E_g^{HSE} (eV)	E_g^{exp} (eV)	m_h^* (m_e)	$\overline{m}_h^*$ (m_e)
ZnS	mp-10695	$F\bar{4}3m$	3.5	3.7	0.70	0.81
ZnSe	mp-1190	$F\bar{4}3m$	2.7	2.7	0.63	0.72
ZnTe	mp-2176	$F\bar{4}3m$	2.6	2.4	0.40	0.55
MgS	mp-1315	$Fm\bar{3}m$	5.5	6.4	0.96	0.98
MgTe	mp-1039	$P6_3mc$	4.2	4.7	0.18	1.56
GaSe	mp-1943	$P6_3/mmc$	2.6	2.1	0.25	0.77
GaTe	mp-10009	$P6_3/mmc$	1.7	1.7	0.14	0.55
Al_2Se_3	mp-11674	$P6_3/mmc$	3.1	3.1	0.56	1.42
BeTe	mp-252	$F\bar{4}3m$	2.6	2.9	0.35	n.a.

Therefore, the hole effective mass calculation might be using the higher curvature to determine the effective mass.

Application of our recent criteria would eliminate most of the listed materials. The band gap ($\geq 3.0\,eV$) criterion would exclude more than half of the compounds. For the effective mass, based on database values, we would kill MgTe and maybe also Al_2Se_3 depending on if we require the harmonic average of the hole effective mass to be smaller than 1 or $1.5\,m_e$. So only two compounds would remain: ZnS and MgS. The experimental band gap of the latter is fairly large with 6.4 eV indicating insulating behavior. Therefore, it needs to be tested if this compound is still semiconducting.

4.5.2 Ternaries

The ternary chalcogenide screening[211] is based on the new methodology, which is similar to the methodology used for pnictide and halide screening. We searched in the Materials Project Database[63] for candidates and employed the dryad database of Ricci *et al.*[62] in order to find the hole effective masses. Afterwards, the HSE-band gap was calculated. After screening of the defect chemistry, the optical spectra and the band alignment were also calculated. For the latter, the branch point method[91] was employed, which was later on included in the HSE-screening. This allowed us later to test the classification scheme of Sarmardian *et al.*[97] and to point out interesting materials, for which defect chemistries were not studied because of their HSE-band gap being too small.

The criteria used in this screening were strict. For the database search, the elements were limited so that only specific metal-metal-chalcogenides would be further considered. The harmonic average of the hole effective mass had to be smaller than or equal to $1.0\,m_e$ and the HSE-band gap had to lie between 3.0 and 4.3 eV. This resulted in 34 candidates that are listed in Tab. 4.18, for which the intrinsic defect chemistry was screened.

Table 4.18: List of ternary chalcogenides after screening with criteria for hole effective mass and HSE band gap sorted by their harmonic average value of the hole effective mass. For each compound, the MPDB ID, symmetry, HSE-band gap (E_g^{HSE}), eigenvalues of the hole effective mass and harmonic mean of the hole effective mass are given.

Compound	MPDB ID	Space group	E_g^{HSE} (eV)	m_h^*1 (m_e)	m_h^*2 (m_e)	m_h^*3 (m_e)	$\overline{m}_h^*$ (m_e)
$NaBiS_2$	mp-675531	Fdd2	3.0	0.20	0.25	2.14	0.31
$AlTlSe_2$	mp-863762	C2/c	3.35	0.18	0.86	0.88	0.38
IrSbS	mp-8630	$P2_13$	3.08	0.39	0.39	0.39	0.39
$TlInS_2$	mp-865274	C2/c	3.00	0.21	0.72	0.75	0.40
$TlGaS_2$	mp-4016	C2/c	3.39	0.22	0.86	0.87	0.44
Na_5InTe_4	mp-28597	Pbcn	3.00	0.23	1.54	1.55	0.53
Ba_2GeSe_4	mp-11902	$P2_1/m$	3.00	0.22	3.87	7.75	0.60
$NaInSe_2$	mp-22473	$R\bar{3}m$	3.11	0.48	0.48	4.91	0.60
$RbAu_3Se_2$	mp-9385	$P\bar{3}m1$	3.18	0.49	0.49	1.58	0.63
Al_2ZnS_4	mp-4842	$Fd\bar{3}m$	3.95	0.66	0.66	0.66	0.66
$LiAlTe_2$	mp-4586	$I\bar{4}2d$	3.60	0.52	0.83	0.83	0.69
Tl_3BS_3	mp-29337	$P2_12/m$	3.00	0.43	0.65	2.23	0.69
$Ga_2Sn_2S_5$	mp-14280	$Pna2_1$	3.00	0.43	0.65	2.23	0.70
Ba_2SiSe_4	mp-14447	$P2_1/m$	3.95	0.26	7.80	10.34	0.74
$Ba(BSe_3)_2$	mp-570823	Cmce	3.53	0.51	0.85	1.38	0.77
Na_2GeSe_3	mp-4068	$P2_1/c$	3.12	0.38	1.02	4.83	0.79
Ag_3AuS_2	mp-34460	$R\bar{3}m$	3.03	0.40	1.59	1.59	0.80
$NbCu_3Se_4$	mp-5621	$P\bar{4}3m$	3.13	0.82	0.82	0.82	0.82
Na_2ZrSe_3	mp-7219	C2/m	4.32	0.50	0.71	4.73	0.83
VCu_3S_4	mp-3762	$P\bar{4}3m$	3.69	0.93	0.93	0.93	0.93
$NaInS_2$	mp-20289	$R\bar{3}m$	3.90	0.67	0.67	5.98	0.94
$NbCu_3S_4$	mp-5621	$P\bar{4}3m$	3.40	0.97	0.97	0.97	0.97
Ba_2GeS_4	mp-540805	Pnma	4.13	0.38	3.86	5.74	0.97
NaLiTe	mp-8754	Pnma	3.73	0.49	1.50	2.96	0.98
Na_2GeS_3	mp-4068	$P2_1/c$	4.29	0.48	1.28	4.93	0.98
$Zn(GaSe_2)_2$	mp-15776	$I\bar{4}$	3.31	0.99	1.00	1.02	1.00
$LiGaSe_2$	mp-11582	$Pna2_1$	3.17	0.53	1.73	2.14	1.0
$CuBS_2$	mp-12954	$I\bar{4}2d$	3.15	0.93	1.07	1.07	1.0
Tl_2SiSe_3	mp-15776	$I\bar{4}$	3.02	0.57	1.16	4.02	1.0
$Ba(GaSe_2)_2$	mp-7841	Cccm	3.58	0.70	1.14	1.83	1.0
$Rb(SbSe_2)_2$	mp-9798	$P\bar{1}$	3.58	0.61	1.26	2.41	1.0
RbAuSe	mp-9731	Cmcm	3.39	0.56	1.13	5.66	1.0
KAuSe	mp-9881	Cmcm	3.42	0.54	1.23	5.48	1.0
Ba_2TiS_4	mp-17908	Cmcm	3.2	0.54	1.83	2.88	1.0

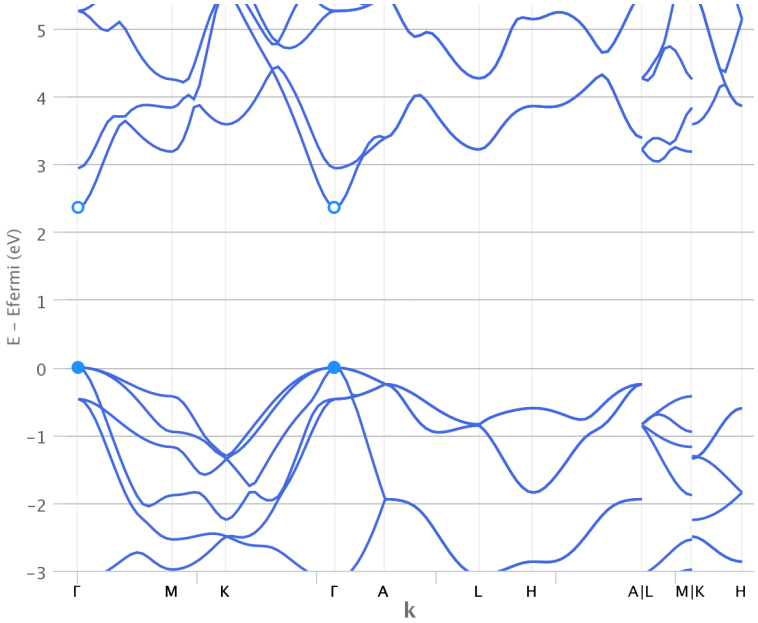

Figure 4.27: Band structure of MgTe adopted from the Materials Project Database.[63] The circles indicate the position of the Γ-point, where three valence bands are degenerate.

We can first have a look at the compounds containing tellurium. This element exhibits a similar electronegativity as phosphor and therefore probably suffers from similar problems: the band gaps of these materials could be too small to let them pass the PBE- and HSE-band gap screening steps. We only found $LiAlTe_2$, Na_5InTe_4 and NaLiTe as potential candidates. The lithium-containing materials exhibit HSE-band gaps of 3.60 ($LiAlTe_2$) and 3.73 eV (NaLiTe) and Na_5InTe_4 is barely passing the HSE-band gap criterion with 3.00 eV. Although we were not able to find any dopant for $LiAlTe_2$, Na_5InTe_4 and NaLiTe pass our intrinsic defect screening. In $LiAlTe_2$, the antisite defect of Li on Al is troublesome and in NaLiTe, the lithium interstitial might be problematic. In the case of the latter, it is hard to find a suitable dopant, since both of the metals are in oxidation state I.

The oxidation state is also important for the selenium-based materials, for which intrinsic defects are screened. The defect chemistry of most of these materials posses often no hole killing defects under anion-rich conditions. Therefore, only $NaInSe_2$, $Zn(GaSe_2)_2$, $LiGaSe_2$, and $Rb(SbSe_2)_2$ are failing the intrinsic defect chemistry screening. For the gallium-containing compounds, the antisite defects of Ga on Zn and Ga on Li turn out to be hole killing. In $NaInSe_2$, we have beside the antisite defect of In on Na also Se on Na, which releases electrons into the material.

In contrast to these three materials, Na_2ZrSe_3 is passing the intrinsic defect screening. But it is suffering under the antisite defect of Zr on Na, which prevents us from finding

any suitable dopant. In $Rb(SbSe_2)_2$, the hole killing defect is even just the interstitial defect of selenium, which is rather unusual for anion interstitials. However, we should not forget that selenium is also able to form compounds, where it is in an oxidation state of IV.[109] This explains the release of electrons under electron-poor conditions.

We encounter further selenium-related problems also in $AlTlSe_2$, Ba_2GeSe_4, Tl_2SiSe_3, $Ba(GaSe_2)_2$, and as mentioned in $Rb(SbSe_2)_2$. Except for both thallium-containing compounds, where this is the antisite defect, it is the selenium interstitial defect, which renders doping of these compounds hard. Nonetheless, we were able to find possible dopants for Ba_2GeSe_4 letting this compound as the only one from the above mentioned, pass the extrinic and therefore whole defect screening.

Furthermore, for Ba_2SiSe_4, $Ba(BSe_3)_2$ and Na_2GeSe_3, we see also Se-related problems, but they are not the main hindrance for p-type doping. In Na_2GeSe_3, the sodium interstitial is more troublesome than the antisite defect, so Sn on Na prevents us from finding any suitable dopant. Under electron-poor conditions, the vacancies of Si and B release electrons into the material in case of Ba_2SiSe_4 and $Ba(BSe_3)_2$, respectively. This unusual behavior of cation vacancies could also be related to selenium, because boron as well as silicon are surrounded by selenium in a tetrahedral fashion. The difference in electronegativity is also relatively small. Therefore, the classification of Se^{2-} and Si^{4+} might not be justified and we should more likely think in terms of ${SiSe_4}^{4-}$ and ${B_2Se_6}^{2-}$. We were able to find dopants for both compounds, so that both of them pass the defect screening.

Finally, we are left with the coinage metal- and selenium-containing materials. All these materials suffer from interstitial defects of coinage metals and are potentially intrinsic p-type, if the coinage metal vacancies are not pinned by an interstitial defect. This happened in $NbCu_3Se_4$, where the copper vacancy is pinned by a copper interstitial defect. This in combination with the inability to find any dopant led to the failing of the extrinsic defect screening for this compound. We were also not able to find any dopant for $RbAu_3Se_2$, RbAuSe, and KAuSe, but the vacancies of these materials render them intrinsic p-type. However, in the case of KAuSe it is the potassium vacancy, since the gold vacancy got pinned by its interstitial defect.

Even though the electronegativities of selenium and sulfur are similar and the number of candidates in both classes are nearly equal (16 selenides and 15 sulfides), a lot more sulfides are failing the intrinsic defect screening. In $NaBiS_2$, $NaInS_2$, and Ba_2TiS_4, sulfur-rich conditions were not sufficient to suppress the formation of sulfur vacancies, which act as hole killer in these compounds. The vacancy of sulfur is also problematic in Tl_3BS_3. However, it is not a hole killer letting this compound barely pass our intrinsic defect screening. In the end, it failed the dopant screening, since we were not able to find a suitable dopant. The antisite defect In on Na in $NaInS_2$ is even more troublesome than the vacancy due to the low formation energy of the former. $TlInS_2$, $TlGaS_2$, and Al_2ZnS_4 are not passing the intrinsic defect screening because of antisite defects. In the thallium-containing materials, it is the Tl on S antisite defect, which remains hole killing, although sulfur-rich conditions were applied. For Al_2ZnS_4, it is the Al on Zn antisite defect, which proves to be hole killing. $Ga_2Sn_2S_5$ and Na_2GeS_3 are also not passing our intrinsic defect screening. In these materials, the interstitial defects are responsible for

Table 4.19: Final list of ternary chalcogenides after defect chemistry screening. Top materials for which we found a dopant bottom intrinsic p-type materials without dopants. Sorted by their harmonic average value of the hole effective mass. For each compound, the MPDB ID, symmetry, HSE-band gap (E_g^{HSE}), eigenvalues of the hole effective mass, harmonic mean of the hole effective mass and are given.

Compound	MPDB ID	Space group	E_g^{HSE} (eV)	m_h^*1 (m_e)	m_h^*2 (m_e)	m_h^*3 (m_e)	$\overline{m}_h^*$ (m_e)
IrSbS	mp-8630	$P2_13$	3.08	0.39	0.39	0.39	0.39
Ba_2GeSe_4	mp-11902	$P2_1/m$	3.00	0.22	3.87	7.75	0.60
Ba_2SiSe_4	mp-14447	$P2_1/m$	3.95	0.26	7.80	10.34	0.74
$Ba(BSe_3)_2$	mp-570823	Cmce	3.53	0.51	0.85	1.38	0.77
$NbCu_3Se_4$	mp-5621	$P\bar{4}3m$	3.13	0.82	0.82	0.82	0.82
VCu_3S_4	mp-3762	$P\bar{4}3m$	3.69	0.93	0.93	0.93	0.93
$CuBS_2$	mp-12954	$I\bar{4}2d$	3.15	0.93	1.07	1.07	1.0
$RbAu_3Se_2$	mp-9385	$P\bar{3}m1$	3.18	0.49	0.49	1.58	0.63
Ag_3AuS_2	mp-34460	$R\bar{3}m$	3.03	0.40	1.59	1.59	0.80
$NbCu_3S_4$	mp-5621	$P\bar{4}3m$	3.40	0.97	0.97	0.97	0.97
RbAuSe	mp-9731	Cmcm	3.39	0.56	1.13	5.66	1.0
KAuSe	mp-9881	Cmcm	3.42	0.54	1.23	5.48	1.0

killing the holes. To summarize, we had three compounds killed by S vacancies, three killed by metal antisite defects and two killed by interstitial defects. This leads to 8 out of 15 materials, which do not pass our intrinsic defect screening. This is in contrast to 4 out of 16 materials in case of the selenium-containing compounds.

As can be seen in Tab. 4.19, from the seven sulfide materials passing the intrinsic defect screening only IrSbS, Tl_3BS_3, and Ba_2GeS_4 do not posses a coinage metal in their formula. Ba_2GeS_4 is similar to Ba_2SiSe_4 and $Ba(BSe_3)_2$. In this case, Ge is surrounded by sulfur in a tetrahedral arrangement instead of selenium, which is found in the same arrangement for the two latter materials. Nevertheless, this is leading to a similar problem, as the vacancy of germanium is letting this material fail the dopant screening. As mentioned we were not able to finde a suitable dopant for Tl_3BS_3, which led this material fail the extrinsic defect screening. In IrSbS, the antisite defect S on Sb is the most troublesome defect, which is similar to selenium-containing compounds. Nevertheless, we were able to find a dopant, so that this material passed the hole defect screening. Finally, all sulfide- and coinage metal-containing materials, *i.e.* Ag_3AuS_2, VCu_3S_4, $NbCu_3S_4$, and $CuBS_2$ pass our intrinsic defect screening. The coinage metal vacancy renders all four compounds already intrinsic p-type, but we were not able to find dopants for Ag_3AuS_2 and $NbCu_3S_4$. For VCu_3S_4 and $CuBS_2$, we were able to find suitable dopants, so that these materials also passed our extrinsic defect screening.

Bibliography

[1] Walter Kohn. Nobel Lecture: Electronic Structure of Matter – Wave Functions and Density Functionals. *Reviews of Modern Physics*, 71(5):1253–1266, 1999.

[2] John A. Pople. Nobel Lecture: Quantum Chemical Models. *Reviews of Modern Physics*, 71(5):1267–1274, 1999.

[3] Dominik Marx and Jürg Hutter. *Ab Initio Molecular Dynamics*. Cambridge University Press, 2009.

[4] Jürg Hutter. Car-Parrinello Molecular Dynamic. *WIREs: Computational Molecular Science*, 2(4):604–612, 2012.

[5] Thomas D. Kühne. Second Generation Car-Parrinello Molecular Dynamics. *WIREs: Computational Molecular Science*, 4(4):391–406, 2014.

[6] Thomas D. Kühne, Pouya Partovi-Azar, and Hossam Elgabarty. Ab-Initio-Moleküldynamik. *Nachrichten aus der Chemie*, 63:327–330, 2015.

[7] Michele Parrinello. From Silicon to RNA: The Coming of Age of Ab Initio Molecular Dynamics. *Solid State Communications*, 102(2–3):107–120, 1997.

[8] Emil Prodan and Walter Kohn. Nearsightedness of Electronic Matter. *Proceedings of the National Academy of Sciences of the United States of America*, 102(33):11635–11638, 2005.

[9] Stefan Goedecker. Linear Scaling Electronic Structure Methods. *Reviews of Modern Physics*, 71(4):1085–1123, 1999.

[10] David R. Bowler and Tsuyoshi Miyazaki. O(n) Methods in Electronic Structure Calculations. *Reports on Progress in Physics*, 75(03):036503, 2012.

[11] Stefano Baroni and Paolo Giannozzi. Towards very Large-Scale Electronic-Structure Calculations. *Europhysics Letters*, 17(6):547–552, 1992.

[12] Weitao Yang. Direct Calculation of Electron Density in Density-Functional Theory. *Physical Review Letters*, 66(11):1438–1441, 1991.

[13] Guilia Galli and Michele Parrinello. Large Scale Electronic Structure Calculations. *Physical Review Letters*, 69(24):3547–3550, 1992.

[14] Francesco Mauri, Guilia Galli, and Roberto Car. Orbital Formulation for Electronic-Structure Calculaions with Linear System-Size Scaling. *Physical Review B*, 47(15):9973–9976, 1993.

[15] X.-P. Li, Ricardo W. Nunes, and David Vanderbilt. Density-Matrix Electronic-Structure Method with Linear System-Size Scaling. *Physical Review B*, 47(16):10891–10894, 1993.

[16] Adam H. R. Palser and David E. Manolopoulos. Canonical Purification of the Density Matrix in Electronic-Structure Theory. *Physical Review B*, 58(19):12704–12711, 1998.

[17] Laura E. Ratcliff, Stephan Mohr, Georg Huhs, Thierry Deutsch, Michel Masella, and Luigi Genovese. Challenges in Large Scale Quantum Mechanical Calculations. *WIREs: Computational Molecular Science*, 7(1):e1290, 2017.

[18] Nicholas D. M. Hine, Mark Robinson, Peter D. Haynes, Chris-Kriton Skylaris, Mike C. Payne, and Arash A. Mostofi. Accurate Ionic Forces and Geometry Optimization in Linear-Scaling Density-Functional Theory with Local Orbitals. *Physical Review B*, 83(19):195102, 2011.

[19] Joost VandeVondele, Urban Borstnik, and Jürg Hutter. Linear Scaling Self-Consistent Field Calculations with Millions of Atoms in the Condensed Phase. *Journal of Chemical Theory and Computation*, 8(10):3565—3573, 2012.

[20] Rustam Z. Khaliullin, Joost VandeVondele, and Jürg Hutter. Efficient Linear-Scaling Density Functional Theory for Molecular Systems. *Journal of Chemical Theory and Computation*, 9(10):4421—4427, 2013.

[21] Stephan Mohr, Laura E. Ratcliff, Paul Boulanger, Luigi Genovese, Damien Caliste, Thierry Deutsch, and Stefan Goedecker. Daubechies Wavelets for Linear Scaling Density Functional Theory. *The Journal of Chemical Physics*, 140(20):204110, 2014.

[22] Fuyuki Shimojo, Shinnosuke Hattori, Rajiv K. Kalia, Manaschai Kunaseth, Weiwei Mou, Aiichiro Nakano, Ken-ichi Nomura, Satoshi Ohmura, Pankaj Rajak, Kohei Shimamura, and Priya Vashishta. A Divide-Conquer-Recombine Algorithmic Paradigm for Large Spatiotemporal Quantum molecular Dynamics Simulations. *The Journal of Chemical Physics*, 140(18):18A529, 2014.

[23] Michiaki Arita, David R. Bowler, and Tsuyoshi Miyazaki. Stable and Efficient Linear Scaling First-Principles Molecular Dynamics for 10000+ atoms. *Journal of Chemical Theory and Computation*, 10(12):5419–5425, 2014.

[24] Stephan Mohr, Laura E. Ratcliff, Luigi Genovese, Damien Caliste, Paul Boulanger, Stefan Goedecker, and Thierry Deutsch. Accurate and Efficient Linear Scaling DFT Calculations with Universal Applicability. *Physical Chemistry Chemical Physics*, 17(47):31360–31370, 2015.

[25] Dorothee Richters and Thomas D. Kühne. Linear-Scaling Self-Consistent Field Theory Based Molecular Dynamics: Application to C_{60} Buckyballs Colliding with Graphite. *Molecular Simulation*, 44(17):1380–1386, 2018.

[26] Ali Alavi and Daan Frenkel. Grand-Canonical Simulations of Solvated Ideal Fermions. Evidence for Phase Separation. *The Journal of Chemical Physics*, 97(12):9249–9257, 1992.

[27] Ali Alavi, Jorge Kohanoff, Michele Parrinello, and Daan Frenkel. Ab Initio Molecular Dynamics with Excited Electrons. *Physical Review Letters*, 73(19):2599–2602, 1994.

[28] Florian R. Krajewski and Michele Parrinello. Linear Scaling Electronic Structure Calculations and Accurate Statistical Mechanics Sampling with Noisy Forces. *Physical Review B*, 73(4):041105, 2006.

[29] Dorothee Richters and Thomas D. Kühne. Self-Consistent Field Theory Based Molecular Dynamics with Linear System-Size Scaling. *The Journal Chemical Physics*, 140(13):134109, 2014.

[30] Istvan Montvay and Gernot Münster. *Quantum Fields on a Lattice*. Cambridge Monographs on Mathematical Physics. Cambridge University Press, 1994.

[31] Michele Ceriotti, Thomas D. Kühne, and Michele Parrinello. An Efficient and Accurate Decomposition of the Fermi Operator. *The Journal Chemical Physics*, 129(2):024707, 2008.

[32] Michele Ceriotti, Thomas D. Kühne, and Michele Parrinello. A Hybrid Approach to Fermi Operator Expansion. *AIP Conference Proceedings*, 1148(1):658–661, 2009.

[33] Joost VandeVondele, Matthias Krack, Fawzi Mohamed, Michele Parrinello, Thomas Chassaing, and Jürg Hutter. Quickstep: Fast and Accurate Density Functional Calculations Using a Mixed Gaussian and Plane Waves Approach. *Computer Physics Communications*, 167(2):103–128, 2005.

[34] Luigi Genovese, Alexey Neelov, Stefan Goedecker, Thierry Deutsch, Seyed Alireza Ghasemi, Alexander Willand, Damien Caliste, Oded Zilberberg, Mark Rayson, Anders Bergman, and Reinhold Schneider. Daubechies Wavelets as a Basis Set for Density Functional Pseudopotential Calculations. *The Journal Chemical Physics*, 129(1):014109, 2008.

[35] Scott Habershon, Thomas E. Markland, and David E. Manolopoulos. Competing Quantum Effects in the Dynamics of a Flexible Water Model. *The Journal Chemical Physics*, 131(2):024501, 2009.

[36] Revati Kumar and James L. Skinner. Water Simulation Model with Explicit Three-Molecule Interactions. *The Journal of Physical Chemistry B*, 112(28):8311–8318, 2008.

[37] Craig Tainter, Piotr A. Pieniazek, Yu-Shan Lin, and James L. Skinner. Robust Three-Body Water Simulation Model. *The Journal Chemical Physics*, 134(18):184501, 2011.

[38] Daan Frenkel and Berend Smit. *Understanding Molecular Simulation - From Algorithms to Applications*, Volume 1 of *Computational Science - From Theory to Applications*. Academic Press, 2002.

[39] Hans C. Andersen. Molecular Dynamics Simulations at Constant Pressure and/or Temperature. *The Journal Chemical Physics*, 72(4):2384–2393, 1980.

[40] Scott Habershon, David E. Manolopoulos, Thomas E. Markland, and Thomas F. Miller III. Ring-Polymer Molecular Dynamics: Quantum Effects in Chemical Dynamics from Classical Trajectories in an Extended Phase Space. *Annual Review of Physical Chemistry*, 64:387–413, 2013.

[41] Thomas E. Markland and David E. Manolopoulos. An Efficient Ring Polymer Contraction Scheme for Imaginary Time Path Integral Simulations. *The Journal Chemical Physics*, 129(2):024105, 2008.

[42] Thomas E. Markland and David E. Manolopoulos. A Refined Ring Polymer Contraction Scheme for Systems with Electrostatic Interactions. *Chemical Physics Letters*, 464(4-6):256–261, 2008.

[43] M. Tuckerman, B. J. Berne, and G. J. Martyna. Reversible Multiple Time Scale Molecular Dynamics. *The Journal Chemical Physics*, 97(3):1990–2001, 1992.

[44] Florian R. Krajewski and Michele Parrinello. Stochastic Linear Scaling for Metals and Nonmetals. *Physical Review B*, 71(23):233105, 2005.

[45] Thomas D. Kühne, Matthias Krack, Fawzi R. Mohamed, and Michele Parrinello. Efficient and Accurate Car-Parrinello-like Approach to Born-Oppenheimer Molecular Dynamics. *Physical Review Letters*, 98(6):066401, 2007.

[46] Thomas D. Kühne, Matthias Krack, and Michele Parrinello. Static and Dynamical Properties of Liquid Water from First Principles by a Novel Car-Parrinello-like Approach. *Journal of Chemical Theory and Computation*, 5(2):235–241, 2009.

[47] Kristof Karhan, Rustam Z. Khaliullin, and Thomas D. Kühne. On the Role of Interfacial Hydrogen Bonds in "On-Water" Catalysis. *The Journal Chemical Physics*, 141(22):22D528, 2014.

[48] Peter Würfel and Uli Würfel. *Physics of Solar Cells*. Wiley, 2016.

[49] NREL Efficiency Chart. https://www.nrel.gov/pv/cell-efficiency.html (accessed 21.12.2019)

[50] William Shockley and Hans J. Queisser. Detailed Balance Limit of Efficiency of p-n Junction Solar Cells. *Journal of Applied Physics*, 32(3):510–519, 1961.

[51] Rudolf Gross and Achim Marx. *Festkörperphysik*. 2. Auflage, De Gruyter, 2014.

[52] Kun-Han Lin, Antonio Prlj, and Clémence Corminboeuf. A Rising Star: Truxene as a Promising Hole Transport Material in Perovskite Solar Cells. *The Journal of Physical Chemistry C*, 121(39):21729–21739, 2017.

[53] Ramya Kormath Madam Raghupathy, Thomas D. Kühne, Claudia Felser, and Hossein Mirhosseini. Rational Design of Transparent p-Type Conducting Non-Oxide Materials from High-Throughput Calculations. *Journal of Materials Chemistry C*, 6(3):541–549, 2018.

[54] W. H. Strehlow and Earl L. Cook. Compilation of Energy Band Gaps in Elemental and Binary Compound Semiconductors and Insulators. *Journal of Physical and Chemical Reference Data*, 2(1):163–200, 1973.

[55] Alexandr Fonari and Christopher Sutton. Validation of the Effective Masses Calculated Using Finite Difference Method on a Five-Point Stencil for Inorganic and Organic Semiconductors. *arXiv Preprint*, arXiv:1302.4996, 2013.

[56] John P. Perdew, Kieron Burke, and Matthias Ernzerhof. Generalized Gradient Approximation Made Simple. *Physical Review Letters*, 77(18):3865–3868, 1996.

[57] Fabien Tran and Peter Blaha. Importance of the Kinetic Energy Density for Band Gap Calculations in Solids with Density Functional Theory. *The Journal of Physical Chemistry A*, 121(17):3318–3325, 2017.

[58] Samuel A. Miller, Maxwell Dylla, Shashwat Anand, Kiarash Gordiz, G. Jeffrey Snyder, and Eric S. Toberer. Empirical Modeling of Dopability in Diamond-like Semiconductors. *npj Computational Materials*, 4:71, 2018.

[59] Keith T. Butler, Yu Kumagai, Fumiyasu Oba, and Aron Walsh. Screening Procedure for Structurally and Electronically Matched Contact Layers for High-Performance Solar Cells: Hybrid Perovskites. *Journal of Materials Chemistry C*, 4(6):1149–1158, 2016.

[60] Georg K.H. Madsen and David J. Singh. BoltzTraP. A Code for Calculating Band-Structure Dependent Quantities. *Computer Physics Communications*, 175(1):67–71, 2006.

[61] Kiran Mathew, Arunima K. Singh, Joshua J. Gabriel, Kamal Choudhary, Susan B. Sinnott, Albert V. Davydov, Francesca Tavazza, and Richard G. Hennig. MPInterfaces: A Materials Project Based Python Tool for High-Throughput Computational Screening of Interfacial Systems. *Computational Materials Science*, 122:183–190, 2016.

[62] Francesco Ricci, Wei Chen, Umut Aydemir, G. Jeffrey Snyder, Gian-Marco Rignanese, Anubhav Jain, and Geoffroy Hautier. An Ab Initio Electronic Transport Database for Inorganic Materials. *Scientific Data*, 4:170085, 2017.

[63] Anubhav Jain, Shyue Ping Ong, Geoffroy Hautier, Wei Chen, William Davidson Richards, Stephen Dacek, Shreyas Cholia, Dan Gunter, David Skinner, Gerbrand Ceder, and Kristin A. Persson. Commentary: The Materials Project: A Materials Genome Approach to Accelerating Materials Innovation. *APL Materials*, 1(1):011002, 2013.

[64] Guillaume Brunin, Francesco Ricci, Viet-Anh Ha, Gian-Marco Rignanese, and Geoffroy Hautier. Transparent Conducting Materials Discovery Using High-Throughput Computing. *npj Computational Materials*, 5:63, 2019.

[65] Lianshan Lin. Materials Databases Infrastructure Constructed by First Principles Calculations: A Review. *Materials Performance and Characterization*, 4(1):148–169, 2015.

[66] The NOMAD Laboratory A European Centre of Excellence. https://nomad-coe.eu/ (accessed 05.01.2020)

[67] Giovanni Pizzi, Andrea Cepellotti, Riccardo Sabatini, Nicola Marzari, and Boris Kozinsky. AiiDA: Automated Interactive Infrastructure and Database for Computational Science. *Computational Materials Science*, 111:218–230, 2016.

[68] Tam Mayeshiba, Henry Wu, Thomas Angsten, Amy Kaczmarowski, Zhewen Song, Glen Jenness, Wei Xie, and Dane Morgan. The Materials Simulation Toolkit (MAST) for Atomistic Modeling of Defects and Diffusion. *Computational Materials Science*, 126:90–102, 2017.

[69] Scott Kirklin, James E Saal, Bryce Meredig, Alex Thompson, Jeff W Doak, Muratahan Aykol, Stephan Rühl, and Chris Wolverton. The Open Quantum Materials Database (OQMD): Assessing the Accuracy of DFT Formation Energies. *npj Computational Materials*, 1:15010, 2015.

[70] Inorganic Crystal Structure Database. https://icsd.products.fiz-karlsruhe.de/ (accessed 05.01.2020)

[71] Shyue Ping Ong, Shreyas Cholia, Anubhav Jain, Miriam Brafman, Dan Gunter, Gerbrand Ceder, and Kristin A. Persson. The Materials Application Programming Interface (API): A Simple, Flexible and Efficient API for Materials Data Based on Representational State Transfer (REST) Principles. *Computational Materials Science*, 97:209–215, 2015.

[72] Kiran Mathew, Joseph H. Montoya, Alireza Faghaninia, Shyam Dwarakanath, Muratahan Aykol, Hanmei Tang, Iek-heng Chu, Tess Smidt, Brandon Bocklund, Matthew Horton, John Dagdelen, Brandon Wood, Zi-Kui Liu, Jeffrey Neaton, Shyue Ping Ong, Kristin Persson, and Anubhav Jain. Atomate: A High-Level Interface to Generate, Execute, and Analyze Computational Materials Science Workflows. *Computational Materials Science*, 139:140–152, 2017.

[73] Anubhav Jain, Shyue Ping Ong, Wei Chen, Bharat Medasani, Xiaohui Qu, Michael Kocher, Miriam Brafman, Guido Petretto, Gian-Marco Rignanese, Geoffroy Hautier, Daniel Gunter, and Kristin A Persson. FireWorks: A Dynamic Workflow System Designed for High-Throughput Applications. *Concurrency and Computation: Practice and Experience*, 27(17):5037–5059, 2015.

[74] Logan Ward, Alexander Dunn, Alireza Faghaninia, Nils E.R. Zimmermann, Saurabh Bajaj, Qi Wang, Joseph Montoya, Jiming Chen, Kyle Bystrom, Maxwell Dylla, Kyle Chard, Mark Asta, Kristin A. Persson, G. Jeffrey Snyder, Ian Foster, and Anubhav Jain. Matminer: An Open Source Toolkit for Materials Data Mining. *Computational Materials Science*, 152(April):60–69, 9 2018.

[75] Danny Broberg, Bharat Medasani, Nils E.R. Zimmermann, Guodong Yu, Andrew Canning, Maciej Haranczyk, Mark Asta, and Geoffroy Hautier. PyCDT: A Python Toolkit for Modeling Point Defects in Semiconductors and Insulators. *Computer Physics Communications*, 226:165–179, 2018.

[76] Arunima K. Singh, Lan Zhou, Aniketa Shinde, Santosh K. Suram, Joseph H. Montoya, Donald Winston, John M. Gregoire, and Kristin A. Persson. Electrochemical Stability of Metastable Materials. *Chemistry of Materials*, 29(23):10159–10167, 2017.

[77] Sabine Körbel, Miguel A.L. Marques, and Silvana Botti. Stability and Electronic Properties of New Inorganic Perovskites from High-Throughput: Ab Initio Calculations. *Journal of Materials Chemistry C*, 4(15):3157–3167, 2016.

[78] Hans Georg von Schnering, Martin Hartweg, Ute Hartweg, and Wolfgang Hönle. K_4P_3, eine Verbindung mit dem Radikalanion ${P_3}^{4-}$. *Angewandte Chemie*, 101(1):98–99, 1989.

[79] Shyue Ping Ong, Lei Wang, Byoungwoo Kang, and Gerbrand Ceder. $Li-Fe-P-O_2$ Phase Diagram from First Principles Calculations. *Chemistry of Materials*, 20(5):1798–1807, 2008.

[80] Anubhav Jain, Geoffroy Hautier, Shyue Ping Ong, Charles J. Moore, Christopher C. Fischer, Kristin A. Persson, and Gerbrand Ceder. Formation Enthalpies by Mixing GGA and GGA + U Calculations. *Physical Review B*, 84(4):045115, 2011.

[81] Geert Gnutzmann, Friedrich Wilhelm Dorn, and Wilhelm Klemm. Das Verhalten der Alkalimetalle zu Halbmetallen. VII. Über einige A_3B- und AB_2-Verbindungen der schweren Alkalimetalle mit Elementen der V. Gruppe. *Zeitschrift für anorganische und allgemeine Chemie*, 309(3-4):210–225, 1961.

[82] Hans Georg von Schnering, M. Somer, G Kliche, Wolfgang Hönle, T Meyer, J Wolf, L. Ohse, and P. B. Kempa. Chemie und Strukturchemie von Phosphiden und Polyphosphiden. 53. Darstellung, Eigenschaften und Schwingungsspektren

der Käfiganionen $P_{11}{}^{3-}$ und $As_{11}{}^{3-}$. *Zeitschrift für anorganische und allgemeine Chemie*, 601(1):13–30, 1991.

[83] Hans Georg von Schnering, and Wolfgang Hönle. Zur Chemie und Strukturchemie der Phosphide und Polyphosphide. 20. Darstellung, Struktur und Eigenschaften der Alkalimetallmonophosphide NaP und KP. *Zeitschrift für anorganische und allgemeine Chemie*, 456(1):194–206, 1979.

[84] Hans-Peter Abicht, Wolfgang Hönle, and Hans Georg von Schnering. Zur Chemie und Strukturchemie von Phosphiden und Polyphosphiden. 36. Tetrakaliumhexaphosphid: Darstellung, Struktur und Eigenschaften von $\alpha-K_4P_6$ und $\beta-K_4P_6$. *Zeitschrift für anorganische und allgemeine Chemie*, 519(12):7–23, 1984.

[85] Hans Georg von Schnering and H. Schmidt. KP_{15}, ein neues Kaliumpolyphosphid. *Angewandte Chemie*, 79(7):323–323, 1967.

[86] Rachel Woods-Robinson, Danny Broberg, Alireza Faghaninia, Anubhav Jain, Shyam S. Dwaraknath, and Kristin A. Persson. Assessing High-Throughput Descriptors for Prediction of Transparent Conductors. *Chemistry of Materials*, 30(22):8375–8389, 2018.

[87] John P. Perdew, Weitao Yang, Kieron Burke, Zenghui Yang, Eberhard K. U. Gross, Matthias Scheffler, Gustavo E. Scuseria, Thomas M. Henderson, Igor Ying Zhang, Adrienn Ruzsinszky, Haowei Peng, Jianwei Sun, Egor Trushin, and Andreas Görling. Understanding Band Gaps of Solids in Generalized Kohn–Sham Theory. *Proceedings of the National Academy of Sciences*, 114(11):2801–2806, 2017.

[88] Volker Heine. Theory of Surface States. *Physical Review*, 138(6A):A1689–A1696, 6 1965.

[89] Winfried Mönch. Empirical Tight-Binding Calculation of the Branch-Point Energy of the Continuum of Interface-Induced Gap States. *Journal of Applied Physics*, 80(9):5076–5082, 1996.

[90] Manuel Cardona and Niels E Christensen. Acoustic Deformation Potentials and Heterostructure Band Offsets in Semiconductors. *Physical Review B*, 35(12):6182–6194, 1987.

[91] André Schleife, Frank Fuchs, Claudia Rödl, Jürgen Furthmüller, and Friedhelm Bechstedt. Branch-Point Energies and Band Discontinuities of III-Nitrides and III-/II-Oxides from Quasiparticle Band-Structure Calculations. *Applied Physics Letters*, 94(1):012104, 2009.

[92] Daniel W. Davies, Keith T. Butler, Jonathan M. Skelton, Congwei Xie, Artem R. Oganov, and Aron Walsh. Computer-Aided Design of Metal Chalcohalide Semiconductors: From Chemical Composition to Crystal Structure. *Chemical Science*, 9(4):1022–1030, 2018.

[93] Jerry Tersoff. Theory of Semiconductor Heterojunctions: The Role of Quantum Dipoles. *Physical Review B*, 30(8):4874–4877, 1984.

[94] Alfonso Baldereschi. Mean-Value Point in the Brillouin Zone. *Physical Review B*, 7(12):5212–5215, 1973.

[95] Peter Deák, Bálint Aradi, and Thomas Frauenheim. Band Lineup and Charge Carrier Separation in Mixed Rutile-Anatase Systems. *Journal of Physical Chemistry C*, 115(8):3443–3446, 2011.

[96] Jochen Heyd, Gustavo E. Scuseria, and Matthias Ernzerhof. Hybrid Functionals Based on a Screened Coulomb Potential. *The Journal of Chemical Physics*, 118(18):8207–8215, 2003.

[97] Nasrin Sarmadian, Rolando Saniz, Bart Partoens, Dirk Lamoen, Kalpana Volety, Guido Huyberechts, and Johan Paul. High Throughput First-Principles Calculations of Bixbyite Oxides for TCO Applications. *Physical Chemistry Chemical Physics*, 16(33):17724–17733, 2014.

[98] Nasrin Sarmadian, Rolando Saniz, Bart Partoens, and Dirk Lamoen. Easily Doped p-Type, low Hole Effective Mass, Transparent Oxides. *Scientific Reports*, 6:20446, 2016.

[99] Yoyo Hinuma, Andreas Grüneis, Georg Kresse, and Fumiyasu Oba. Band Alignment of Semiconductors from Density-Functional Theory and Many-Body Perturbation Theory. *Physical Review B - Condensed Matter and Materials Physics*, 90(15):1–16, 2014.

[100] Pedro Borlido, Thorsten Aull, Ahmad W. Huran, Fabien Tran, Miguel A. L. Marques, and Silvana Botti. Large-Scale Benchmark of Exchange–Correlation Functionals for the Determination of Electronic Band Gaps of Solids. *Journal of Chemical Theory and Computation*, 15(9):5069–5079, 2019.

[101] Kanghoon Yim, Yong Youn, Miso Lee, Dongsun Yoo, Joohee Lee, Sung Haeng Cho, and Seungwu Han. Computational Discovery of p-Type Transparent Oxide Semiconductors Using Hydrogen Descriptor. *npj Computational Materials*, 4:17, 2018.

[102] Christoph Freysoldt, Jörg Neugebauer, and Chris G. Van de Walle. Fully Ab Initio Finite-Size Corrections for Charged-Defect Supercell Calculations. *Physical Review Letters*, 102(1):016402, 2009.

[103] Yu Kumagai and Fumiyasu Oba. Electrostatics-Based Finite-Size Corrections for First-Principles Point Defect Calculations. *Physical Review B*, 89(19):195205, 2014.

[104] Zhang and Northrup. Chemical Potential Dependence of Defect Formation Energies in GaAs: Application to Ga Self-Diffusion. *Physical review letters*, 67(17):2339–2342, 1991.

[105] Chris G. Van de Walle and Anderson Janotti. Advances in Electronic Structure Methods for Defects and Impurities in Solids. *physica status solidi (b)*, 248(1):19–27, 2011.

[106] Otfried Madelung. *Semiconductors: Data Handbook*. Springer Berlin Heidelberg, Berlin, Heidelberg, 2004.

[107] Nikolas J. Podraza, Wei Qiu, Beverly B. Hinojosa, Michael A. Motyka, Simon R. Phillpot, James E. Baciak, Susan Trolier-McKinstry, and Juan C. Nino. Band gap and Structure of Single Crystal BiI_3 : Resolving Discrepancies in Literature. *Journal of Applied Physics*, 114(3):033110, 7 2013.

[108] C. M. Fang, R A de Groot, R. J. Bruls, H. T. Hintzen, and G de With. Ab Initio Band Structure Calculations of Mg_3N_2 and $MgSiN_2$. *Journal of Physics: Condensed Matter*, 11(25):4833–4842, 1999.

[109] Nils Wiberg, Egon Wiberg, and Arnold F. Holleman. *Lehrburch der Anorganischen Chemie*. de Gruyter, Berlin, 102. Auflage, 2008.

[110] Peter Atkins, Tina Overton, Jonathan Rourke, Mark Weller, and Fraser Armstrong. *Shriver & Atkins Inorganic Chemistry*. Oxford University Press, Oxford, 5th Edition, 2009.

[111] R. W. Olesinski, N. Kanani, and Gholamreza J. Abbaschian. The P−Si (Phosphorus-Silicon) system. *Bulletin of Alloy Phase Diagrams*, 6(2):130–133, 1985.

[112] Victor Manriquez, Wolfgang Hönle, and Hans Georg von Schnering. Zur Chemie und Strukturchemie von Phosphiden und Polyphosphiden. 42. Trilithiumheptaphosphid Li_3P_7: Darstellung, Struktur und Eigenschaften. *Zeitschrift für anorganische und allgemeine Chemie*, 539(8):95–109, 1986.

[113] Institut für Arbeitsschutz der Deutschen Gesetzlichen Unfallversicherung (IFA). GESTIS-Stoffdatenbank. https://www.dguv.de/ifa%3B/gestis/gestis-stoffdatenbank/index.jsp (accessed 05.01.2020)

[114] Jing Li, Ki-Bum Nam, Mim Lal Nakarmi, Joung-Yol Lin, Hongxing Jiang, Pierre Carrier, and Su-Huai Wei. Band Structure and Fundamental Optical Transitions in Wurtzite AlN. *Applied Physics Letters*, 83(25):5163–5165, 2003.

[115] Chikara Sugiura. Chlorine K X-Ray Spectra and Electronic Band Structures of $MgCl_2$, $CaCl_2$, $SrCl_2$ and $BaCl_2$. *Physical Review B*, 9(6):2679–2683, 1974.

[116] Andrew Evans, Andy G. McGlynn, Brian M. Towlson, Matt Gunn, D. Jones, Tudor E. Jenkins, Rudi Winter, and Nigel R. J. Poolton. Determination of the Optical Band-Gap Energy of Cubic and Hexagonal Boron Nitride Using Luminescence Excitation Spectroscopy. *Journal of Physics: Condensed Matter*, 20(7):075233, 2008.

[117] Glen A. Slack, Thomas F. McNelly, and E.A. Taft. Melt Growth and Properties of B_6P Crystals. *Journal of Physics and Chemistry of Solids*, 44(10):1009–1013, 1983.

[118] Jean P. Odile, S. Soled, C. A. Castro, and Aaron Wold. Crystal Growth and Characterization of the Transition-Metal Phosphides CuP_2, NiP_2, and RhP_3. *Inorganic Chemistry*, 17(2):283–286, 1978.

[119] Thomas M. Tolhurst, Cordula Braun, Teak D. Boyko, Wolfgang Schnick, and Alexander Moewes. Experiment-Driven Modeling of Crystalline Phosphorus Nitride P_3N_5 : Wide-Ranging Implications from a Unique Structure. *Chemistry - A European Journal*, 22(30):10475–10483, 2016.

[120] Alvin M. Goodman. Photoemission of Electrons and Holes into Silicon Nitride. *Applied Physics Letters*, 13(8):275–277, 1968.

[121] Naruhito Ohno, Yasuhiro Yamasaki, Hajime Yoshida, and Masami Fujita. Optical Spectra of Orthorhombic $SnBr_2$ Crystals. *physica status solidi (b)*, 223(3):723–728, 2001.

[122] Jun-ichi Nara and Sadao Adachi. Optical Properties of $SnCl_2$ Phosphor. *Journal of Applied Physics*, 109(8):083539, 2011.

[123] Apurbal Lal Ray, Holland M. Smith, and Nancy M. Haegel. Temperature Dependence of the indirect Bandgap in Thallium Bromide from Cathodoluminescence Spectroscopy. *Journal of Applied Physics*, 115(16):163709, 2014.

[124] Hongliang Shi and Mao-Hua Du. Shallow Halogen Vacancies in Halide Optoelectronic Materials. *Physical Review B*, 90(17):174103, 2014.

[125] Ronald W. Gurney and Nevill F. Mott. The Theory of the Photolysis of Silver Bromide and the Photographic Latent Image. *Proceedings of the Royal Society of London. Series A - Mathematical and Physical Sciences*, 164(917):151–167, 1938.

[126] Robert T. Paine and Chaitanya K. Narula. Synthetic Routes to Boron Nitride. *Chemical Reviews*, 90(1):73–91, 1990.

[127] Hisanori Yamane, Shinichi Kikkawa, Hiroyuki Horiuchi, and Mitsue Koizumi. Structure of a New Polymorph of Lithium Boron Nitride, Li_3BN_2. *Journal of Solid State Chemistry*, 65(1):6–12, 1986.

[128] Yajie Wang, Robert Wenisch, Rutger Schlatmann, and Iver Lauermann. Inorganic Materials as Hole Selective Contacts and Intermediate Tunnel Junction Layer for Monolithic Perovskite-CIGSe Tandem Solar Cells. *Advanced Energy Materials*, 8(30):1801692, 2018.

[129] Xiaoyong Liang, Qing Yi, Sai Bai, Xingliang Dai, Xin Wang, Zhizhen Ye, Feng Gao, Fengling Zhang, Baoquan Sun, and Yizheng Jin. Synthesis of Unstable Colloidal Inorganic Nanocrystals through the Introduction of a Protecting Ligand. *Nano Letters*, 14(6):3117–3123, 2014.

[130] K. Tennakone, G.R.R.A. Kumara, I.R.M. Kottegoda, V.P.S. Perera, G.M.L.P. Aponsu, and K.G.U. Wijayantha. Deposition of Thin Conducting Films of CuI on Glass. *Solar Energy Materials and Solar Cells*, 55(3):283–289, 1998.

[131] Arun K. Prasad, David J. Kubinski, and Pelagia-Irene Gouma. Comparison of Sol-Gel and Ion Beam Deposited MoO_3 Thin Film Gas Sensors for Selective Ammonia Detection. *Sensors and Actuators, B: Chemical*, 93(1-3):25–30, 2003.

[132] Xiang Yao, Wenzhan Xu, Xiaojuan Huang, Jun Qi, Qingwu Yin, Xiaofang Jiang, Fei Huang, Xiong Gong, and Yong Cao. Solution-Processed Vanadium Oxide Thin Film as the Hole Extraction Layer for Efficient Hysteresis-Free Perovskite Hybrid Solar Cells. *Organic Electronics*, 47:85–93, 2017.

[133] Anubhav Jain, Geoffroy Hautier, Charles J. Moore, Shyue Ping Ong, Christopher C. Fischer, Tim Mueller, Kristin A. Persson, and Gerbrand Ceder. A High-Throughput Infrastructure for Density Functional Theory Calculations. *Computational Materials Science*, 50(8):2295–2310, 2011.

[134] Sigrid Furuseth, Kari Selte, Hakon Hope, Arne Kjekshus, and Bernt Klewe. Iodine Oxides. Part V. The Crystal Structure of $(IO)_2SO_4$. *Acta Chemica Scandinavica A*, 28:71–76, 1974.

[135] Pekka Pyykkö and Jean Paul Desclaux. Relativity and The Periodic System of Elements. *Accounts of Chemical Research*, 12(8):276–281, 1979.

[136] Max Born and Joseph E. Mayer. Zur Gittertheorie der Ionenkristalle. *Zeitschrift für Physik*, 75(1-2):1–18, 1932.

[137] Joseph E. Mayer. Dispersion and Polarizability and the Van der Waals Potential in the Alkali Halides. *The Journal of Chemical Physics*, 1(4):270–279, 1933.

[138] Maurice L. Huggins and Joseph E. Mayer. Interatomic Distances in Crystals of the Alkali Halides. *The Journal of Chemical Physics*, 1(9):643–646, 1933.

[139] L. G. Schulz. Polymorphism of Cesium and Thallium Halides. *Acta Crystallographica*, 4(6):487–489, 1951.

[140] Donald W. Pashley. The Nucleation, Growth, Structure and Epitaxy of Thin Surface Films. *Advances in Physics*, 14(55):327–416, 1965.

[141] Viet-Anh Ha, Francesco Ricci, Gian-Marco Rignanese, and Geoffroy Hautier. Structural Design Principles for Low Hole Effective Mass s-Orbital-Based p-Type Oxides. *Journal of Materials Chemistry C*, 5(23):5772–5779, 2017.

[142] Paul J. Sellin. Thick Film Compound Semiconductors for X-Ray Imaging Applications. *Nuclear Instruments and Methods in Physics Research, Section A: Accelerators, Spectrometers, Detectors and Associated Equipment*, 563(1):1–8, 2006.

[143] B. W. Lucas. Structure (Neutron) of Potassium Iodate at 100 and 10 K. *Acta Crystallographica Section C Crystal Structure Communications*, 41(10):1388–1391, 1985.

[144] Matthew A. Brown, Zhi Liu, Paul D. Ashby, Apurva Mehta, Ronald L. Grimm, and John C. Hemminger. Surface Structure of KIO_3 Grown by Heterogeneous Reaction of Ozone with KI (001). *The Journal of Physical Chemistry C*, 112(47):18287–18290, 2008.

[145] Alfried Haase and Georg Brauer. Hydratstufen und Kristallstrukturen von Bariumchlorid. *Zeitschrift für anorganische und allgemeine Chemie*, 441(1):181–195, 1978.

[146] Taylor Shoulders and Romain M. Gaume. Phase-Change Sintering of $BaCl_2$ Transparent Ceramics. *Journal of Alloys and Compounds*, 705:517–523, 2017.

[147] Pradeep Kumar and Agnikumar G. Vedeshwar. DFT Calculations of Structural, Electronic, Optical and Elastic Properties of Scintillator Materials $BaCl_2$ and $BaBr_2$. *Journal of Physics D: Applied Physics*, 48(10):105301, 2015.

[148] Stephen Hull, Stefan T. Norberg, Istaq Ahmed, Sten G. Eriksson, and Chris E. Mohn. High Temperature Crystal Structures and Superionic Properties of $SrCl_2$, $SrBr_2$, $BaCl_2$ and $BaBr_2$. *Journal of Solid State Chemistry*, 184(11):2925–2935, 2011.

[149] Hans J. Seifert and Friedrich W. Koknat. Über die Systeme $KCl/MnCl_2$ und $NaCl/MnCl_2$ sowie die Strukturverhältnisse der Alkalichloromanganate(II). 341(5-6):269–280, 1966.

[150] J. Goodyear, E. M. Ali, and Gottfried A. Steigmann. Rubidium Tetrachloromanganate. *Acta Crystallographica*, B33:2932–2933, 1976.

[151] J. Makovsky, A. Zodkevitz, and Z. H. Kalman. Single Crystal Growth of Rb_2MnCl_4 and $Rb_3Mn_2Cl_7$. *Journal of Crystal Growth*, 11(1):99–100, 1971.

[152] Ursula Kambli, Hans U. Gudel, and Bernard Briat. Optical Absorption and Luminescence Studies of the 2D Antiferromagnets Rb_2MnCl_4 and $Rb_3Mn_2Cl_7$. *Journal of Physics C: Solid State Physics*, 17(17):3113–3122, 1984.

[153] Taiju Tsuboi, Pertti Silfsten, and Katsunori Iio. Time-Resolved Luminescence Spectra of Rb_2MnCl_4 Crystals. *physica status solidi (b)*, 170(1):K55–K59, 1992.

[154] Joseph S. Manser, Jeffrey A. Christians, and Prashant V. Kamat. Intriguing Optoelectronic Properties of Metal Halide Perovskites. *Chemical Reviews*, 116(21):12956–13008, 2016.

[155] Yang Zhou, Jie Chen, Osman M. Bakr, and Hong-Tao Sun. Metal-Doped Lead Halide Perovskites: Synthesis, Properties, and Optoelectronic Applications. *Chemistry of Materials*, 30(19):6589–6613, 2018.

[156] Timo Taetz. Zur Darstellung und Charakterisierung ausgewählter Übergangsmetalloxide - Ein Beitrag zu niedrigdimensionalen S = 1/2 Systemen. *Dissertation, Universität zu Köln*, 2008.

[157] Federico Bisti, Victor A. Rogalev, Michael Karolak, Soumyadeep Paul, Ankur Gupta, Thorsten Schmitt, Gernot Güntherodt, Volker Eyert, Giorgio Sangiovanni, Gianni Profeta, and Vladimir N. Strocov. Weakly-Correlated Nature of Ferromagnetism in Nonsymmorphic CrO_2 Revealed by Bulk-Sensitive Soft-X-Ray ARPES. *Physical Review X*, 7(4):041067, 2017.

[158] Peter G. Jones and Eberhard Bembenek. Low-Temperature Redetermination of the Structures of Three Gold Compounds. *Journal of Crystallographic and Spectroscopic Research*, 22(4):397–401, 1992.

[159] Shoji Yamanaka. Intercalation and Superconductivity in Ternary Layer Structured Metal Nitride Halides (MNX: M = Ti, Zr, Hf; X = Cl, Br, I). *Journal of Materials Chemistry*, 20(15):2922, 2010.

[160] Viet-Anh Ha, Guodong Yu, Francesco Ricci, Diana Dahliah, Michiel J. van Setten, Matteo Giantomassi, Gian-Marco Rignanese, and Geoffroy Hautier. Computationally Driven High-Throughput Identification of CaTe and Li_3Sb as Promising Candidates for High-Mobility p-Type Transparent Conducting Materials. *Physical Review Materials*, 3(3):034601, 2019.

[161] Otto Schmitz-DuMont and Horst Bornefeld. Über den Einfluß des Kationenradius auf die Bildungsenergie von Anlagerungsverbindungen. VIII. Die Systemreihe Alkalifluorid/Zinkfluorid. *Zeitschrift für anorganische und allgemeine Chemie*, 287(3):120–137, 1956.

[162] Joel B. Varley, Anna Miglio, Viet-Anh Ha, Michiel J. van Setten, Gian-Marco Rignanese, and Geoffroy Hautier. High-Throughput Design of Non-Oxide p-Type Transparent Conducting Materials: Data Mining, Search Strategy, and Identification of Boron Phosphide. *Chemistry of Materials*, 29(6):2568–2573, 2017.

[163] Yoyo Hinuma, Taisuke Hatakeyama, Yu Kumagai, Lee A. Burton, Hikaru Sato, Yoshinori Muraba, Soshi Iimura, Hidenori Hiramatsu, Isao Tanaka, Hideo Hosono, and Fumiyasu Oba. Discovery of Earth-Abundant Nitride Semiconductors by Computational Screening and High-Pressure Synthesis. *Nature Communications*, 7(1):11962, 2016.

[164] Rainer Niewa, Dmitri A Zherebtsov, and Stefano Leoni. $Li_3[ScN_2]$: The First Nitridoscandate(III)-Tetrahedral Sc Coordination and Unusual MX_2 Framework. *Chemistry - A European Journal*, 9(17):4255–4259, 2003.

[165] J. Harris. Simplified Method for Calculating the Energy of Weakly Interacting Fragments. *Physical Review B*, 31(4):1770–1779, 1985.

[166] Éamonn D. Murray, Kyuho Lee, and David C. Langreth. Investigation of Exchange Energy Density Functional Accuracy for Interacting Molecules. *Journal of Chemical Theory and Computation*, 5(10):2754–2762, 2009.

[167] Mehmet Somer, Alper Yarasik, Lev Akselrud, Stefano Leoni, Helge Rosner, Walter Schnelle, and Rüdiger Kniep. Ae[Be_2N_2]: Nitridoberyllates of the Heavier Alkaline-Earth Metals. *Angewandte Chemie - International Edition*, 43(9):1088–1092, 2004.

[168] Martin Jansen and Ulrich Henseler. Synthesis, Structure Determination, and Ionic Conductivity of Sodium Tetrathiophosphate. *Journal of Solid State Chemistry*, 99(1):110–119, 1992.

[169] Zoltán A. Gál, Phillip M. Mallinson, Heston J. Orchard, and Simon J. Clarke. Synthesis and Structure of Alkaline Earth Silicon Nitrides: $BaSiN_2$, $SrSiN_2$, and $CaSiN_2$. *Inorganic Chemistry*, 43(13):3998–4006, 2004.

[170] Masatake Tsuji, Hidenori Hiramatsu, and Hideo Hosono. Tunable Light-Emission through the Range 1.8-3.2 eV and p-Type Conductivity at Room Temperature for Nitride Semiconductors, $Ca(Mg_{1-x}Zn_x)_2N_2$ (x=0-1). *Inorganic Chemistry*, 58(18):12311–12316, 2019.

[171] Martin Zeuner, Peter J. Schmidt, and Wolfgang Schnick. One-Pot Synthesis of Single-Source Precursors for Nanocrystalline LED Phosphors $M_2Si_5N_8$:Eu^{2+} (M = Sr, Ba). *Chemistry of Materials*, 21(12):2467–2473, 2009.

[172] Akitoshi Hayashi, Kousuke Noi, Atsushi Sakuda, and Masahiro Tatsumisago. Superionic Glass-Ceramic Electrolytes for Room-Temperature Rechargeable Sodium Batteries. *Nature Communications*, 3(1):856, 2012.

[173] Erik A. Wu, Christopher S. Kompella, Zhuoying Zhu, Jungwoo Z. Lee, Steven C. Lee, Iek-Heng Chu, Han Nguyen, Shyue Ping Ong, Abhik Banerjee, and Ying Shirley Meng. New Insights into the Interphase between the Na Metal Anode and Sulfide Solid-State Electrolytes: A Joint Experimental and Computational Study. *ACS Applied Materials & Interfaces*, 10(12):10076–10086, 2018.

[174] Verena Schultz-Coulon and Wolfgang Schnick. $CaMg_2N_2$ – ein gemischtes Erdalkalimetallnitrid mit anti$-La_2O_3-$Struktur / $CaMg_2N_2$ – a Mixed Alkaline-Earth Metal Nitride with anti$-La_2O_3$Structure. *Zeitschrift für Naturforschung B*, 50(4):619–622, 1995.

[175] Verena Schultz-Coulon and Wolfgang Schnick. Mg_2PN_3 und Ca_2PN_3 - Phosphor(V)-nitride mit eindimensional unendlich Ketten eckenverknüpfter PN_4-Tetraeder. *Zeitschrift für anorganische und allgemeine Chemie*, 623(1-6):69–74, 1997.

[176] Rachid Belkada, Masanori Kohyama, Toshiya Shibayanagi, and Masaaki Naka. Relative Stability of P63/m and P63 Structures of $\beta-Si_3N_4$. *Physical Review B*, 65(9):092104, 2002.

[177] Rainer Grün. The Crystal Structure of $\beta-Si_3N_4$: Structural and Stability Considerations between α- and $\beta-Si_3N_4$. *Acta Crystallographica Section B*, 35(4):800–804, 1979.

[178] Karsten Albe. Theoretical Study of Boron Nitride Modifications at Hydrostatic Pressures. *Physical Review B*, 55(10):6203–6210, 1997.

[179] George A. Jeffrey and G. S. Parry. Crystal Structure of Aluminum Nitride. *The Journal of Chemical Physics*, 23(2):406–406, 1955.

[180] Jelena Zagorac, Dejan Zagorac, Milena Rosić, J. Christian Schön, and Branko Matović. Structure Prediction of Aluminum Nitride Combining Data Mining and Quantum Mechanics. *CrystEngComm*, 19(35):5259–5268, 2017.

[181] Peter Kroll and Wolfgang Schnick. A Density Functional Study of Phosphorus Nitride P_3N_5: Refined Geometries, Properties, and Relative Stability of $\alpha-P_3N_5$ and $\gamma-P_3N_5$ and a Further Possible High-Pressure Phase $\delta-P_3N_5$ with Kyanite-Type. *Chemistry - A European Journal*, 8(15):3530–3537, 2002.

[182] Theodor Stefanidis and Anders G. Nord. Structure Studies of Thortveitite-like Dimanganese Diphosphate, $Mn_2P_2O_7$. *Acta Crystallographica Section C Crystal Structure Communications*, 40(12):1995–1999, 1984.

[183] Shin-ichi Nishimura, Naoto Tanibata, Akitoshi Hayashi, Masahiro Tatsumisago, and Atsuo Yamada. The Crystal Structure and Sodium Disorder of High-Temperature Polymorph $\beta-Na_3PS_4$. *Journal of Materials Chemistry A*, 5(47):25025–25030, 2017.

[184] Wenwu Yang, Junichi Hojo, Naoya Enomoto, Yumi Tanaka, and Miki Inada. Influence of Sintering Aid on the Translucency of Spark Plasma-Sintered Silicon Nitride Ceramics. *Journal of the American Ceramic Society*, 96(8):2556–2561, 2013.

[185] Kenji Watanabe, Takashi Taniguchi, and Hisao Kanda. Direct-Bandgap Properties and Evidence for Ultraviolet Lasing of Hexagonal Boron Nitride Single Crystal. *Nature Materials*, 3(6):404–409, 2004.

[186] R. D. Carson and Stephen E. Schnatterly. Valence-Band Electronic Structure of Silicon Nitride Studied with the Use of Soft-X-Ray Emission. *Physical Review B*, 33(4):2432–2438, 1986.

[187] Xuefeng Lu, Dong Qiu, Meng Chen, Lei Fan, Chao Wang, Hong-jie Wang, and GuanjunQiao. First Principles Calculations of Electronic Structures and Optical Properties of Al- and Ca-Doped $\beta-Si_3N_4$. *Materials Research Innovations*, 17(3):201–206, 2013.

[188] Abdul Ahad Khan, Rehmat Hasil, A. Laref, Naeem Ullah, Muhammad Sajjad, Aurang Zeb, and Ghulam Murtaza. DFT Prediction of the Structural, Electronic, Thermoelectric and Optical Properties of Ternary Pnictides $MgBe_2X_2$ (X = N, P, As, Sb, Bi): A Novel Analysis of Beryllium with 2A- and 5B-Elements of the Structure Type $CaAl_2Si_2$. *Solid State Communications*, 300:113667, 2019.

[189] Axel D. Becke and Erin R. Johnson. A Simple Effective Potential for Exchange. *The Journal of Chemical Physics*, 124(22):221101, 2006.

[190] Mathias Mallmann, Christian Maak, Robin Niklaus, and Wolfgang Schnick. Ammonothermal Synthesis, Optical Properties, and DFT Calculations of Mg_2PN_3 and Zn_2PN_3. *Chemistry - A European Journal*, 24(52):13963–13970, 2018.

[191] Cheng-Jun Duan, Xin Jun Wang, Will M. Otten, Anna C. A. Delsing, Jing-Tai Zhao, and H. T. Hintzen. Preparation, Electronic Structure, and Photoluminescence Properties of Eu^{2+} - and Ce^{3+} /Li^{+} -Activated Alkaline Earth Silicon Nitride $MSiN_2$ (M = Sr, Ba). *Chemistry of Materials*, 20(4):1597–1605, 2008.

[192] Lei Kang, Molin Zhou, Jiyong Yao, Zheshuai Lin, Yicheng Wu, and Chuangtian Chen. Metal Thiophosphates with Good Mid-Infrared Nonlinear Optical Performances: A First-Principles Prediction and Analysis. *Journal of the American Chemical Society*, 137(40):13049–13059, 2015.

[193] D. M. Bylander and Leonard Kleinman. Good Semiconductor Band Gaps with a Modified Local-Density Approximation. *Physical Review B*, 41(11):7868–7871, 1990.

[194] A. Seidl, Andreas Görling, Peter Vogl, Jacek A. Majewski, and Mel Levy. Generalized Kohn-Sham schemes and the Band-Gap Problem. *Physical Review B*, 53(7):3764–3774, 2 1996.

[195] Olaf Reckeweg, Cora Lind, Arndt Simon, and Francis J. DiSalvo. Rietveld Refinement of the Crystal Structure of $\alpha-Be_3N_2$ and the Experimental Determination of Optical Band Gaps for Mg_3N_2, Ca_3N_2 and $CaMg_2N_2$. *Zeitschrift für Naturforschung B*, 58(1):159–162, 2003.

[196] Luiz E. Ramos, Lara Kühl Teles, Luisa M. R. Scolfaro, José L. P. Castineira, Andreia Luisa da Rosa, and José R. Leite. Structural, Electronic, and Effective-Mass Properties of Silicon and Zinc-Blende Group-III Nitride Semiconductor Compounds. *Physical Review B*, 63(16):165210, 2001.

[197] Masakatsu Suzuki, Takeshi Uenoyama, and Akira Yanase. First-Principles Calculations of Effective-Mass Parameters of AlN and GaN. *Physical Review B*, 52(11):8132–8139, 1995.

[198] A. V. Shaposhnikov, I. P. Petrov, V. A. Gritsenko, and C. W. Kim. Electronic Band Structure and Effective Masses of Electrons and Holes in the α and β Phases of Silicon Nitride. *Physics of the Solid State*, 49(9):1628–1632, 2007.

[199] Yong Zhang, Wen Liu, and Hanben Niu. Native Defect Properties and p-Type Doping Efficiency in group-IIA doped wurtzite AlN. *Physical Review B*, 77(3):035201, 2008.

[200] R Q Wu, Lei Shen, Ming Yang, Zhen-Dong Sha, Yongqing Cai, Yuan Ping Feng, Zufang Huang, and Quing Yan Wu. Possible Efficient p-Type Doping of AlN using Be: An Ab Initio Study. *Applied Physics Letters*, 91(15):152110, 2007.

[201] Hiroshi Katayama-Yoshida, Takeshi Nishimatsu, Takashi Yamamoto, and Nozomi Orita. Comparison between the Theoretical Prediction of Codoping and the Recent Experimental Evidences in p-Type GaN, AlN, ZnSe, $CuInS_2$ and n-Type Diamond. *physica status solidi (b)*, 210(2):429–436, 1998.

[202] Rajendra Dahal, Jing Li, Sashikanth Majety, Bed Nidhi Pantha, Xiangke Cao, Jingyu Lin, and Hongxing Jiang. Epitaxially Grown Semiconducting Hexagonal Boron Nitride as a Deep Ultraviolet Photonic Material. *Applied Physics Letters*, 98(21):211110, 2011.

[203] Sashikanth Majety, Jing Li, Xiangke Cao, Rajendra Dahal, Bed Nidhi Pantha, Jingyu Lin, and Hongxing Jiang. Epitaxial Growth and Demonstration of Hexagonal BN/AlGaN p-n Junctions for Deep Ultraviolet Photonics. *Applied Physics Letters*, 100(6):061121, 2012.

[204] Helmut Werheit, Udo Kuhlmann, Koun Shirai, and Yukinobu Kumashiro. Interband Transitions and Phonon Spectra of Si-Doped $B_{12}P_2$. *Journal of Solid State Chemistry*, 133(1):140–144, 1997.

[205] Yukihiro Hirota and Takeshi Kobayashi. Chemical Vapor Deposition and Characterization of Phosphorus Nitride (P_3N_5) Gate Insulators for InP Metal-Insulator-Semiconductor Devices. *Journal of Applied Physics*, 53(7):5037–5043, 1982.

[206] Joel B. Varley, Vincenzo Lordi, Anna Miglio, and Geoffroy Hautier. Electronic Structure and Defect Properties of B_6O from Hybrid functional and Many-Body Perturbation Theory Calculations: A Possible Ambipolar Transparent Conductor. *Physical Review B - Condensed Matter and Materials Physics*, 90(4):1–9, 2014.

[207] Li_3GaN_2 Crystal Structure: Datasheet from "PAULING FILE Multinaries Edition – 2012" in SpringerMaterials https://materials.springer.com/isp/crystallographic/docs/sd_1703279 (accessed 05.01.2020)

[208] Frank Ottinger and Reinhard Nesper. Synthesis and Crystal Structure of the Nitridosilicates $Ca_5[Si_2N_6]$ and $Ca_7[NbSi_2N_9]$. *Zeitschrift fur Anorganische und Allgemeine Chemie*, 631(9):1597–1602, 2005.

[209] Halka Bilinski. Precipitation and Complex Formation in the System Manganese Perchlorate-Sodium Pyrophosphate $Mn(ClO_4)-Na_4P_2O_7-pH$ (295 K, I = 0.5 and I $\approx$ 0 Mol dm^{-3}). *Chemischer Informationsdienst*, 14(30):353–358, 1983.

[210] Martin Zeuner, Frauke Hintze, and Wolfgang Schnick. Low Temperature Precursor Route for Highly Efficient Spherically Shaped LED-Phosphors $M_2Si_5N_8$: Eu^{2+} (M = Eu, Sr, Ba). *Chemistry of Materials*, 21(2):336–342, 2009.

[211] Ramya Kormath Madam Raghupathy, Hendrik Wiebeler, Thomas D. Kühne, Claudia Felser, and Hossein Mirhosseini. Database Screening of Ternary Chalcogenides for p-Type Transparent Conductors. *Chemistry of Materials*, 30(19):6794–6800, 2018.

Acknowledgments

First, I thank Prof. Dr. Thomas D. Kühne for supervising the linear scaling part and introducing me to the speedCIGS-project, for which the computational high-throughput screening for transparent p-type semiconductors was undertaken. I am especially grateful to Dr. Hossein Mirhosseini, who supervised the second project. In addition, I thank both of them for their feedback on my thesis and together with Prof. Dr. Matthias Bauer for their willingness to review this dissertation. I am also thankful for the supervision of Dr. Ramya Kormath Raghupathy, who also worked on the screening. Furthermore, I thank Dr. Manjusha Chugh and Dr. Sudhir Kumar Sahoo, who worked on different topics of the speedCIGS-project, for the scientific discussions. As the group of Prof. Dr. Thomas D. Kühne grew over time, I thank its past and present members, in particular: Dr. Hossam Elgabarty, Dr. Andres Henao Aristizabal, Dr. Jure Gujt, Julian Heske, Naveen Kumar Kaliannan, Dr. Kristof Karhan, Dr. Deepak Ojha, Dr. Thomas Spura and Frederik Zysk. They provided a productive and friendly atmosphere during my work at the university and at later visits. The work on the speedCIGS-project was carried out in the technology park and owing to this, I also thank Britta Fremerey for her assistance during the process of setting-up the offices in the technology park and relocation. I also thank my brother Christian for proofreading this thesis. Furthermore, his knowledge in semiconductor physics helped me in understanding the physical aspects that were of relevance for the p-type semiconductor screening. I also have to thank him and my parents for their support during some rough times. Last but not least, I am thanking the Paderborn Center for Parallel Computing (PC^2): Without their technical support and the provided high-performance computing resources, the high-throughput screening would have not been possible.